SHORTCUT TO TARGET STATES IN A SPIN-1 BOSE-EINSTEIN CONDENSATE

A Dissertation
Presented to
The Academic Faculty

By

Lin Xin

In Partial Fulfillment
of the Requirements for the Degree
Doctor of Philosophy in the
School of Physics
Department of Atomic, Molecular and Optical Physics

Georgia Institute of Technology

Aug 2022

SHORTCUT TO TARGET STATES IN A SPIN-1 BOSE-EINSTEIN CONDENSATE

Thesis committee:

Dr. Michael S. Chapman, Advisor
School of Physics
Georgia Institute of Technology

Dr. Creston Herold
Georgia Tech Research Institute
Georgia Institute of Technology

Dr. T. A. B. Kennedy
School of Physics
Georgia Institute of Technology

Dr. Martin Mourigal
School of Physics
Georgia Institute of Technology

Dr. Colin Parker
School of Physics
Georgia Institute of Technology

Date approved: May 19, 2022

To my parents, Mr. Xiangyang Xin and Mrs. Yan Bao

In memory of my grandparents, Mr. Xuguang Xin, Mr. Muyong Bao and Mr. Zuliang Huang

ACKNOWLEDGMENTS

I would like to take this opportunity to thank the people who have inspired and supported me through this wonderful journey with unforgettable memories.

First and foremost, I would like to thank my advisor Prof. Michael Chapman. He gave me an opportunity to join the group, despite the fact that I had no experience in experimental physics. His speech with great pacing and pulses always rephrases complexity into simplicity. It is very generous of him to tolerate me or other group members making mistakes. His clever humor influences me deeply. For example, he once showed a video of a Karate kid breaking a board to all group members and suggested a similarity to a Ph.D. You tried, you exhausted, you cried, and yet you persistently kick until suddenly the board broke. Mike is also a supportive advisor in both academia and life. I get all the help I need from him for presentations, award applications, and job interviews. Once, he emailed me to care about my family's safety when an explosion near our tour destination. This is just one of many warm things he did and I could not thank him more.

I would like to extend my gratitude to my committee members and other professors. It is pleasant to take many classes with Prof. Brian Kennedy, who is no doubt one of the best teachers at Georgia Tech. He always welcomed me even when bothering him with various questions, one of which later led to a collaborated theory paper. During the collaboration, I learned so much from him with his patience including the spirit of striving for perfectness. Prof. Colin Parker is very kind to offer his expertise and physics insight through many stimulating discussions. I also would like to thank Dr. Creston Herold and Prof. Martin Mourigal who are generous to be on my thesis committee on short notice. I also got extensive help from Prof. Carlos S. De Melo, who kindly agree to be my reference during the job searching. We had a lot of great times while playing ping pong and chatting about all the interesting stories and physics.

I'm grateful to work with several wonderful and talented lab colleagues after I arrived

at Georgia Tech. Dr. Bharath Hebbe Madhusudhana was working on the experiment for his thesis when I joined the lab. His diligence and smartness really impressed me and his insight into theory continued to inspire me throughout the years. Meanwhile, Dr. Matthew Boguslawski, an expert in electronics and machining, taught me plenty of skills that filled my knowledge gap in experiments. After work, he also introduced me to ballroom dancing. Maryrose Barrios has worked with me together for the longest time and I want to thank her for enduring my slow adaption to the team working style. She is a great friend after school for kindly hosting Christmas parties and recommending me to attend the scuba diving class. Julia Cohen is a talented student with an optimistic attitude. She gave me invaluable help on paper writing and job application. Byron Lowry who worked in GTRI kindly shared lots of his techniques with the group. Our new member, Zhixin Song has adapted quickly to the group and begins to contribute.

Besides the BEC group, I would like to express my gratitude to the former and present members of our lab. Thomas Dellaert and I worked together on building the mini-MOT setup. I shared lots of fun with Deniz Kurdak and Ms. Laura O'Donnell while working on the Barium ion trap project. Mikai Hulse, Tetsuro Ishida, and Chureh Atasi are hard-working and talented undergraduate students who I mentored. I learned new science while working with all of them.

Special thanks to my friends, especially postdocs and graduate students from AMO groups. There are too many names for me to mention. I cannot count how many times we borrowed equipment and shared knowledge with each other especially late at night.

Finally, I would like to thank my parents for their unconditional and endless love throughout my endeavor. Even knowing how every reunion will be difficult across the most distant way in the world, they still encouraged their only child to pursue his dream without any hesitation. They even kept my dad's cancer a secret until the surgery is done to prevent me from worrying. I am forever indebted to them.

Last but not least, I want to thank myself for staying through all the difficulties and

struggles. I hung in there when I didn't know if the experiment will ever work, when my family members passed away, when I had to rush back to the United States after over 40 hours of flight due to the COVID border seal, and when the pandemic stopped me from making progress. Those experiences enable me to face any difficulties in my future.

TABLE OF CONTENTS

LIST OF TABLES

LIST OF FIGURES

SUMMARY

An important frontier of research in metrology is the development of techniques to surpass the standard quantum limit using quantum squeezed states or other entangled states. In this thesis, we report the first observation of squeezed ground states generation in a ^{87}Rb spinor condensate. The measurement of squeezed ground states builds on previous experiments of spin-nematic squeezing. A spin-1 Bose-Einstein condensate is tuned near the quantum critical point between the polar and ferromagnetic quantum phases to create a ground state with squeezing properties. In contrast to typical non-equilibrium methods for preparing atomic squeezed states by quenching through a quantum phase transition, squeezed ground states are time-stationary and remain squeezed for the lifetime of the condensate. A squeezed ground state with a metrological improvement up to $6 - 8$ dB and a constant squeezing angle maintained over 2 s is demonstrated.

A protocol consisting of a pair of controlled quenches of an external magnetic field is applied, which allows fast tuning of the system Hamiltonian in the vicinity of a phase transition. Our protocol effectively shortcuts the adiabatic technique, overcoming the challenge of maintaining adiabaticity in the neighborhood of the quantum critical point where the frequency scale of the final Hamiltonian evolution tends to zero. This protocol is indicative of creating eigenstates of the system through the non-adiabatic method and lay the foundation for future experiments involving entangled eigenstates generation.

In addition, we extend our studies to further improve the control of a quantum system and the Hamiltonian engineering of a many-body system. In this thesis, we present our proposals and preliminary results.

CHAPTER 1
INTRODUCTION AND BACKGROUND

1.1 A Brief History of Bose-Einstein Condensate

The idea of Bose-Einstein condensation (BEC) was formulated about 100 years ago by Satyendra Nath Bose and Albert Einstein in 1924-1925 [1, 2]. With the breakthroughs in laser cooling developed by 1997 Nobel laureates Chu, Cohen-Tannoudji, Phillips, and others [3], lasers quickly became a workhorse in the BEC quest. The achievement of BEC was recognized by the Nobel prizes for Cornell, Ketterle, and Wieman in 2001 [4, 5].

1.2 Spinor BEC

In the early condensate systems using magnetic traps, only atoms in a weak-field seeking state were magnetically trapped, and therefore, their spin degrees of freedom were frozen. A spinor Bose-Einstein condensate, namely a BEC with spin internal degrees of freedom, was first realized in a gas of spin-1 anti-ferromagnetic ^{23}Na atoms confined in an optical dipole trap in 1998 [6].

The first condensates with ferromagnetic ordering were realized by our group using ^{87}Rb condensates created directly in optical traps [7]. The focus of these initial investigations was on verifying the sign of the spinor dynamical energy for the $F = 1$ ^{87}Rb which had been predicted to be negative [8] . In the subsequent work, our group demonstrated for the first time the coherent oscillation of the spinor system [9], which provided the first convincing validation of the mean-field theoretical treatment of the system dynamics. Number squeezing (as known as sub-Poissonian fluctuations) [10] is observed with the spin-mixing procedure and later the spin-nematic squeezing (as known as quadrature squeezing) [11] is observed with the spinor phase shifted by microwave pulses. Those breakthroughs widen

the research topic from the mean values of observables to the uncertainties. Afterward, our group studied the important physics related to the energy gaps, such as the parametric excitation [12], the adiabatic state preparation [13], and the quantum Kibble-Zurek mechanism [14]. At the same time, the experimental advance leads us further improve the way to control the system thus studying novel problems including dynamic stabilization theories [15] and singular loops in Bloch spheres [16].

1.3 Thesis Contribution and Organization

This thesis describes the theory [17] along with the experimental results [18] for squeezed ground states in the spin-1 ferromagnetic condensate. This work draws heavily on the work of previous doctoral students.

The thesis is organized as follows. Chapter 2 gives detailed derivation for the basic spinor BEC theory. Here quantum and semi-classical theoretical approaches are discussed. In Chapter 3, the experimental apparatus is discussed in detail. This has been covered extensively before and this thesis contains the detailed measurement of the all-optical BEC technique on the latest apparatus for future reference. The tools used to manipulate and observe the BEC will be expounded in more detail. In Chapter 4, the theory of time-stationary squeezed states is studied through a discussion of harmonic oscillator approximation, optimal quantum control, and finite system size effect. These ideas are applied to the ground states of spinor BEC along with a comparison to the highest excited states. In Chapter 5, the theoretical predictions are compared to the measured results. Using the theory and simulation result from Chapter 4, a measurement protocol is developed to access the squeezed ground states. Several details of the measurement protocol and calibration for data analysis are discussed. Chapter 6 describes the extra theoretical projects that are possible to be implemented into the experimental platforms and Chapter 7 contains the experimental projects that are conducted as a future improvement to the apparatus. Finally, Chapter 8 contains some concluding remarks and possible future directions.

The information necessary for the explorations described in this thesis more resembles a manual rather than a linear narrative. Because of this, the topics are more categorized for the convenience to look up.

CHAPTER 2

BASIC SPINOR BEC THEORY

2.1 Gross-Pitaevskii Equation

The Hamiltonian of the condensate includes the kinetic energy, potential energy of the confined trap V_T, and the two-body interaction energy.

$$H = \sum_{i}^{N}(-\frac{\nabla^2}{2m} + V_T) + \sum_{i,j,i<j}^{N} V(\vec{r_i} - \vec{r_j}) = \sum_{i}^{N}(-\frac{\nabla^2}{2m} + V_T) + \frac{1}{2}\sum_{i,j,i\neq j}^{N} V(\vec{r_i} - \vec{r_j}). \quad (2.1)$$

Equation 2.1 is called the Gross-Pitaevskii equation (or nonlinear Schrödinger equation) [19, 20, 21]. For the low-temperature limit where there is only s-wave scattering, the spin-mixing interaction is modeled as a contact pseudo-potential in two-body collisions. During the collision, the total spin of two-body is the sum of individual spin $\vec{F} = \vec{f_1} + \vec{f_2},\ F = 2f, 2f-1, \cdots 0$. The interaction between two atoms in a collision is given by

$$V(\vec{r_1} - \vec{r_2}) = \delta(\vec{r_1} - \vec{r_2}) \sum_{F=0}^{2f} g_F P_F, \quad (2.2)$$

with projection operator in the form $P_F = \sum_{m_F=-F}^{F} |F, m_F><F, m_F|$ and the coupling strength $g_F = \frac{4\pi\hbar^2 a_F}{m}$. a_F is the s-wave scattering length for total spin-F channel, and m is the atomic mass. Since for ^{87}Rb the total spin equals nuclear spin $\frac{3}{2}$ add electron spin $\frac{1}{2}$, we have $f = 1$ or 2, which are both bosons. The scattering channels for $f = 1$ is written in

the form $|F, m_F >= |m_{f_1} > |m_{f_2} >$ as the following:

$$\begin{cases} |2,2>=|1>|1> \\ |2,1>=\frac{1}{\sqrt{2}}(|0>|1>+|1>|0>) \\ |2,0>=\frac{1}{\sqrt{6}}(|-1>|1>+2|0>|0>+|1>|-1>) \\ |2,-1>=\frac{1}{\sqrt{2}}(|0>|-1>+|-1>|0>) \\ |2,-2>=|-1>|-1> \end{cases}, \tag{2.3}$$

$$\begin{cases} |1,1>=\frac{1}{\sqrt{2}}(|0>|1>-|1>|0>) \\ |1,0>=\frac{1}{\sqrt{2}}(|-1>|1>-|1>|-1>) \\ |1,-1>=\frac{1}{\sqrt{2}}(|-1>|0>-|0>|-1>) \end{cases}, \tag{2.4}$$

and

$$|0,0>=\frac{1}{\sqrt{3}}(|-1>|1>-|0>|0>+|1>|-1>). \tag{2.5}$$

When we consider the $f = 1$ atoms collide, the state has to be symmetric which leads the scattering channel to only be $F = 0$ or $F = 2$.

The spin-spin coupling of two spin-f bosons can be found using the identity

$$\vec{f_1} \cdot \vec{f_2} = \frac{\hat{F}^2 - \hat{f_1}^2 - \hat{f_2}^2}{2} = \frac{F(F+1) - 2f(f+1)}{2}. \tag{2.6}$$

Applying the identity operator leads to

$$\vec{f_1} \cdot \vec{f_2} = \vec{f_1} \cdot \vec{f_2} \sum_{F=0,even}^{2f} P_F = \sum_{F=0,even}^{2f} \lambda_F P_F, \tag{2.7}$$

where $\lambda_F = \frac{F(F+1)-2f(f+1)}{2}$. Here the closure relationship is used since the sum of projec-

tion operators equals identity operator. For $f = 1$ condensates,

$$1 = P_0 + P_2,\ \vec{f_1} \cdot \vec{f_2} = P_2 - 2P_0. \tag{2.8}$$

Thus,

$$\begin{aligned} V(\vec{r_1} - \vec{r_2}) &= \delta(\vec{r_1} - \vec{r_2}) \sum_{F=0}^{2f} g_F P_F \\ &= \delta(\vec{r_1} - \vec{r_2})(g_0 P_0 + g_2 P_2) \\ &= \delta(\vec{r_1} - \vec{r_2})(c_0(P_0 + P_2) + c_2(P_2 - 2P_0)) \\ &= \delta(\vec{r_1} - \vec{r_2})(c_0 + c_2 \vec{f_1} \cdot \vec{f_2}), \end{aligned} \tag{2.9}$$

where $c_0 := \frac{g_0+2g_2}{3}$ and $c_2 := \frac{g_2-g_0}{3}$. The continuous integration of the total Hamiltonian is used instead of the discrete sum hereafter:

$$\begin{aligned} H = &\sum_{i=-1,0,1} \int d^3\vec{r} \psi_i^\dagger (-\frac{\nabla^2}{2m} + V_T)\psi_j \\ &+ \frac{1}{2} \int d^3\vec{r} (\sum_{i,j=\pm 1,0} c_0 \psi_i^\dagger \psi_j^\dagger \psi_j \psi_i + \sum_{i,j,k,l=\pm 1,0} c_2 \psi_i^\dagger \psi_j^\dagger (\vec{f_{jk}} \cdot \vec{f_{il}}) \psi_k \psi_l), \end{aligned} \tag{2.10}$$

where $i = \pm 1, 0$ denotes the different Zeeman states. The identity operator makes the c_0 channel represent as $\psi_i^\dagger \psi_j^\dagger \psi_j \psi_i$. The entire Hamiltonian can be decompose into spin-independent symmetry part and asymmetry part:

$$H_s = \sum_{i=-1,0,1} \int d^3\vec{r} \psi_i^\dagger (-\frac{\nabla^2}{2m} + V_T)\psi_i + \frac{c_0}{2} \int d^3\vec{r} \sum_{i,j=\pm 1,0} \psi_i^\dagger \psi_j^\dagger \psi_j \psi_i, \tag{2.11}$$

and

$$\begin{aligned} H_a = &\frac{c_2}{2} \int d^3\vec{r} \psi_1^\dagger \psi_1^\dagger \psi_1 \psi_1 + \psi_{-1}^\dagger \psi_{-1}^\dagger \psi_{-1} \psi_{-1} + 2\psi_1^\dagger \psi_0^\dagger \psi_0 \psi_1 \\ &- 2\psi_1^\dagger \psi_{-1}^\dagger \psi_{-1} \psi_1 + 2\psi_0^\dagger \psi_{-1}^\dagger \psi_{-1} \psi_0 + 2\psi_{-1}^\dagger \psi_1^\dagger \psi_0 \psi_0 + 2\psi_0^\dagger \psi_0^\dagger \psi_{-1} \psi_1. \end{aligned} \tag{2.12}$$

The asymmetry part is calculated based on the spin-1 Pauli operators:

$$f_x = \frac{1}{\sqrt{2}} \begin{pmatrix} 0 & 1 & 0 \\ 1 & 0 & 1 \\ 0 & 1 & 0 \end{pmatrix}, f_y = \frac{i}{\sqrt{2}} \begin{pmatrix} 0 & -1 & 0 \\ 1 & 0 & -1 \\ 0 & 1 & 0 \end{pmatrix}, f_z = \begin{pmatrix} 1 & 0 & 0 \\ 0 & 0 & 0 \\ 0 & 0 & -1 \end{pmatrix}. \tag{2.13}$$

Each element of the sum has the detailed form as the following:

$$(\vec{\psi}^\dagger f_x \vec{\psi})^2 = \frac{1}{2}(\psi_1^\dagger \psi_0 + \psi_0^\dagger \psi_{-1} + (\psi_0^\dagger \psi_1 + \psi_{-1}^\dagger \psi_0))^2, \tag{2.14}$$

$$(\vec{\psi}^\dagger f_y \vec{\psi})^2 = (-\frac{1}{2}(\psi_1^\dagger \psi_0 + \psi_0^\dagger \psi_{-1} - (\psi_0^\dagger \psi_1 + \psi_{-1}^\dagger \psi_0)))^2, \tag{2.15}$$

$$(\vec{\psi}^\dagger f_z \vec{\psi})^2 = (\psi_1^\dagger \psi_1 - \psi_{-1}^\dagger \psi_{-1})^2, \tag{2.16}$$

and

$$\psi_i^\dagger \psi_j^\dagger (\vec{f_{jk}} \cdot \vec{f_{il}}) \psi_k \psi_l = 2(\psi_1^\dagger \psi_0 + \psi_0^\dagger \psi_{-1})^2 + 2(\psi_0^\dagger \psi_1 + \psi_{-1}^\dagger \psi_0)^2 + (\psi_1^\dagger \psi_1 - \psi_{-1}^\dagger \psi_{-1})^2. \tag{2.17}$$

2.2 Single Mode Approximation

When the size of the condensate is smaller than the spin healing length $\xi_s = h/\sqrt{2m|c_2|n}$, where n is atom number density, the spin components have the same spatial wave function which leads to the single mode approximation (SMA):

$$\psi_i \approx a_i \sqrt{N} \phi(r), \int |\phi(r)|^2 = 1. \tag{2.18}$$

Here $\phi(r)$ is renormalized. For ^{87}Rb and ^{23}Na, $c_0 \gg |c_2|$, the symmetric Hamiltonian is the dominant term and determines the partial wave function $\phi(r)$ with

$$(-\frac{\nabla^2}{2m} + V_T + \frac{c_0}{2}N|\phi|^2)\phi = \mu\phi. \tag{2.19}$$

As a result, the symmetric part of the Hamiltonian

$$\begin{aligned} H_s &= \sum_{i=-1,0,1} \int d^3\vec{r}\psi_i^\dagger(\mu - \frac{c_0}{2}N|\phi|^2)\psi_i + \frac{c_0}{2}\int d^3\vec{r} \sum_{i,j=\pm1,0} \psi_i^\dagger\psi_j^\dagger\psi_j\psi_i \\ &= \sum_{i=-1,0,1} a_i^\dagger N(\mu - c_0'N)a_i + c_0'N^2 \sum_{i,j=\pm1,0} a_i^\dagger a_j^\dagger a_j a_i \\ &= \mu\hat{N} + c_0'\hat{N}(\hat{N}-1), \end{aligned} \tag{2.20}$$

where $c_0' := \frac{c_0}{2}\int|\phi(r)|^4$. With the same derivation, the asymmetric part has the following formula:

$$H_a = c_2'(\hat{S}^2 - 2\hat{N}), \tag{2.21}$$

where $\hat{S}^2 = \hat{S}_x^2 + \hat{S}_y^2 + \hat{S}_z^2$ and $c_2' := \frac{c_2}{2}\int|\phi(r)|^4$. $c_2 < 0$ means ferromagnetic, while $c_2 > 0$ is anti-ferromagnetic. Each operator has the form as shown in Table 2.1. Because H_s is spin-independent, the dynamics of spinor state is decided by H_a.

Table 2.1: Spin-1 dipole operators. Matrices in spherical polar basis $|f, m_f\rangle$.

$$S_x = \frac{1}{\sqrt{2}} \begin{pmatrix} 0 & 1 & 0 \\ 1 & 0 & 1 \\ 0 & 1 & 0 \end{pmatrix} \qquad S_x = \frac{1}{\sqrt{2}}(a_1^\dagger a_0 + a_0^\dagger a_{-1} + a_0^\dagger a_1 + a_{-1}^\dagger a_0)$$

$$S_y = \frac{i}{\sqrt{2}} \begin{pmatrix} 0 & -1 & 0 \\ 1 & 0 & -1 \\ 0 & 1 & 0 \end{pmatrix} \qquad S_y = \frac{i}{\sqrt{2}}(-a_1^\dagger a_0 - a_0^\dagger a_{-1} + a_0^\dagger a_1 + a_{-1}^\dagger a_0)$$

$$S_z = \begin{pmatrix} 1 & 0 & 0 \\ 0 & 0 & 0 \\ 0 & 0 & -1 \end{pmatrix} \qquad S_z = (a_1^\dagger a_1 - a_{-1}^\dagger a_{-1})$$

2.3 Magnetic fields

The magnetic field introduces energy shifts to the Zeeman sub-levels of the hyperfine state. The Zeeman energy for total atoms in each spinor state becomes

$$\begin{aligned} E_1 &= pN_1 + qN_1 + N_1 E_0 \\ E_0 &= N_0 E_0 \\ E_{-1} &= -pN_{-1} + qN_{-1} + N_{-1} E_0, \end{aligned} \tag{2.22}$$

where $p = -\mu_B B_z g_f$, $q = \mu_B^2 B_z^2/(\hbar^2 E_{hfs})$ are the linear and quadratic Zeeman effect accordingly [22]. g_f is the Landé g factor and E_{HFS} is the ground state hyperfine splitting. The total magnetic field energy is given by

$$E_B = p(N_1 - N_{-1}) + q(N_1 + N_{-1}) + NE_0. \tag{2.23}$$

Now the system with external magnetic fields in the z direction has the Hamiltonian

$$\begin{aligned} H_a &= c_2'(S^2 - 2N) + E_B \\ &= c_2'(S^2 - 2N) + pS_z + \frac{q}{2}Q_{zz}, \end{aligned} \tag{2.24}$$

where the quadrupole operator $Q_{i,j} = S_iS_j + S_jS_i - \frac{4}{3}\delta_{i,j}$ (see Table 2.2). Since N is a constant, N can be neglected in H_a.

Table 2.2: Spin-1 quadrapole operators. Matrices in spherical polar basis $|f, m_f\rangle$.

$$Q_{xx} = \begin{pmatrix} -\frac{1}{3} & 0 & 1 \\ 0 & \frac{2}{3} & 0 \\ 1 & 0 & -\frac{1}{3} \end{pmatrix} \qquad Q_{xx} = -\tfrac{1}{3}a_1^\dagger a_1 + \tfrac{2}{3}a_0^\dagger a_0 - \tfrac{1}{3}a_{-1}^\dagger a_{-1} + a_1^\dagger a_{-1} + a_{-1}^\dagger a_1$$

$$Q_{yy} = \begin{pmatrix} -\frac{1}{3} & 0 & -1 \\ 0 & \frac{2}{3} & 0 \\ -1 & 0 & -\frac{1}{3} \end{pmatrix} \qquad Q_{yy} = -\tfrac{1}{3}a_1^\dagger a_1 + \tfrac{2}{3}a_0^\dagger a_0 - \tfrac{1}{3}a_{-1}^\dagger a_{-1} - a_1^\dagger a_{-1} - a_{-1}^\dagger a_1$$

$$Q_{zz} = \begin{pmatrix} \frac{2}{3} & 0 & 0 \\ 0 & -\frac{4}{3} & 0 \\ 0 & 0 & \frac{2}{3} \end{pmatrix} \qquad Q_{zz} = \tfrac{2}{3}a_1^\dagger a_1 - \tfrac{4}{3}a_0^\dagger a_0 + \tfrac{2}{3}a_{-1}^\dagger a_{-1}$$

$$Q_{xy} = i\begin{pmatrix} 0 & 0 & -1 \\ 0 & 0 & 0 \\ 1 & 0 & 0 \end{pmatrix} \qquad Q_{xy} = i(-a_1^\dagger a_{-1} + a_{-1}^\dagger a_1)$$

$$Q_{xz} = \tfrac{1}{\sqrt{2}}\begin{pmatrix} 0 & 1 & 0 \\ 1 & 0 & -1 \\ 0 & -1 & 0 \end{pmatrix} \qquad Q_{xz} = \tfrac{1}{\sqrt{2}}(a_1^\dagger a_0 - a_0^\dagger a_{-1} + a_0^\dagger a_1 - a_{-1}^\dagger a_0)$$

$$Q_{yz} = \tfrac{i}{\sqrt{2}}\begin{pmatrix} 0 & -1 & 0 \\ 1 & 0 & 1 \\ 0 & -1 & 0 \end{pmatrix} \qquad Q_{yz} = \tfrac{i}{\sqrt{2}}(-a_1^\dagger a_0 + a_0^\dagger a_{-1} + a_0^\dagger a_1 - a_{-1}^\dagger a_0)$$

2.4 Semi-classical Approach

The spinor dynamics of the condensate can be derived using the Heisenberg equation of motion

$$i\hbar\frac{\partial a_i}{\partial t} = [a_i, H_a]. \tag{2.25}$$

To simplify the notation, $c := 2c_2'N$ is used hereafter. For each spin component we can get

$$\begin{aligned} i\hbar\frac{\partial a_1}{\partial t} =& c(a_1^\dagger a_1 a_1 + a_0^\dagger a_0 a_1 - a_{-1}^\dagger a_{-1} a_1 + a_{-1}^\dagger a_0 a_0) \\ i\hbar\frac{\partial a_0}{\partial t} =& c(a_1^\dagger a_0 a_1 + a_{-1}^\dagger a_{-1} a_0 + 2a_0^\dagger a_{-1} a_1) \\ i\hbar\frac{\partial a_{-1}}{\partial t} =& c(a_{-1}^\dagger a_{-1} a_{-1} - a_1^\dagger a_{-1} a_1 + a_0^\dagger a_{-1} a_0 + a_1^\dagger a_0 a_0). \end{aligned} \tag{2.26}$$

Under the mean-field description $a_i = e^{-i\mu t}\xi_i$ and by neglecting the global phase $e^{-i\mu t}$ [23], Equation 2.26 can be simplified as

$$\begin{aligned} i\hbar\frac{\partial \xi_1}{\partial t} =& E_1\xi_1 + c(\xi_1^\dagger \xi_1 \xi_1 + \xi_0^\dagger \xi_0 \xi_1 - \xi_{-1}^\dagger \xi_{-1} \xi_1 + \xi_{-1}^\dagger \xi_0 \xi_0) \\ i\hbar\frac{\partial \xi_0}{\partial t} =& E_0\xi_0 + c(\xi_1^\dagger \xi_0 \xi_1 + \xi_{-1}^\dagger \xi_{-1} \xi_0 + 2\xi_0^\dagger \xi_{-1} \xi_1) \\ i\hbar\frac{\partial \xi_{-1}}{\partial t} =& E_{-1}\xi_{-1} + c(\xi_{-1}^\dagger \xi_{-1} \xi_{-1} - \xi_1^\dagger \xi_{-1} \xi_1 + \xi_0^\dagger \xi_{-1} \xi_0 + \xi_1^\dagger \xi_0 \xi_0), \end{aligned} \tag{2.27}$$

which can be further simplified as

$$\begin{aligned} i\hbar\frac{\partial \xi_1}{\partial t} =& E_1\xi_1 + c((\rho_1 + \rho_0 - \rho_{-1})\xi_1 + \xi_{-1}^\dagger \xi_0 \xi_0) \\ i\hbar\frac{\partial \xi_0}{\partial t} =& E_0\xi_0 + c((\rho_1 + \rho_{-1})\xi_0 + 2\xi_0^\dagger \xi_{-1} \xi_1) \\ i\hbar\frac{\partial \xi_{-1}}{\partial t} =& E_{-1}\xi_{-1} + c((\rho_{-1} + \rho_0 - \rho_1)\xi_{-1} + \xi_1^\dagger \xi_0 \xi_0). \end{aligned} \tag{2.28}$$

Here $\rho_i = N_i/N$ is the relative population and $E_i = pi + qi^2$. The wave function $\psi = (\xi_1, \xi_0, \xi_{-1})$ is under the constraint that $|\xi_1|^2 + |\xi_0|^2 + |\xi_{-1}|^2 = 1$. The number of real

variables can be further reduced to 4 under the constraint:

$$\xi_1 = \sqrt{\frac{1-\rho_0+m}{2}}\exp^{i\chi_+}, \xi_0 = \sqrt{\rho_0}, \xi_{-1} = \sqrt{\frac{1-\rho_0-m}{2}}\exp^{i\chi_-}, \tag{2.29}$$

with $\chi_\pm = \frac{\theta_s \pm \theta_m}{2}, m = \frac{N_1 - N_{-1}}{N}$. θ_s and θ_m are called the spinor phase and magnetization phase, which are the relative phase between N_0 and $N_{\pm 1}$ and the relative phase between N_{+1} and N_{-1} accordingly. Using this parametreization and changing to a rotating frame to remove the magnetization phase ($\xi'_{\pm 1} \rightarrow e^{\mp i\theta_m/2}\xi_{\pm 1}$), the equations can be further simplified to just two dynamical variables, ρ_0 and θ_s [23].

$$\begin{aligned}
\dot{\rho_0} &= \frac{2c}{\hbar}\rho_0\sqrt{(1-\rho_0)^2 - m^2}\sin(\theta_s) \\
\dot{\theta_s} &= -\frac{2q}{\hbar} + \frac{2c}{\hbar}(1-2\rho_0) + \frac{2c}{\hbar}\frac{(1-\rho_0)(1-2\rho_0) - m^2}{\sqrt{(1-\rho_0)^2 - m^2}}\cos(\theta_s)
\end{aligned} \tag{2.30}$$

The energy per atom equals to

$$E = \frac{c}{2}m^2 + c\rho_0[(1-\rho_0) + \sqrt{(1-\rho_0)^2 - m^2}cos\theta_s] + pm + q(1-\rho_0). \tag{2.31}$$

A given set of relative spin operators $(s_x, s_y, q_{yz}, q_{xz}) := (S_x/N, S_y/N, Q_{yz}/N, Q_{xz}/N)$ is generated from Gaussian distributions satisfying the uncertainty relationships (see Table 2.4) for spin-1 operators $\Delta S_x \Delta Q_{yz} = N$ and $\Delta S_y \Delta Q_{xz} = N$ with all atoms in $m_F = 0$. One set of relative spin operators is used to compute one set of the mean-field

variables based on Table 2.3 which gives the following relationships:

$$\begin{aligned}
\chi_+ &= \arctan(-\frac{s_y + q_{yz}}{s_x - q_{xz}}) \\
\chi_- &= \arctan(\frac{s_y - q_{yz}}{s_x - q_{xz}}) \\
\theta_s &= \chi_+ + \chi_- \\
\rho_0 &= \frac{1}{2} + \sqrt{\frac{1}{4} - \frac{1}{8}\big((\frac{s_x + q_{xz}}{\cos\chi_+})^2 + (\frac{s_x - q_{xz}}{\cos\chi_-})^2\big)} \\
m &= \frac{1}{8\rho_0}\big((\frac{s_x + q_{xz}}{\cos\chi_+})^2 - (\frac{s_x - q_{xz}}{\cos\chi_-})^2\big).
\end{aligned} \tag{2.32}$$

In the limit $N \gg 1$, the uncertainty relationships for the relative spin operators $\Delta s_x \Delta q_{yz} = 1/N$ and $\Delta s_y \Delta q_{xz} = 1/N$ indicate a distribution with $\rho_0 \to 1$, $m \to 0$ and uniform θ_s in $[0, 4\pi]$. This set sampling process is repeated for N times to simulate the quantum dynamics with the mean-field equations [24].

The spinor phase shift $\Delta\theta_s$ can be added by applying a small change directly to $\theta_s \to \theta_s + \Delta\theta_s$ or applying the operation $\xi_0 \to \xi_0 e^{-i\Delta\theta_s/2}$. This operation is important in searching the maximum squeezing angles.

Table 2.3: Spin-1 observables in mean-field parameters.

s_x	$= \sqrt{\rho_0}(\sqrt{1-\rho_0+m}\cos(\chi_+) + \sqrt{1-\rho_0-m}\cos(\chi_-))$
s_y	$= -\sqrt{\rho_0}(\sqrt{1-\rho_0+m}\sin(\chi_+) - \sqrt{1-\rho_0-m}\sin(\chi_-))$
s_z	$= \frac{1}{2}m$
q_{yz}	$-\sqrt{\rho_0}(\sqrt{1-\rho_0+m}\sin(\chi_+) + \sqrt{1-\rho_0-m}\sin(\chi_-))$
q_{xz}	$= \sqrt{\rho_0}(\sqrt{1-\rho_0+m}\cos(\chi_+) - \sqrt{1-\rho_0-m}\cos(\chi_-))$
s_z^2	$= 1 - \rho_0$
$s_x^2 + s_y^2$	$= 2\rho_0(1-\rho_0) + 2\rho_0\sqrt{(1-\rho_0)^2 - m^2}\cos\theta_s$
$q_{yz}^2 + q_{xz}^2$	$= 2\rho_0(1-\rho_0) - 2\rho_0\sqrt{(1-\rho_0)^2 - m^2}\cos\theta_s$
x	$= 2\rho_0 - 1$
$x^2 + s_x^2 + s_y^2 + q_{yz}^2 + q_{xz}^2$	$= 1$

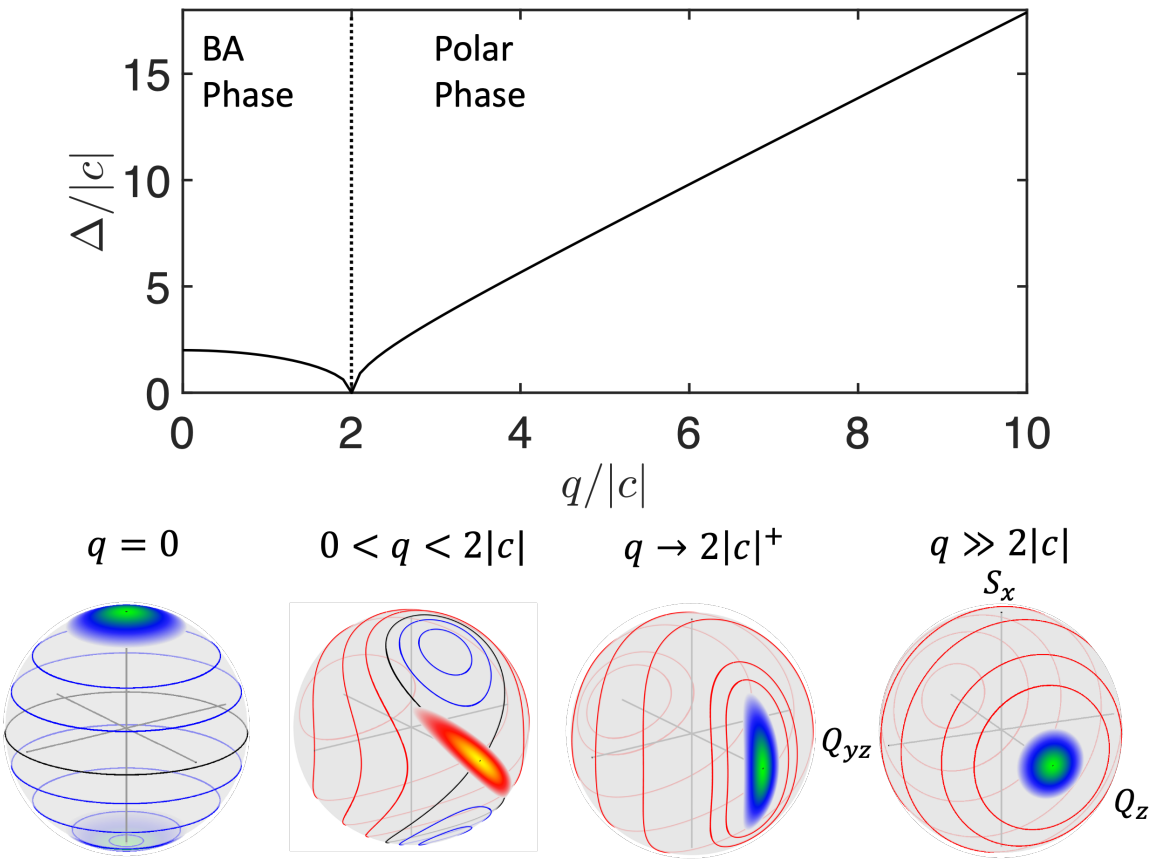

Figure 2.1: The phase transition energy gap and spin-nematic sphere for different magnetic fields. The energy gap between the ground state and the first excited-state shows the phase transition happens at $q = 2|c|$. When $q \gg 2|c|$, the dominance of the quadratic Zeeman energy indicate the ground state near the Q_z pole with the energy gap $\Delta = 2\sqrt{q(q+2c)}$ [13], as known as the Polar phase. When $0 < q < 2|c|$, the ground state splits into two distributions with the energy gap $\Delta = 2\sqrt{c^2 - q^2/4}$, as know as the Broken-axis symmetry (BA) phase. This is the regime where the spin-nematic squeezing happens. The two special cases are $q = 0$, where the ground state is the maximum angular momentum Dicke state, and $q \to 2|c|^+$, where the ground state is an equilibrium squeezed state. The later one is the core of the research in this thesis. The black curve represents the separatrix (zero energy contour). Negative energy contours (blue) are inside the separatrix and positive energy contours (red) are outside.

Table 2.4: Commutation relationship for spin-1 operators.

$[\downarrow, \rightarrow]$	S_x	S_y	S_z	Q_{xz}	Q_{yz}	Q_{xy}	Q_{zz}	Q_{xx}	Q_{yy}
S_x	0	iS_z	$-iS_y$	$-iQ_{xy}$	$i(Q_{zz} - Q_{yy})$	iQ_{xz}	$-2iQ_{yz}$	0	$2iQ_{yz}$
S_y		0	iS_x	$-i(Q_{zz} - Q_{xx})$	iQ_{xy}	$-iQ_{yz}$	$2iQ_{xz}$	$-2iQ_{xz}$	0
S_z			0	iQ_{yz}	$-iQ_{xz}$	$i(Q_{yy} - Q_{xx})$	0	$2iQ_{xy}$	$-2iQ_{xy}$
Q_{xz}				0	iS_z	$-iS_x$	$-2iS_y$	$2iS_y$	0
Q_{yz}					0	iS_y	$2iS_x$	0	$-2iS_x$
Q_{xy}						0	0	$-2iS_z$	$2iS_z$
Q_{zz}							0	0	0
Q_{xx}								0	0
Q_{yy}									0

2.5 Quantum Approach

In this thesis, we consider the dynamics of a spin-1 condensate in a magnetic field oriented along the z direction and satisfying the single spatial mode approximation to be described by the Hamiltonian [11],

$$\hat{H} = \frac{c}{2N}\hat{S}^2 + \frac{q}{2}\hat{Q}_{zz}, \tag{2.33}$$

where $\hat{S}^2 = \hat{S}_x^2 + \hat{S}_y^2 + \hat{S}_z^2$ and $\hat{S}_\nu = \sum_{i=1}^N \hat{s}_\nu^i$ is a collective spin operator with $\hat{s}_\nu$ the corresponding single particle spin-ν component, and N is the total number of atoms. $\hat{Q}_{\nu\mu} = \sum_{i=1}^N \hat{q}_{\nu\mu}^i$ is a collective nematic operator, where $\hat{q}_{\nu\mu} \equiv \hat{s}_\nu\hat{s}_\mu + \hat{s}_\mu\hat{s}_\nu - (4/3)\delta_{\nu\mu}$ is a symmetric and traceless rank-2 tensor. The coefficient $c/(2N)$ is the collisional spin interaction energy per particle, with $c < 0$ for ^{87}Rb dictating a preferred ferromagnetic ordering (in this thesis $c = -|c|$ always), while $q = q_z B^2$ is the quadratic Zeeman energy per particle with $q_z/h = 71.6$ Hz/G^2. The QCP between the polar and the BA phases occurs at $q_c = 2|c|$. This is a second-order (continuous) quantum phase transition according to Ehrenfest's classification, which is akin to the phase transition in the Landau-Ginzburg model [25]. The corresponding polar phase ($q > q_c$) energy gap $\Delta(q) = \omega(q) = \sqrt{q(q - q_c)}$ between the ground state and the first excited state vanishes at the QCP in $N \to +\infty$ case.

We will consider the spin system to be prepared in an eigenstate of $\hat{S}_z$ with quantum number zero. Since the Hamiltonian commutes with $\hat{S}_z$, we may restrict $\hat{H}$ to the subspace of zero net magnetization. A suitable basis consists of the Fock states $|N_1, N_0, N_{-1}\rangle = |k, N - 2k, k\rangle =: |k\rangle$, $0 \le k \le \frac{N}{2}$ [26].

In this basis, the relevant matrix elements needed to construct the Hamiltonian matrix are

$$H_{k',k} = \langle k'|\hat{H}|k\rangle = \frac{c}{2N}\langle k'|\hat{S}^2|k\rangle + \frac{q}{2}\langle k'|\hat{Q}_{zz}|k\rangle. \tag{2.34}$$

$\langle k'|\hat{S}^2|k\rangle$ can be derived with the following relationship:

$$S^2 = S_+S_- - S_z + S_z^2, \tag{2.35}$$

where $S_+ = S_x + iS_y$, $S_- = S_x - iS_y$, $[S_x, S_y] = iS_z$, and $S_+S_- = S_x^2 + S_y^2 + S_z$. Because $\langle k'|S_z^2|k\rangle$ and $\langle k'|S_z|k\rangle$ equal zero,

$$< k'|S^2|k >=< k'|S_+S_-|k >= (S_-|k' >)^\dagger(S_-|k >). \tag{2.36}$$

The equation inside the brackets has the form:

$$\begin{aligned} S_-|k >=&\sqrt{2}(a_0^\dagger a_1 + a_{-1}^\dagger a_0)|k > \\ =&\sqrt{2}(\sqrt{k}\sqrt{N-2k+1}|k-1, N-2k+1, k > \\ &+ \sqrt{k+1}\sqrt{N-2k}|k, N-2k-1, k+1 >) \end{aligned} \tag{2.37}$$

following Table 2.1. Because the Fock states are orthogonal to each other,

$$\begin{aligned} (S_-|k' >)^\dagger(S_-|k >) = 2\Bigg[&\Big(2(N-2k)k + (N-k)\Big)\delta_{k',k} + \\ &(k+1)\sqrt{N-2k}\sqrt{N-2k-1}\delta_{k',k+1} + \\ &(k)\sqrt{N-2k+2}\sqrt{N-2k+1}\delta_{k',k-1}\Bigg]. \end{aligned} \tag{2.38}$$

The nematic operator matrix element is

$$< k'|Q_{zz}|k >= (4k - \frac{4}{3}N)\delta_{k',k}. \tag{2.39}$$

The dynamical evolution can be solved by the Schrödinger equation

$$i\hbar\partial_t|\Psi(t)\rangle = \hat{H}(q(t))|\Psi(t)\rangle$$

with the initial condition $|\Psi(t=0)\rangle = |0, N, 0\rangle$. The eigenstate and energy spectrum can be computed by directly diagnosing the matrix. Other observables can be also expressed in

the matrix form

$$\begin{aligned}\langle k'|S_x^2|k\rangle =&((2(N-2k)k+(N-k))\delta_{k',k}+\\ &(k+1)\sqrt{N-2k}\sqrt{N-2k-1}\delta_{k',k+1}+\\ &(k)\sqrt{N-2k+2}\sqrt{N-2k+1}\delta_{k',k-1}),\end{aligned} \tag{2.40}$$

$$\begin{aligned}\langle k'|S_y^2|k\rangle =&((2(N-2k)k+(N-k))\delta_{k',k}+\\ &(k+1)\sqrt{N-2k}\sqrt{N-2k-1}\delta_{k',k+1}+\\ &(k)\sqrt{N-2k+2}\sqrt{N-2k+1}\delta_{k',k-1}),\end{aligned} \tag{2.41}$$

$$\begin{aligned}\langle k'|Q_{xz}^2|k\rangle =&((2(N-2k)k+(N-k))\delta_{k',k}-\\ &(k+1)\sqrt{N-2k}\sqrt{N-2k-1}\delta_{k',k+1}-\\ &(k)\sqrt{N-2k+2}\sqrt{N-2k+1}\delta_{k',k-1}),\end{aligned} \tag{2.42}$$

$$\begin{aligned}\langle k'|Q_{yz}^2|k\rangle =&((2(N-2k)k+(N-k))\delta_{k',k}-\\ &(k+1)\sqrt{N-2k}\sqrt{N-2k-1}\delta_{k',k+1}-\\ &(k)\sqrt{N-2k+2}\sqrt{N-2k+1}\delta_{k',k-1}),\end{aligned} \tag{2.43}$$

and

$$\rho_0 = \sum_k^N \frac{N-2k}{N}\psi_k^\dagger\psi_k. \tag{2.44}$$

The commutation relations for the subspace are $\langle k'|[\hat{S}_x,\hat{Q}_{yz}]|k\rangle = i(6k-2N)\delta_{k',k}$ and $\langle k'|[\hat{S}_y,\hat{Q}_{xz}]|k\rangle = i(2N-6k)\delta_{k',k}$. At the condition where the initial state is $|0,N,0\rangle$, the commutation relationship gives the standard quantum limit $-\langle[\hat{S}_x,\hat{Q}_{yz}]\rangle = \langle[\hat{S}_y,\hat{Q}_{xz}]\rangle = i2N$.

The spinor phase shift $\Delta\theta_s$ is done by solving the equation

$$i\hbar\partial_t|\Psi(t)\rangle = \hat{Q}_{zz}|\Psi(t)\rangle,$$

which is equivalent to $|\Psi\rangle \rightarrow e^{-iQ_{zz}\Delta\theta_s/4}|\Psi\rangle$.

2.6 Entanglement

Entanglement is a very important quality for the many-body state. Here we mainly focus on connecting the experimental measurable quantities to the entanglement.

2.6.1 Fisher Information

The formal definition of multiparticle entanglementand can be presented via the Fisher information

$$F_Q = \sum_i 4\lambda(\Delta G)_i^2 - \sum_{i\neq j}\frac{8\lambda_i\lambda_j}{\lambda_i+\lambda_i}\langle\lambda_i|G|\lambda_j\rangle,$$

where $|\lambda_i\rangle$ is the eigenbasis with weight λ_i for the input state $\rho_{in} = \sum_i \lambda_i|\lambda_i\rangle\langle\lambda_i|$ [27]. In the spin-1 condensate case, $G = S_x$ is used to calculate the maximum F_Q.

2.6.2 Hellinger Distance

Hellinger Distance, also known as Euclidean distance in the space of probability amplitudes, is analyzed for extraction of the Fisher information [28]. Hellinger Distance is defined as

$$d_H^2(\theta) = \frac{1}{2}\sum_z[\sqrt{P_z(\theta)} - \sqrt{P_z(0)}]^2,$$

where $P_z(\theta)$ is the experimental probability distribution at angle θ. In spin-1 case, θ is the radiofrequency rotation angle (section 3.5). The observed quadratic behavior is expected from the Taylor expansion

$$d_H^2(\theta) = \frac{F_Q}{8}\theta^2 + \mathcal{O}(\theta^3).$$

This relationship is used to extract F_Q from the curvature of $d_H^2(\theta)$.

2.6.3 Entanglement Breadth

In the Bloch sphere operators [29, 30], the boundary of entangled atom number is labeled by the number k with the state

$$|\Psi\rangle = |\psi_k\rangle^{\otimes n} \otimes |\psi_p\rangle, \tag{2.45}$$

which is a product of n ($= [N/k]$, integer part of N/k) copies of state $|\psi_k\rangle$ containing k nonseparable spin-1 particles and state $|\psi_p\rangle$ composed of the remaining p ($= N - nk$) particles. The state $|\psi_\mu\rangle$ ($\mu = k, p$) represents the ground state of the μ particles Hamiltonian

$$H_\mu = (\hat{S}_z^{(\mu)})^2 - \lambda \hat{S}_x^{(\mu)}, \tag{2.46}$$

where $\hat{S}^{(\mu)} = \sum_{j=1}^{\mu} \hat{s}^j$. The boundary points are obtained as

$$\begin{aligned} \langle (\hat{S}_x^2 + \hat{S}_y^2 \rangle &= n \langle \hat{S}_x^{(k)2} + \hat{S}_y^{(k)2} \rangle_{|\psi_k\rangle} + n(n-1) \langle \hat{S}_x^{(k)} \rangle_{|\psi_k\rangle}^2 \\ &\quad + \langle \hat{S}_x^{(p)2} + \hat{S}_y^{(p)2} \rangle_{|\psi_p\rangle} + 2n \langle \hat{S}_x^{(k)} \rangle_{|\psi_k\rangle} \langle \hat{S}_x^{(p)} \rangle_{|\psi_p\rangle} \\ (\Delta \hat{S}_x)^2 &= n (\Delta \hat{S}_x^{(k)})_{|\psi_k\rangle}^2 + (\Delta \hat{S}_x^{(p)})_{|\psi_p\rangle}^2. \end{aligned} \tag{2.47}$$

The spin-nematic sphere operators are extended based on the result here and plotted in Figure 5.8.

CHAPTER 3

EXPERIMENTAL APPARATUS

An all-optical approach to making condensates was first pioneered in our laboratory in 2001 [7] and provided an alternative, simple and fast approach for preparing atomic condensates. Optical traps can provide tighter confinement for the atoms than a magnetic trap, and this can lead to higher density and efficient, fast evaporation in the trap. Our BEC machine consists of a simple vapor cell magneto-optical trap (MOT) [31, 32] and tightly focused CO_2 lasers. This chapter briefly describes our BEC experimental setup.

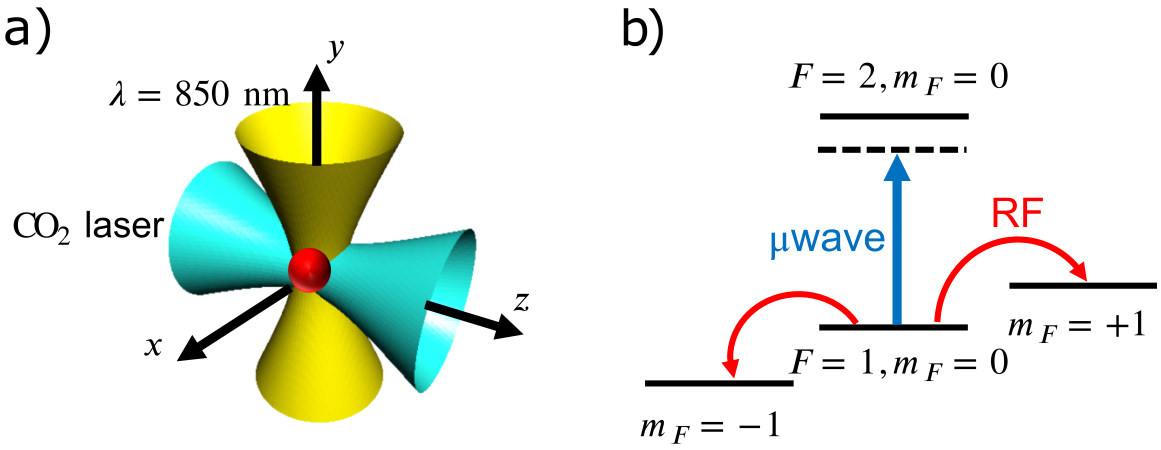

Figure 3.1: (a) An illustration of our apparatus. The optical trap is formed by a CO_2 laser ($\lambda = 10.6\,\mu\mathrm{m}$) in horizontal direction and a $\lambda = 850\,\mathrm{nm}$ laser in vertical direction. (b) The control of states is performed using the radiofrequency (RF) pulses and the detuned microwaves (μwave) pulses as shown in the figure.

3.1 External Cavity Diode Laser

One advantage of working with rubidium is that one can find inexpensive, high-power single-mode laser diodes and diode amplifier chips at 780 nm. Furthermore, the laser linewidth can be easily reduced to below 1 MHz and locked to atomic transitions following well-established external cavity diode laser (ECDL) techniques. The external cavity is

formed by the internal cavity controlled by the temperature and current of laser diodes and the external cavity formed by the grating reduces the linewidth of the laser below 1 MHz [33]. The cavity length is controlled by a piezoelectric actuator (PZT) (150V, Thorlabs) to change the output wavelength. The aspheric lens is used to collimate the output beam. The proportional gain from the laser locking feedback will be input into the current of laser diodes while the integral gain will be added to the PZT.

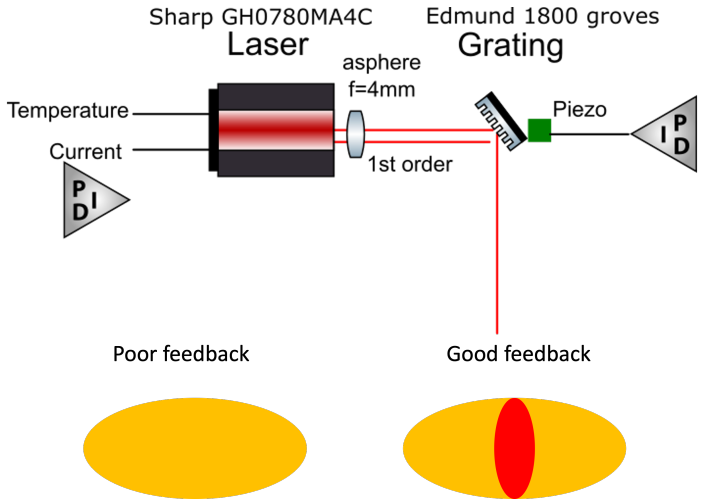

Figure 3.2: The laser diode is mounted in an electrostatic discharge (ESD) protection and strain relief cables (Thorlabs SR9B). The grating is 1800 lines/mm from Edmund optics. The 1st order diffraction is retro-reflected to the diode to form the external cavity. The grating is aligned at a low current with the lasing beam showing the bright central oval distribution.

The temperature controller of laser diodes uses 10 kΩ thermistors (Thorlabs) and 100 kΩ thermistors (home-built) with thermoelectric coolers (TEC) of $R = 4.27\ \Omega$. This allows the temperature to be stabilized to an accuracy of 3 mK level.

3.1.1 $\lambda = 780$ nm laser: frequency stabilization and tuning

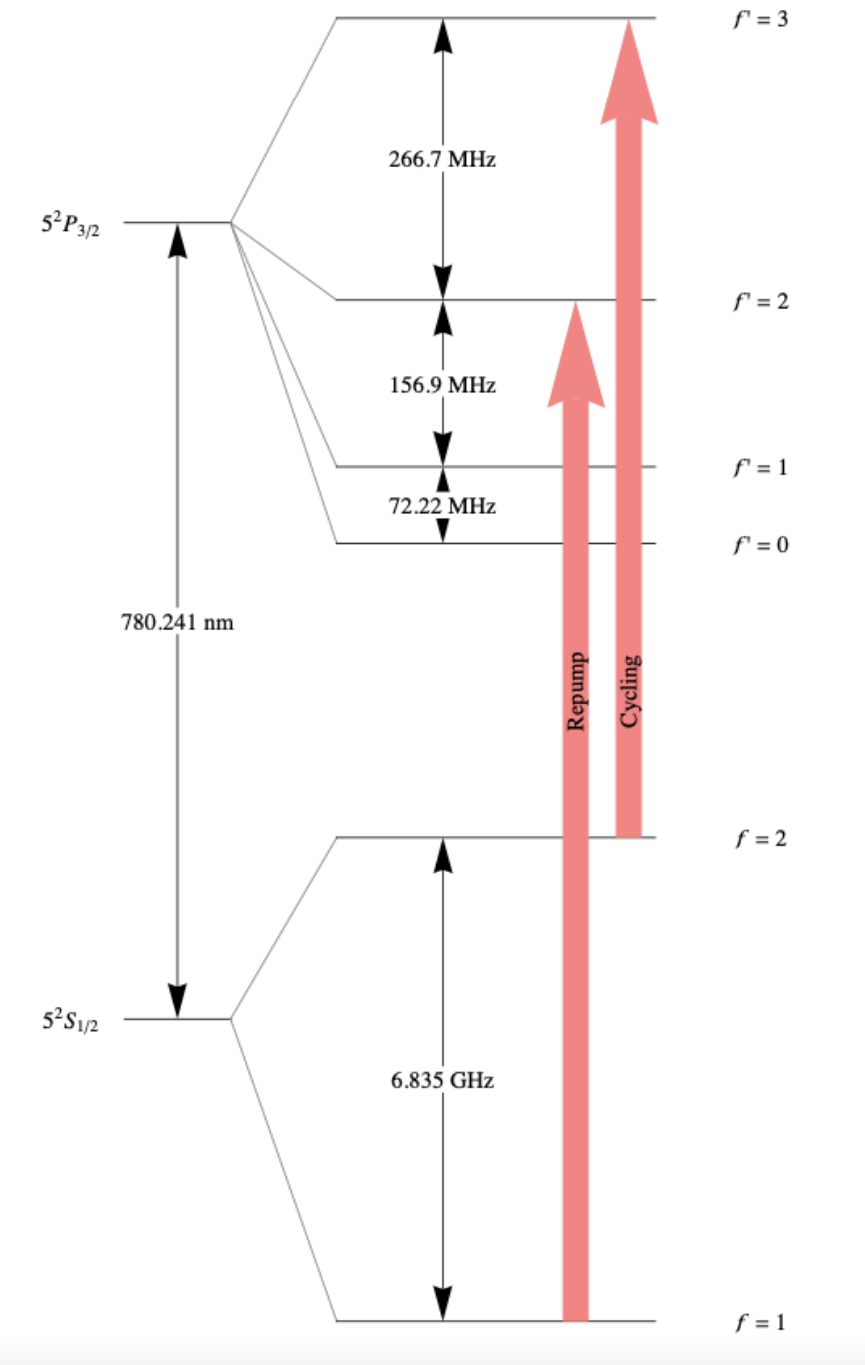

Figure 3.3: ^{87}Rb D_2 transition hyperfine structure [22, 34].

Doppler laser cooling requires the cooling lasers to be frequency stabilized to the red of the cycling transition ($F = 2 \rightarrow F' = 3$). In the experiment, the master laser frequency

is locked to the cross over of $F = 2 \rightarrow F' = 3$ and $F = 2 \rightarrow F' = 1$ transitions (see Figure 3.5), which is -211.8 MHz below the cycling transition. The master laser is locked to a Doppler-free atomic absorption signal obtained from a standard saturated absorption spectrum setup (satspec) as illustrated in Figure 3.4. To change the detuning of the locked master laser, a frequency tunable acoustic optical modulator (AOM) is configured in a double-pass configuration and the output laser beam of the AOM is then injected to lock a slave laser. The slave laser is then inputted into a taped amplifier (TA) to solve the power-inefficiency and then coupled into three fibers that contribute to the three orthogonal beams for laser cooling. The typical beam waist for optimal fiber coupling is 350 μm.

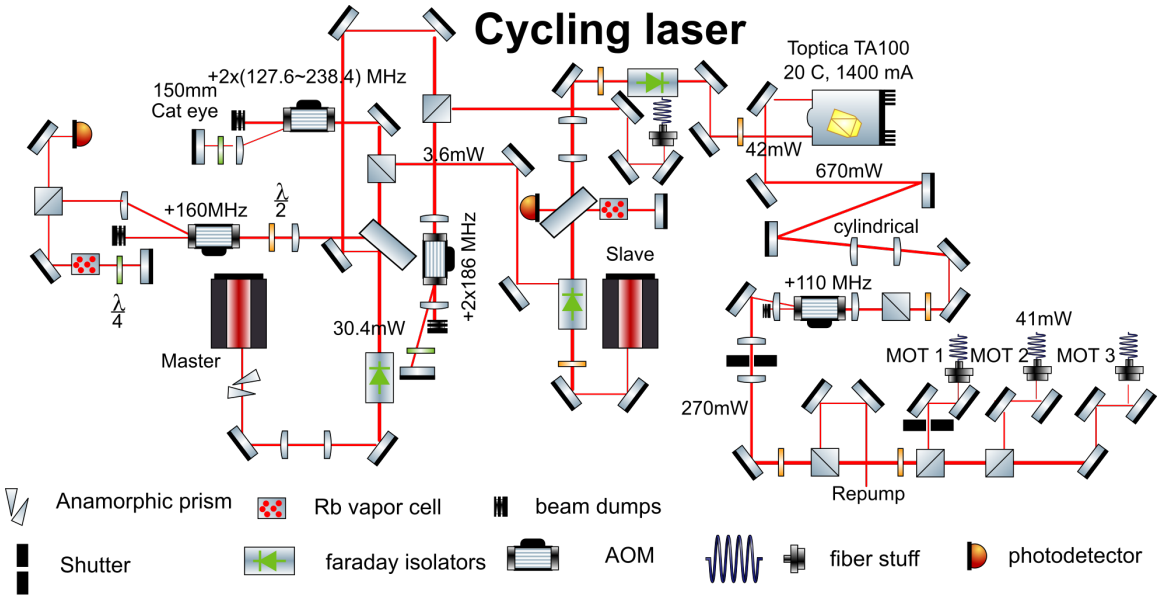

Figure 3.4: The master laser is input into the output beam cube of an optical isolator with the polarization perpendicular to the slave laser. The cat-eye structure for the double-pass AOM is used to minimize the beam walking during the frequency change stage so that the slave laser follows the master laser constantly [35]. The shutters (UNBLITZ) are used together with the AOM power control to fully turn off beams.

The tunable frequency range relative to the cycling transition can be calculated as below. $f_{detuning} = [-226.6, -5]$ MHz $= -211.8$ MHz (Master lock 3,1 cross over) -160 MHz (AOM before satspec) $+[127.6, 238.4]$ MHz (Double pass AOM range measured with counter) -110 MHz (AOM isomet 233A-1 after TA). This detuning range allows us to

achieve sub-Doppler cooling in the final stage of MOT.

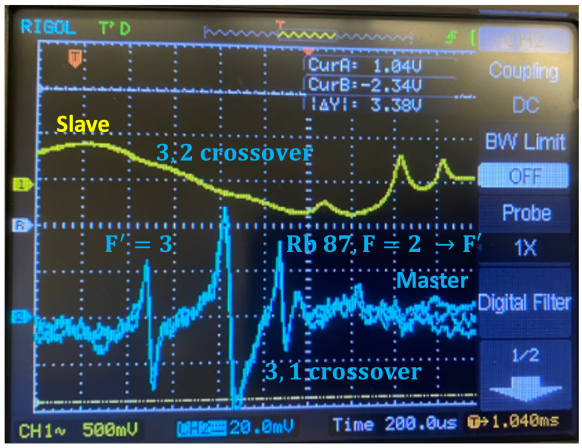

Figure 3.5: Cycling transition spectra: the blue trace is the error signal for the master laser and the yellow trace is the satspec for the slave laser. The master and slave laser is detuned by $[-116.5, 105]$ MHz which is the reason of a displacement between two traces.

Although the lasers are tuned close to the cycling transition, there is a small probability that the atoms can be excited to the $F' = 2$ state, which can spontaneously decay to the $F = 1$ ground state. Due to the large ground-state hyperfine splitting, atoms in the $F = 1$ states are decoupled from the cycling light. To repump these atoms, a second resonant laser of the $F = 1 \rightarrow F' = 2$ transition is added to optically pump the atoms back to the $F = 2$ state - this is referred to as the repump laser.

The repump laser does not need to change frequency; it is locked to the crossover of $F = 1 \rightarrow F' = 2$ and $F = 1 \rightarrow F' = 1$ transitions (see Figure 3.7) and then shifted to resonant frequency of $F = 1 \rightarrow F' = 2$ transition using an AOM that also controls the power.

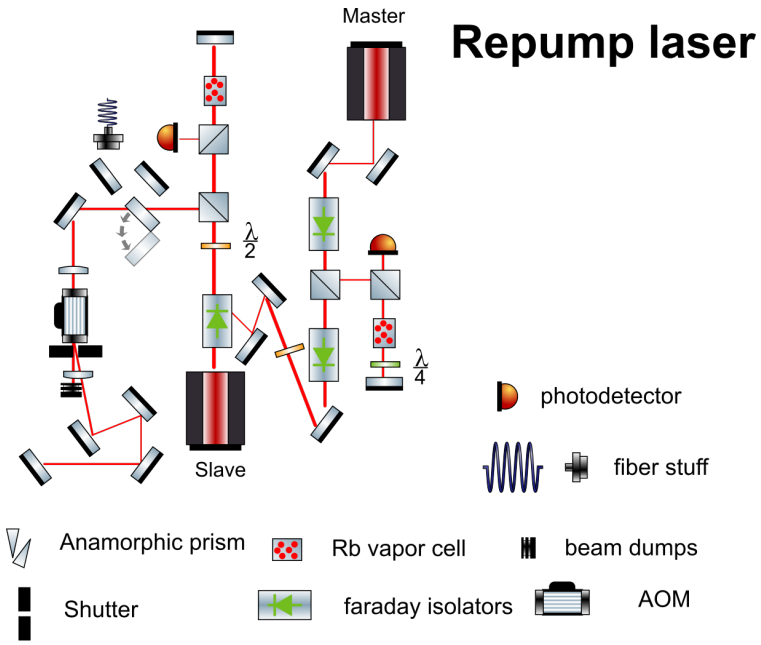

Figure 3.6: The slave laser has a flip mirror to send the light through a multi-mode fiber. This is used to check the injection lock of the slave laser to the master laser.

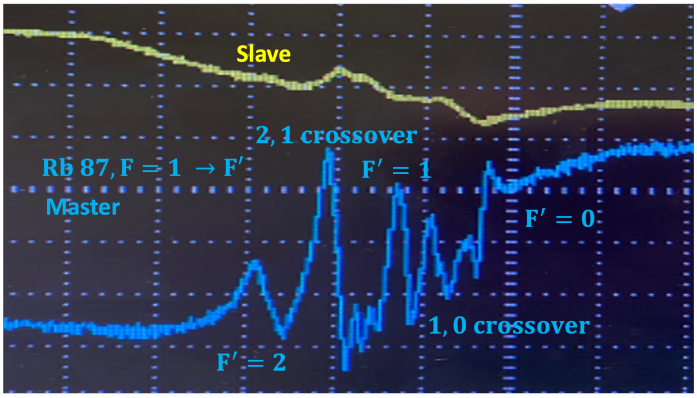

Figure 3.7: Repump transition spectra: the blue trace is the error signal for the master laser and the yellow trace is the satspec for the slave laser. The master and slave laser is not detuned.

The experiment requires three beams of cycling laser. After existing the fiber, each laser beam is expanded, collimated, and then circularly polarized to favor $\sigma^{\pm}$ transitions ($\Delta m = \pm 1$) through retro-reflection. The beam power of each fiber output is an important indicator to solve the experimental issues, which is detailed in Table 3.1. The repump beam power is very sensitive to the small change since it's strongly attenuated by the AOM during

the dark MOT cooling stage.

Table 3.1: The beam power for cycling and repump lasers of each fiber output.

Fiber output	Cycling TA (mW)	Repump slave (mW)
MOT1	39.3	7.4
MOT2	41.2	2.1
MOT3	41.8	2.7

Steps of checking laser

1. Check the grating feedback at low current.
2. Check the wavelength with the optical spectrometer (HP 86142A) to adjust grating to the correct angle.
3. Adjust to the current of typically used laser power, use the (infrared) IR scope to observe fluorescence.
4. Use the satspec for fine tuning.

3.1.2 Laser lock characterization

The laser frequency is stabilized to an absorption peak using frequency modulation (FM) spectroscopy by locking it to a zero-crossing point of the error signal using a proportional (P) and integral (I) circuit. The setup for the FM spectroscopy using current modulation is shown in Figure 3.8. There are also other configurations such as the AOM modulation.

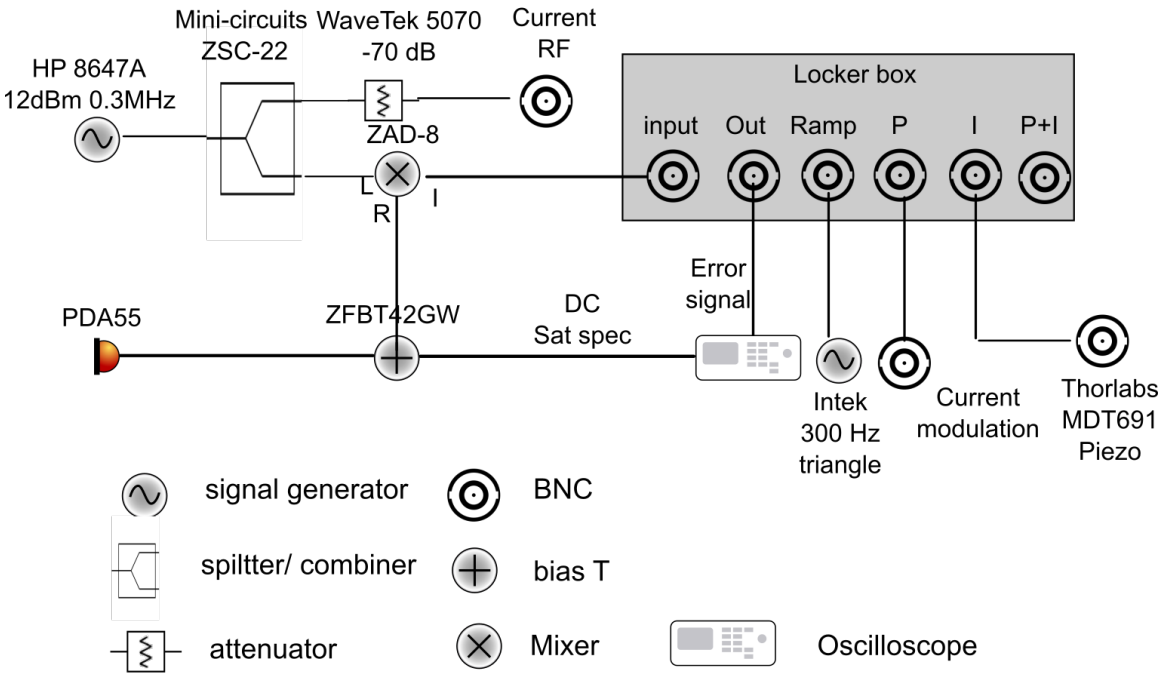

Figure 3.8: The current modulation signal from the signal generator (HP 8647A) is split into two paths. One path is further attenuated and sent into the laser current controller for current modulation. The other path is mixed with the high frequency (AC) part from the detector. Thus the high-frequency signal is demodulated into the low frequency (DC) error signal which goes into the home-built locker box. The piezo scan modulation comes from the ramp channel. P and I channels are connected to the current modulation and piezo modulation as a feedback loop.

The first step to check if the laser is locked is by using the wavemeter (High Finesse WS-7L) to see if the frequency is changed before and after the lock. The more precise measurement of the lock quality is studied below.

Fabry–Pérot interferometer [36]

The laser beam is aligned through the cavity with single-mode, which is verified by a webcam [37]. The cavity length is scanned through the piezo which allows finding the resonance length. Multiple beams are coupled into the same fiber so the alignment only needs to be done once.

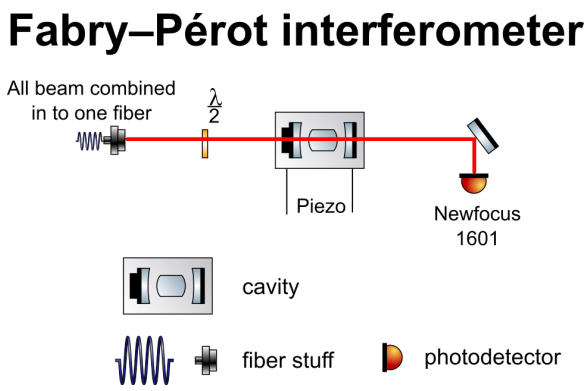

Figure 3.9: Fabry–Pérot cavity (Etalon) is formed by a partially reflecting flat mirror pair. The transmission will be maximum when $\lambda = 2L/n$, where L is the length of the cavity and n is an integer.

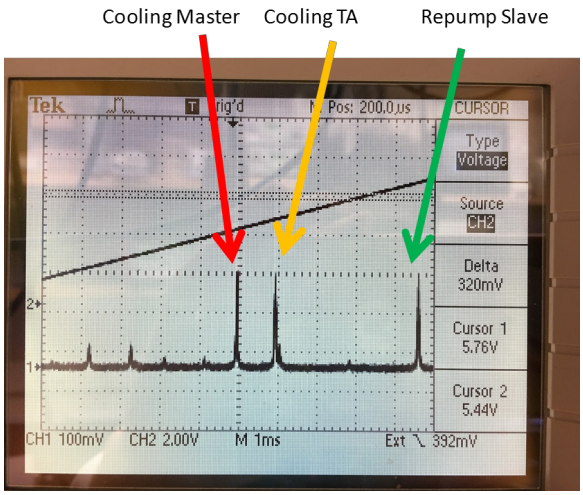

Figure 3.10: The transmission of different lasers (unused AOM 0th order) is studied on the same cavity.

The frequency width of the transmission peaks is known as the linewidth of the cavity:

$$\Delta\nu_{/2} \approx \frac{c\pi}{2LT},$$

where T is the transmitted fraction. Unfortunately, the product of LT for the cavity is only large enough for us to observe at 10 MHz resolution. As a result, we move to the heterodyne measurement to further detect at 1 MHz stability.

Heterodyne

The heterodyne measurement [37] involves two locked lasers to form an interferometer [38]. One laser is side locked by the satspec without frequency modulation as the reference, the other one is with modulation and locked by the error signal. Those two lasers are different by center frequency thus the interference between them generates a beat note. The linewidth of the beat note depends on the laser locking quality.

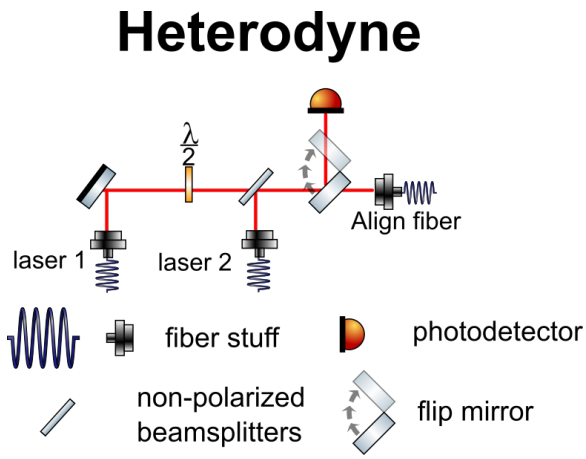

Figure 3.11: Heterodyne setup. The two lasers are maximally overlapped by coupling to the same fiber. The flip mirror will reflect the interference into a high bandwidth (1GHz) detector. The half-wave plate and non-polarized beam splitter are used to maximized the interference signal by having the electromagnetic wave vectors in the same direction. The signal out of the detector is sent into a spectrum analyzer to look at the linewidth of the beat note.

The result from the heterodyne measurement indicates that the current modulation needs to be strongly attenuated to have a narrow linewidth lock, while the error signal gets smaller at the same time.

As discussed earlier, if the FM spectroscopy is done by modulating the AOM, the modulation strength will play a significantly less role.

3.1.3 $\lambda = 850$ nm laser

In order to create the tightly confined optical dipole trap to confine the condensate smaller than the spin-healing length, a laser with a wavelength of 850 nm is applied in the vertical

direction during the last stage of the experiment. The light is in the regime of the far-off-resonant trap and the power is controlled by the AOM. There is no need to lock the laser frequency in this case.

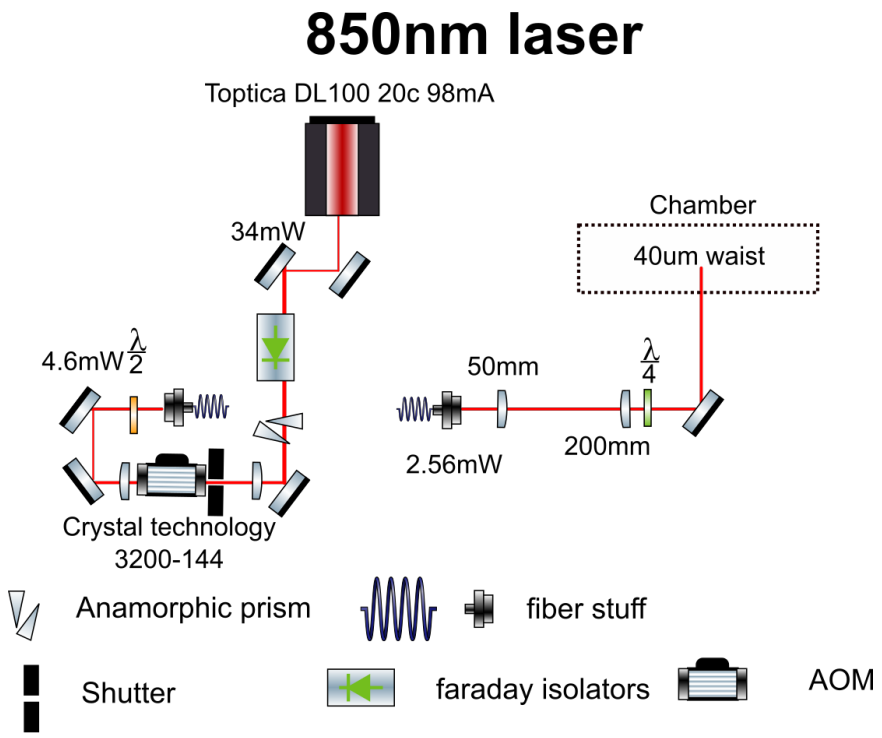

Figure 3.12: The $\lambda = 850$ nm laser light is fiber-coupled to a fixed focus setup aligned as a cross with the main trapping beam. This beam requires delicate alignment since its 40 μm waist must intersect the 20 μm waist of the main dipole trapping beam.

3.2 Vacuum systems

The experiments are performed inside of an ultra-high vacuum (UHV) chamber of an octagonal design from Kimball physics. The chamber has two large glass windows on 6" flanges and five smaller glass windows on 2.75" ports. These glass windows are all broad-band anti-reflection coated for the near-infra-red wavelengths. There are two zinc selenide (ZnSe) 2.75" windows to pass the 10.6 μm of the main optical trapping laser. On the final 2.75" port there is a connection to the dispenser feed-through and vacuum pumps which has another glass window on the far side of the apparatus.

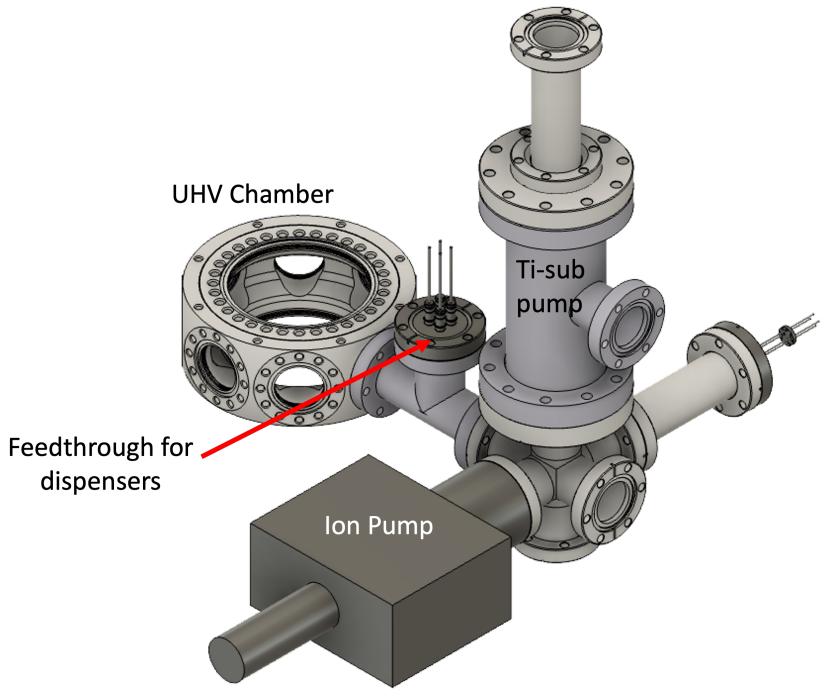

Figure 3.13: Diagram of the experimental setup. An ion pump and a titanium sublimation (Ti-sub) pump are used to maintain the chamber at UHV pressure. The detail of the optical components inside the chamber is discussed in section 3.4 and section 3.7.

3.2.1 Dispenser

The source of rubidium comes from dispensers (SAES) mounted on an electrical feed-through. The electrical feed-through is used to run current (between 4.5 A and 7.5 A) through the dispenser which heats them (500 C$^{\circ}$) causing the release of rubidium into the chamber. Also, the rubidium already in the chamber is recycled by using light intensity assisted de-adsorption which is accomplished by shining bright blue (455 nm wavelength) LEDs onto the windows of the chamber.

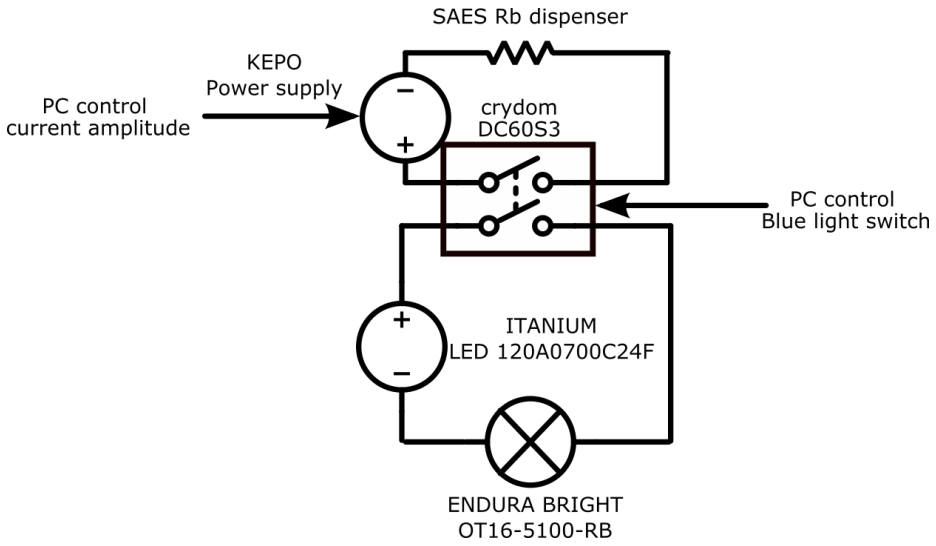

Figure 3.14: The dispenser control circuit. The current amplitude passing through the dispenser is remotely controlled and the switch of dispenser current and blue LEDs are correlated by a solid-state relay. The switch-off is important during the experimental sequence since the dispenser itself generates a non-negligible magnetic field.

3.2.2 Water cooling

Water cooling is essential to the apparatus to avoid overheating and potential fire hazards. The high-power coils used to generate magnetic gradients are cooled by room-temperature water while the CO_2 laser components and microwave amplifiers are cooled by chilled water. To prevent incorrect steps of operation, a couple of in-line flow switches (Gems FS-380P) are installed and connected to the interlocks of devices.

Table 3.2: Water-cooled devices. The tap water requires a regularly changed filter to be used as a cooling source. The Chiller (HASKRIS WW2) input pressure is 35 psi and the output pressure is 30 psi. The temperature is set to 17 C°. The tank is filled with a 10% solution of laboratory-grade (99%) propylene glycol with distilled water to prevent biological growth. The detail about each components is discussed in section 3.3 and section 3.4.

Method	Tap water	Chiller water
Application	MOT and SG coils	CO_2 laser, AOM, beam blocker, microwave amplifier
pressure (psi)	70	30

3.2.3 Air control

The high-pressure (70 psi) air is used to float the optical table and control pneumatic devices. The aperture (Clippard SSR-05-4, PQ-CC08N, EV-3-6VDC) for imaging is controlled by the airflow. The purpose of pneumatic devices is stated in section 3.7.

3.3 Magnetic Coils

Several sets of magnetic coils are employed to control the magnetic field and field gradient in the experiment. The MOT coils (anti-Helmholtz) are used to provide a gradient to trap atoms at the beginning of experiments. In addition to the MOT coils, there are three orthogonal pairs of Helmholtz coils (trim coils) used to cancel the Earth's magnetic field and other stray magnetic fields. However, since the coils are not all in perfect Helmholtz configuration due to the geometry and relative position change of condensates, the field produced by the trim coils is not necessarily uniform. A pair of weaker anti-Helmholtz coils (Aux coils) is used to add or compensate a field gradient along the horizontal trap (z) direction. This pair of Aux coils proved to be important in our spinor studies. During the imaging and the state preparation process, Stern-Gerlach (SG) coils are used to purify the spin component of the condensate and spatially separate spin components.

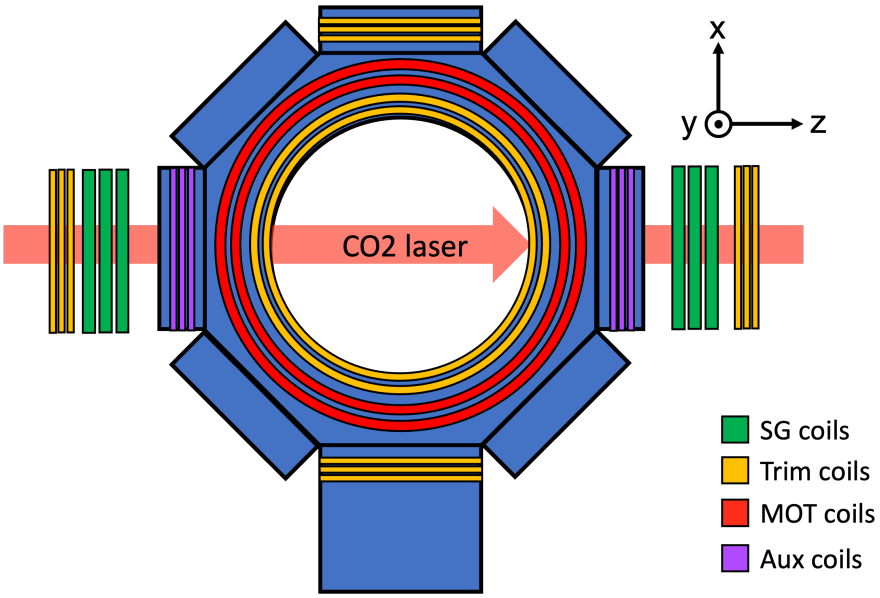

Figure 3.15: The layout of the magnetic coils (top view).

3.3.1 Trim coils

The polynomial expansion for the field of Helmholtz coils at the origin is [39]

$$B_z = B_0 + az^2 + \cdots ,$$

where

$$B_0 = n\frac{\mu_0 I R^2}{(R^2 + A^2)^{3/2}} \tag{3.1}$$

$$a = n\frac{3(4A^2 - R^2)}{2(R^2 + A^2)^2}B_0. \tag{3.2}$$

R is the coil radius, A is half of the spacing of the coils, and n is the number of turns. For optimum uniformity, the spacing of the coils must be equal to the radius $R = 2A$. The dimension of the trim coils in the experiments is stated in Table 3.3.

Table 3.3: The geometry of the trim coils. The calculated B_0/I agrees with the experimental (Exp) measured result through the radiofrequency spectrum of BECs.

	Trim X (imaging axis)	Trim Y (vertical axis)	Trim Z (CO_2 axis)
Power supply	Newport 525	Newport 5060	The boss bipolar 20-20-1
R (")	1.35	3	1.75
A (")	3	2.5	7
n	15	15	90
B_0/I (mG/A)	379.88	1121.51	363.00
Exp (mG/A)	301.89	1178.63	298.40
a/B_0 (1/cm^2)	0.0678	0.0160	0.0165

The field zeroing is important to the spinor experiments since the magnetic field determines the quadratic Zeeman energy which competes with the spin-spin collision term. The number of points of field measurements can be reduced to 7 points to calibrate the field accurately. The trim coil current is controlled by the voltage from the computer, the field measured in the Larmor precession frequency will be fitted to the model:

$$f = 70.24(\text{ kHz}/100\text{ mG}) \cdot \sqrt{(\frac{V_x - V_{x0}}{V_{xprop}})^2 + (\frac{V_y - V_{y0}}{V_{yprop}})^2 + (\frac{V_z - V_{z0}}{V_{zprop}})^2},$$

where V_{i0} is the zero-field voltage and V_{iprop} is the linear coefficient between voltage and field. If the microwave transition is used to measure the field, the coefficient needs to be changed from 70.24 into 69.96 (kHz$/100$ mG).

3.3.2 Gradient coils

The magnetic field gradient is provided by a pair of anti-Helmholtz coils. Near the center of between coils, the field can be expanded into polynomial series of z [39],

$$B_z(z) = bz + cz^3 + \cdots,$$

where

$$b = \frac{\mu_0 I R^2}{2} \frac{6A}{(A^2 + R^2)^{5/2}} \tag{3.3}$$

$$c = \frac{5(4A^2 - 3R^2)}{6(A^2 + R^2)^2} b. \tag{3.4}$$

The gradient in all three directions generated by the anti-Helmholtz coils are related by Gauss's law for magnetism:

$$\frac{\partial B_x}{\partial x} = \frac{\partial B_y}{\partial y} = -\frac{1}{2}\frac{\partial B_z}{\partial z}.$$

Table 3.4: The geometry of the gradient coils. MOT coils and SG coils use a large current to generate sufficient gradients that are required. As a result, they are water-cooled to avoid being overheated. For MOT coils, we also use $1/4$" copper tubing for tap water cooling, the resistance $R = R_{coil} + R_{leads} = 20 + 6.7 = 26.7$ mΩ. The total power cost is $P = 600$ W. For SG coils, we use $1/4$" copper tubing for tap water cooling, The resistance is $R = R_{coil} + R_{leads} + R_{IGBT} + R_{shunt} = 28 + 1.5 + 11 + 0.5 = 41$ mΩ. Aux coils are used to zero the gradient during the spin mixing dynamics.

	Aux Gradient (CO_2 axis)	MOT (vertical axis)	SG (CO_2 axis)
Power supply	Newport 525	EMS	ESS 15-1000-2
I (A)	1.025	112.6	300
R (")	1.35	3.25	1.5
A (")	4	2.5	4.5
n	9	9	21
$\partial B_z/\partial z$ (mG/cm)	29.3	13491.8	15521.83
$\partial B_x/\partial x$ (mG/cm)	14.7	6745.9	7760.9

Aux coils calibration

Empirically, we have found that in order to observe well-characterized spin dynamical evolution, it is necessary to zero the magnetic field gradient along the z axis (CO_2 laser

axis). To measure the gradient, we perform magnetic field measurements using the condensate carefully translated to different z positions. The cloud is displaced spatially by changing the lens mover position, which will change the focus point of the CO_2 laser (see section 3.4). The range of translation is 150 μm measured via absorption imaging.

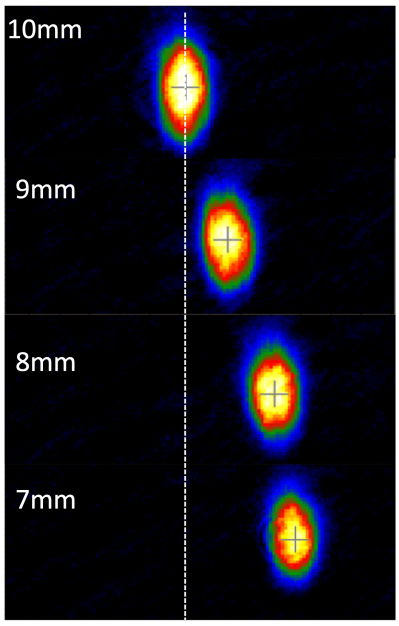

Lens mover (mm)	Distance (pixel)	Distance (μm)
10	421	0
9	435	47.43
8	450	98.02
7	477	189.28

Figure 3.16: The spatial movement of BECs. By changing the final moving distance of the lens mover, the optical trap focus position is changed accordingly which is measured precisely using the absorption imaging method.

At each spatial location, an RF spectroscopy is performed to measure the local z direction magnetic field.

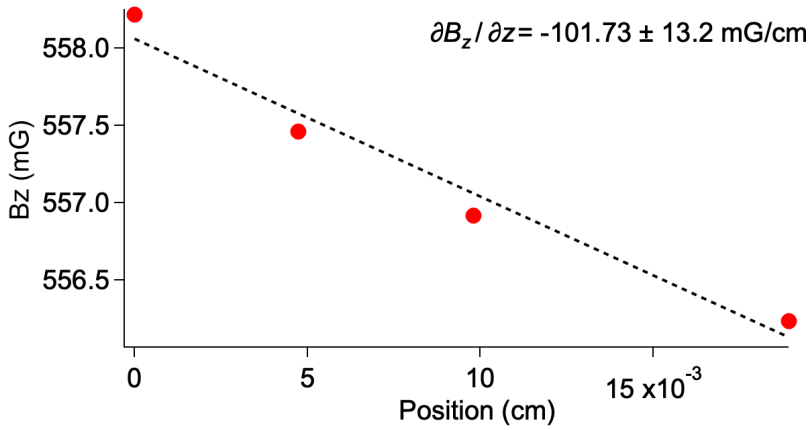

Figure 3.17: Local B_z is measured for the condensate carefully translated to different z positions and $\partial B_z/\partial z$ is determined through a linear fit to the data. The estimated error of the magnetic field from RF spectroscopy is smaller than the size of markers.

The magnetic field gradient is measured at different Aux coil currents. By linear interpolating the data, a zero gradient point can be found within 10 mG/cm precision.

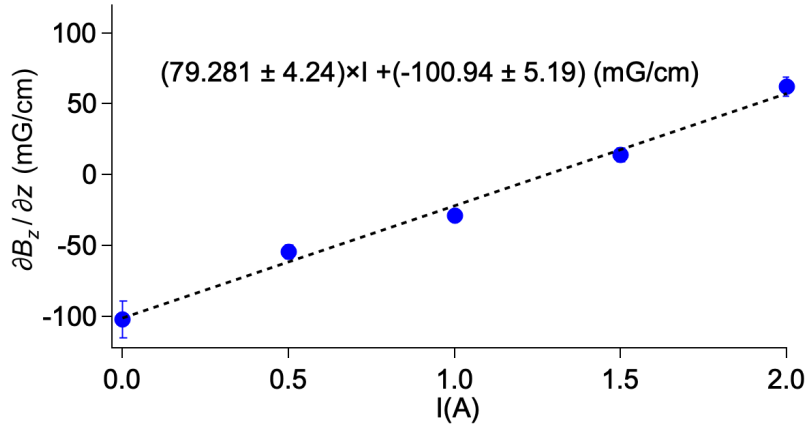

Figure 3.18: Measurement of $\partial B_z/\partial z$ versus the current I in Aux coils. We use those coils to cancel the ambient gradient to < 10 mG/cm.

Another way to see the effect of the gradient is to look at the geometric shapes of $m_F = \pm 1$ atoms after holding the condensate inside the trap for a relatively long time (200 ms). This method does not have a very quantitative indication of the zero gradients so it is not the major method used in this thesis.

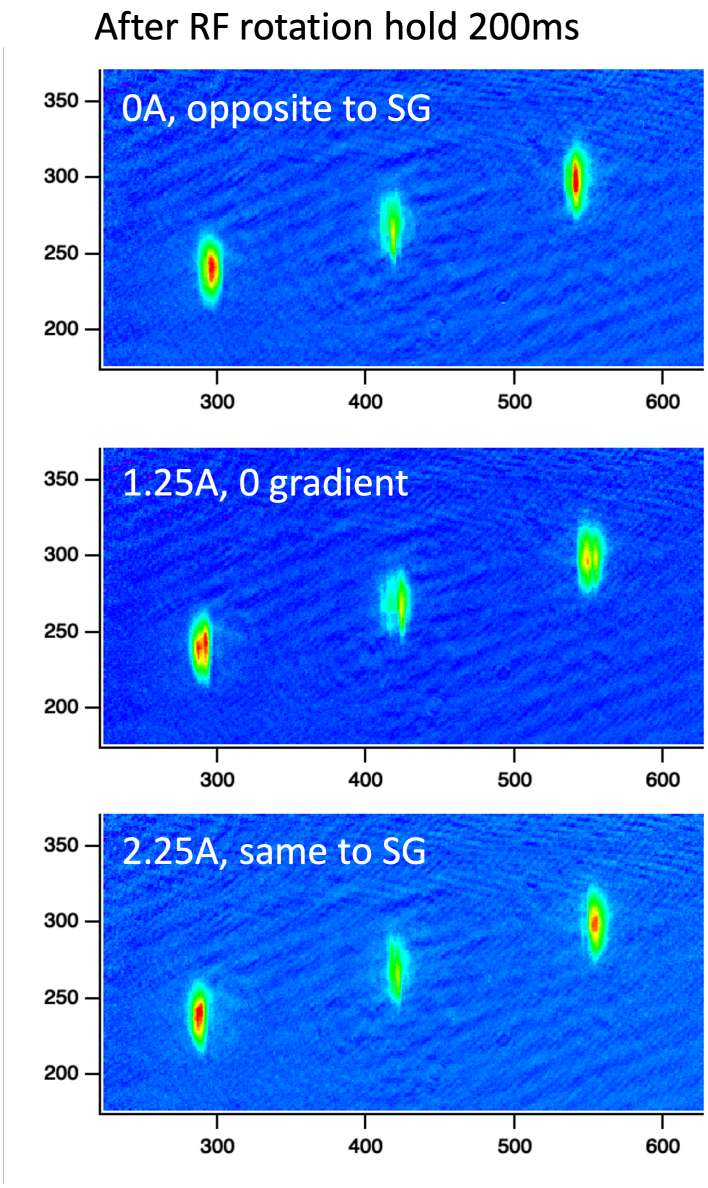

Figure 3.19: An RF rotation is done to have an equal population of atoms in all three Zeeman components. If the existing gradient is in opposition to the direction of the SG gradient, then the ± 1 atoms will have the partial lunar eclipse structure facing inward. When the gradient direction is the same as the SG gradient, the shape faces outward. At zero gradient, domains will be observed.

3.3.3 IGBT circuits

The SG coils are connected with an insulated-gate bipolar transistor (IGBT) for fast switching on and off. The entire circuit is redesigned compared to the previous version for better

protection of the newly purchased power supply (TDK-Lambda 20-500) and faster turning off time. The maximum power setting is in constant voltage mode with $V = 20$V and $I = 460$A. The switching on time is about 1 to 2 ms and the switching off time is about 1 ms at the max power setting.

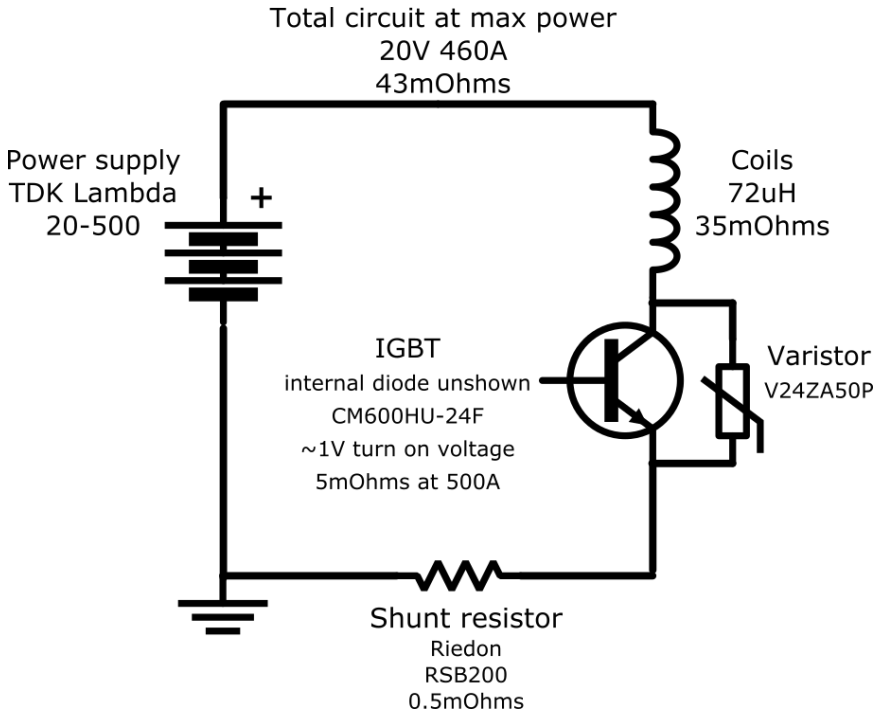

Figure 3.20: IGBT circuit. The ground is connected next to the shunt resistor so that the current passing through the coils can be directly measured using the voltage across the shunt resistor. Another way to measure the current is to use the inductive probe. The main component that absorbs the current from immediately switching off is the varistor, which requires a monthly replacement.

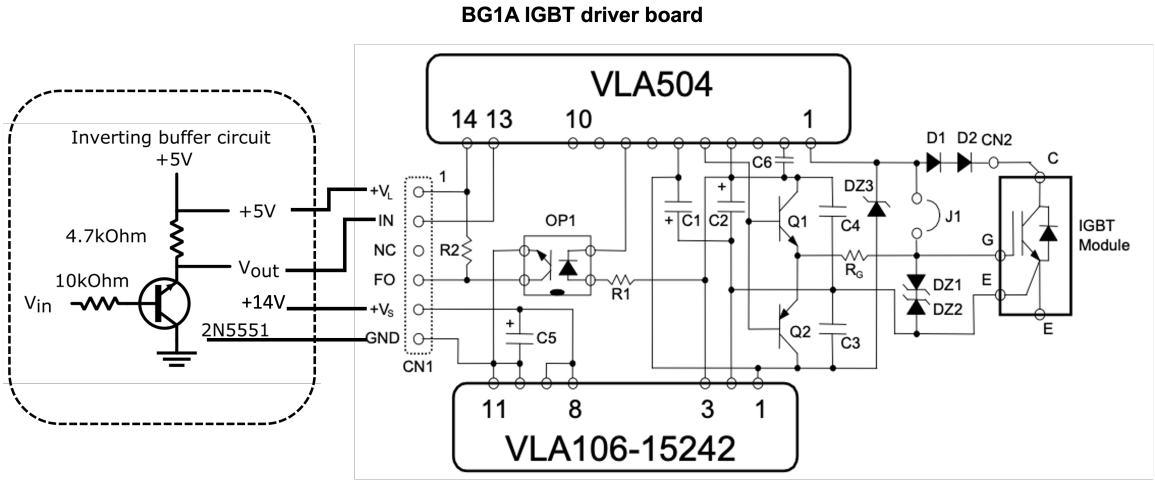

Figure 3.21: The input switch signal from the computer passes an inverting buffer circuit to control the IGBT on and off.

3.4 Optical dipole trap

The key to reaching Bose condensation in an all-optical dipole trap (ODT) is efficient loading in a tight confining potential for subsequent evaporative cooling. The tight confinement in the optical trap can lead to high densities and high collision rates, however, the tight confinement will also cause a small trap volume. Therefore, a large trap volume is desired for creating larger stable condensates. As a result, a motorized translation stage (lens mover) is implemented into the optical path to achieve the large trap volume at the beginning of the experiment and a high density at the last stage of the experiment as shown in Figure 3.22.

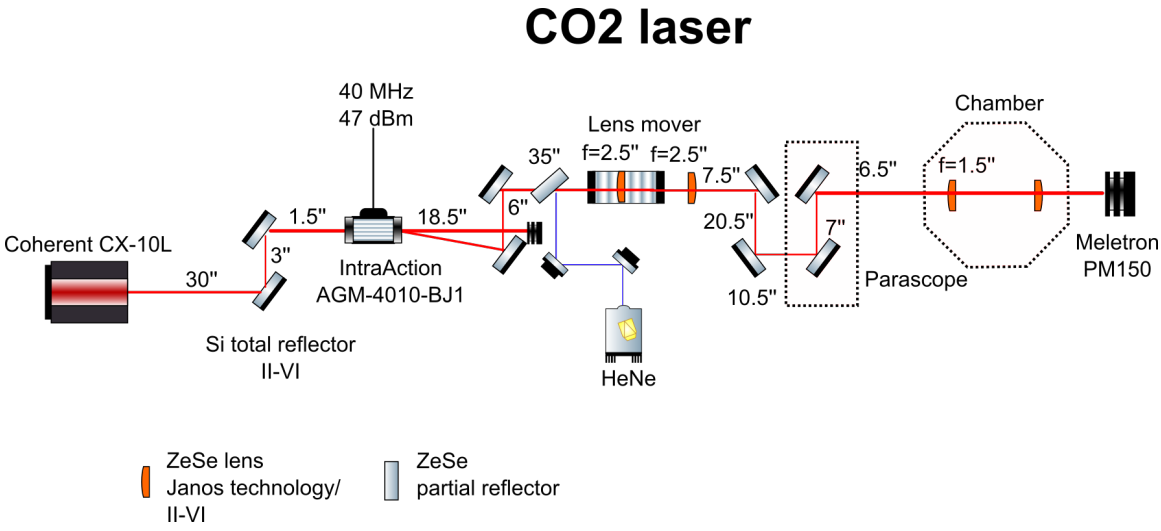

Figure 3.22: The CO_2 laser we are using is Coherent CX-10L 10.6 laser system with RF module assembly. For this model, we only need to connect it to a DC power supply. The mirror we are using is Si/Ge total reflector $d = 1.5''$ and $t = 0.160''$ from II-VI company. The beam splitter/combiner and lens are made with ZeSe. The IntraAction AOM has the following specs: G=germanium, 40=40 MHz, 10=10 mm aperture, 1=10.6 μm coating. A 165 W optical power with a 7 mm optical beam diameter (3.5 mm beam waist) works for the AOM. From the Diamond laser manual, a 7 mm beam diameter is at about 80 cm from the laser (7.5 mrad $1/e^2$ full angle divergence). In the experimental setup, the important distance is laser head to AOM 34.5"=87.63 cm, laser head to lens mover 94"=238.76 cm, and lens mover to chamber 52"=132.08 cm. The helium-neon (HeNe) laser is used to assist the alignment of the CO_2 laser.

There is a power loss for the CO_2 laser after each optical component, Table 3.5 is shown for future reference.

Table 3.5: Power loss for the CO_2 laser at the maximum power.

Location	Power (W)
Before AOM	165
After AOM, RF off	145
After AOM, RF on, 1st order	120
After lens mover	118
After chamber	95

The laser power control is done by the RF power of the AOM. The initial RF signal

(40 MHz, -17.4 dBm) is preamplified by ZFL-100GH (30 dB), where this preamplification can be voltage-controlled by a computer. A switch (ZYSWA-2-50DR) is added afterward before going to a 39 dB amplifier (LZY-1). The resonance of the AOM is at 40 MHz. The sensitivity of RF frequency versus first-order diffraction power is plotted below.

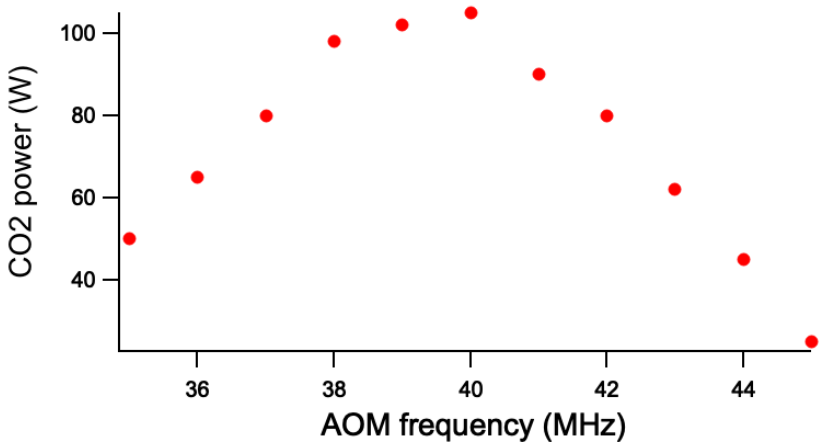

Figure 3.23: The 1st order of diffraction power after AOM as a function of the RF frequency.

The power of the CO_2 laser is calibrated after the AOM using different detectors (Meletron PM150, etc) for different power regimes and fitted with polynomials as listed in Table 3.6 and Table 3.7.

The lens mover is used to change the beam waist of the beam entering the chamber. Here the origin of the position is based on the label on the translation stage (ESP300) which is a relative 0. The beam waist is measured by a graphite razor blade while the CO_2 laser is operated at low power.

Table 3.6: CO_2 laser power calibration table 1.

AOM control voltage (V)	CO_2 laser power first order (W)
300 W range, 150W detector	
0	122.1
0.1	121.5
0.2	118.8
0.3	118.8
0.4	117.9
0.5	113.1
0.6	104.76
0.7	92.13
0.8	76.86
100W range	
0.85	69.3
0.9	60.8
0.95	52
1	44
1.05	36.9
1.1	30.52
1.15	25
1.2	20.32
1.25	16.49
30W range	
1.3	13.26
1.35	10.62
1.4	8.451
1.45	6.774
1.5	5.37
10W range	
1.55	4.26
1.6	3.3383
1.65	2.7
1.7	2.186
1.75	1.77
1.8	1.45
3W range	
1.85	1.176
1.9	0.975
1.95	0.813
2	0.681
2.05	0.5685
2.1	0.4926

Table 3.7: CO_2 laser power calibration table 2.

AOM control voltage (V)	CO_2 laser power first order (W)
1W range	
2.15	0.398
2.2	0.32
2.3	0.23
2.4	0.179
2.5	0.14
300mW range	
2.6	0.0972
2.7	0.081
100mW range 3W detector	
2.8	0.059
2.9	0.047
3	0.0379
3.1	0.0312
3.2	0.0258
3.3	0.0215
3.4	0.0181

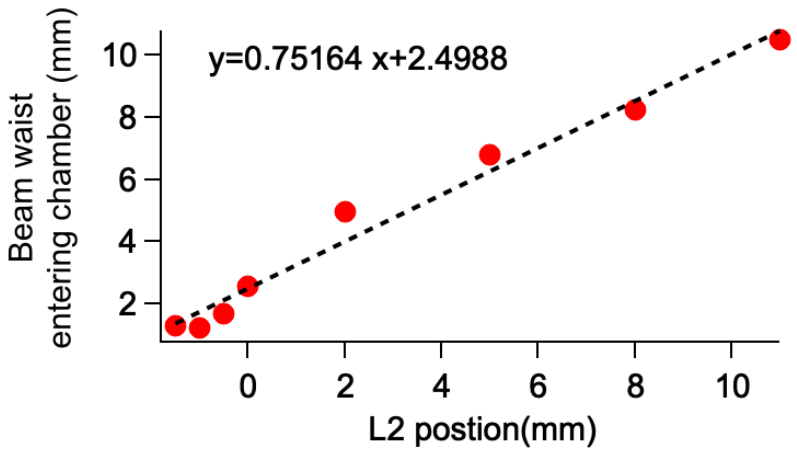

Figure 3.24: The beam waist of the CO_2 laser entering the chamber as a function of the distance between the two lenses controlled by the lens mover. Using this measurement, the beam waist of the focused Gaussian beam inside the chamber can be estimated [40].

We begin by collecting up to 15 M cold atoms in a simple vapor cell ^{87}Rb MOT, which is overlapped with a large volume single focus trap. Up to 4 M atoms are loaded into the optical trap. Once the atoms are loaded into the trap, the effectiveness of the evaporative cooling is determined by the ratio of elastic collision within trapped atoms versus other bad

collisions with untrapped background residual gas molecules. It is therefore important to achieve a high elastic collision rate in a short time. In order to accomplish that, the trap is compressed immediately after loading. The lens mover is programmed with the following parameters in Table 3.8 and takes $T = 1.0417$ s to finish the entire ramp. The input beam waist w_{in} is modeled as a function of time based on the linear fit from Figure 3.24 as plotted in Figure 3.25.

Table 3.8: The controlling parameters for the lens mover.

Start time	400 ms
Start position	0mm
Acceleration	40 mm/s^2
Deceleration	40 mm/s^2
Velocity	15mm/s
Travel for	10mm

The waist of the focus point is related to the input beam waist by $w_{min} = \lambda_{dipole} f/(\pi w_{in})$. Here f is the focus of the lens. The maximum intensity of a Gaussian beam is a function of both power P and w_{min}: $I_{max} = \frac{2P}{\pi w_{min}^2}$. The CO_2 power ramp is a piece-wise linear function. The Rayleigh range, low trap frequency, high trap frequency and mean trap frequency are defined as $z_r = \frac{\pi w_0^2}{\lambda}$, $\omega_L = \sqrt{\frac{2U_0}{m z_r^2}}$, $\omega_H = \sqrt{\frac{4U_0}{m w_0^2}}$, and $\bar{\omega} = (\omega_L \omega_H^2)^{1/3}$ accordingly [40]. The trap potential is calculated by

$$U(r) = -\frac{3\pi c^2}{2\omega_0^3}\frac{\Gamma}{\Delta} I(r),$$

where $|\Delta| = |\omega - \omega_0|$ is the detuning. ω and ω_0 are the angular frequency of the dipole trap laser and the cycling laser. The potential is converted into temperature units using $U = k_B T$ by assuming it is a 2D harmonic trap. The elastic two-body collision rate is computed as $\gamma_{el} = N(8\sqrt{2}\frac{a^2 m}{\pi k_B})\frac{\bar{\omega}^3}{T}$, where $a = 100.4 a_0$.

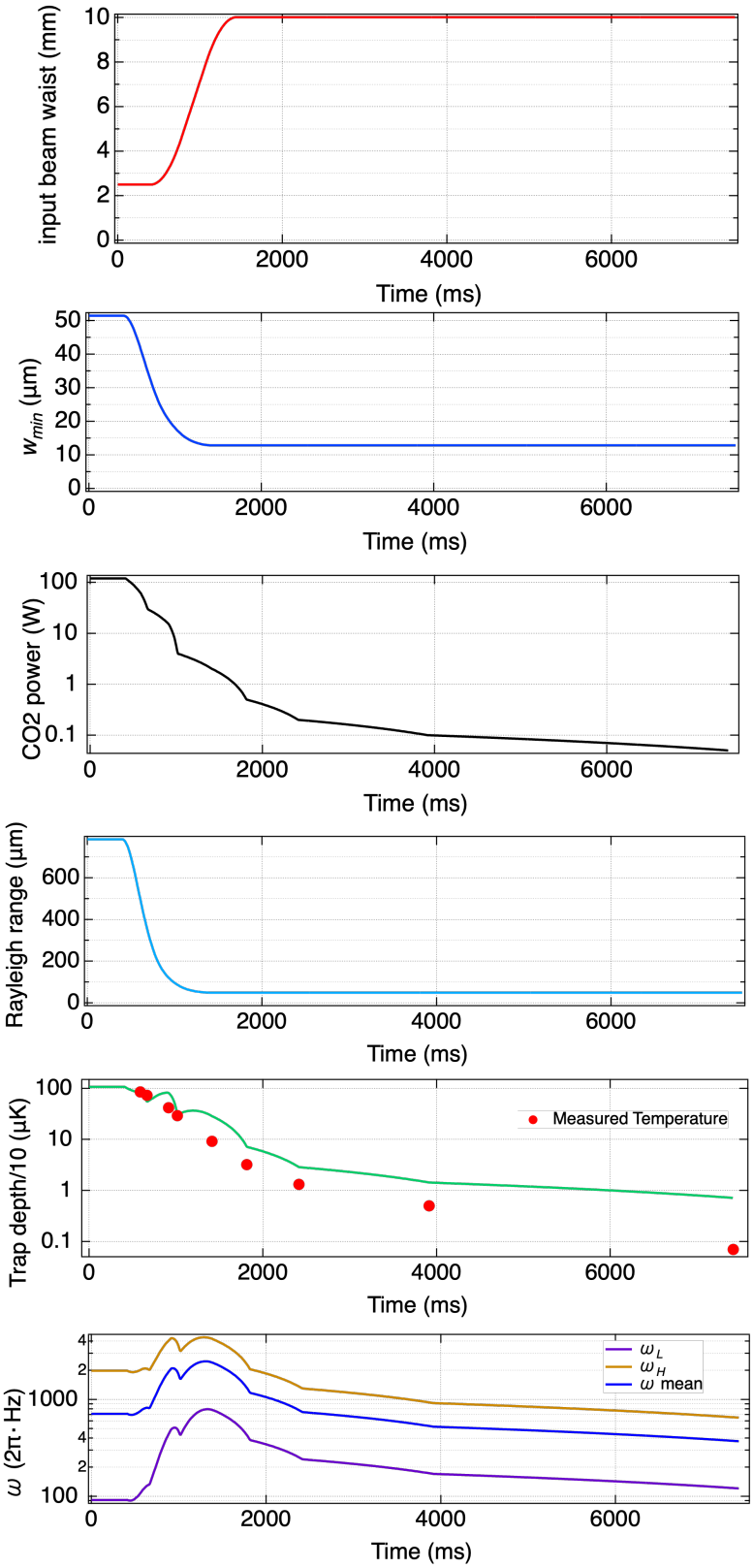

Figure 3.25: Dipole trap parameters as a function of time.

To simultaneously force evaporation, the laser power is ramped down during the compression. A typical chosen ramp of laser power is shown in Figure 3.26 along with the temperature and atom number measured at each power step using fluorescence imaging and absorption imaging.

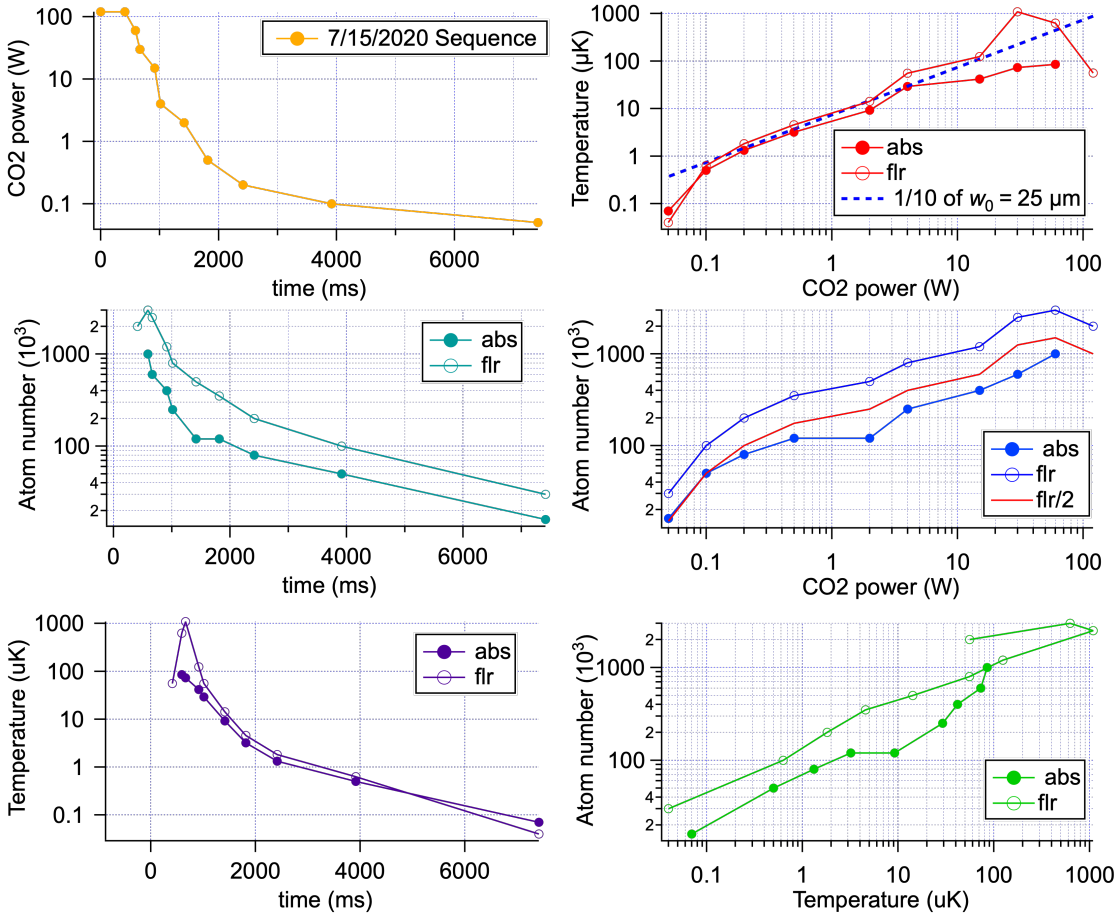

Figure 3.26: The temperature and atom number are measured at each CO_2 laser power step. The length of each power ramp step is optimized to achieve high atom number and low temperature. The last couple of steps is optimized by the condensate fraction. There is a discrepancy in the atom number measured by the fluorescence (flr) imaging and the absorption imaging (abs) but the temperature measurement agrees with each other. The atom number is the max during the time of flight (TOF) and the temperature is measured with 0.1 to 5 ms TOF (see subsection 3.8.1).

Steps of checking CO_2 laser

1. Check the AOM RF source is turned on.

2. Check switch power + pre-amplifier power supply is turned on. The pre-amplifier is sensitive to the supply voltage change.

3. Check the chiller to see if water is still running.

3.5 Radiofrequency systems

Whereas the lasers primarily interact with the electric dipole moment of the valence electron, oscillating magnetic fields can be used to interact with the magnetic dipole moment of the valence electron and to a much lesser extent with the nuclear magnetic moment. The radiofrequency (RF) pulses transfer atoms between Zeeman sub-levels of given hyperfine states. Atoms are coupled by a simple coil placed on top of the chamber centered on the large window. A new RF coil is made with a larger diameter to reduce the interference with the microwave antenna.

Table 3.9: RF coil diameter d and the number of turns for both the old coil and the new coil.

Old coil	New coil
$d = 3$", 9 turns	$d = 5$", 20 turns

The RF coil is directly driven by the Sigelent function generator which is controlled by the pulse generator to switch on for precision of μs using its built-in function. The typically required frequency varies with the magnetic field but is around 100 kHz order. The voltage across the resistor is used as a method to measure the current across the coil. The previous version of the RF system has a switch and a capacitor in the circuit. The reason to get away from the switch is that it clamps the pulse at high voltage input. The capacitor is no longer needed because we do not need the extra resonant LC circuit to achieve enough power for the RF operation.

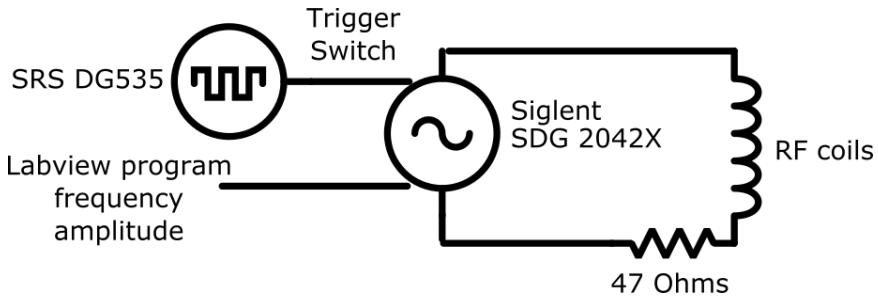

Figure 3.27: The circuit of the RF system. A 47 Ω resistor in the circuit is for the 50 Ω impedance matching.

For the RF transitions, we will look at the simple three-level system in the $F = 1$ manifold. The initial Hamiltonian is:

$$H_0 = \hbar \begin{pmatrix} -\Delta + \delta & 0 & 0 \\ 0 & 0 & 0 \\ 0 & 0 & \Delta + \delta \end{pmatrix}, \tag{3.5}$$

where Δ is the linear Zeeman shift and δ is the quadratic Zeeman shift. RF transitions only occur through the transverse component and so the perturbing Hamiltonian is the B_x portion of the oscillating magnetic field:

$$H_B = \hbar\Omega \cos(\omega_B t) \frac{1}{\sqrt{2}} \begin{pmatrix} 0 & 1 & 0 \\ 1 & 0 & 1 \\ 0 & 1 & 0 \end{pmatrix}, \tag{3.6}$$

where Ω is the strength of the field and ω_B is the frequency of the oscillating magnetic field. Under the interaction picture,

$$H'_B = \hbar\Omega \cos(\omega_B t) \frac{1}{\sqrt{2}} \begin{pmatrix} 0 & e^{i(-\Delta+\delta)} & 0 \\ e^{-i(-\Delta+\delta)} & 0 & e^{-i(\Delta+\delta)} \\ 0 & e^{i(\Delta+\delta)} & 0 \end{pmatrix}. \tag{3.7}$$

If we expand the cosine and make the rotating wave approximation (RWA)

$$H'_B \approx \hbar\Omega \frac{1}{\sqrt{2}} \begin{pmatrix} 0 & e^{i\delta_+ t} & 0 \\ e^{-i\delta_+ t} & 0 & e^{-i\delta_- t} \\ 0 & e^{i\delta_- t} & 0 \end{pmatrix}, \tag{3.8}$$

where $\delta_\pm = \omega_B - \Delta \pm \delta$. In the case that the quadratic Zeeman energy can be neglected ($\delta = 0$) and no detuning $\omega_B = \Delta$, the solution of the Schrödinger equation is [24]

$$\psi(t) = \begin{pmatrix} \frac{1}{2}(1+\cos(\Omega t)) & \frac{i}{\sqrt{2}}\sin(\Omega t) & -\frac{1}{2}(1-\cos(\Omega t) \\ \frac{i}{2}\sin(\Omega t) & \cos(\Omega t) & \frac{i}{2}\sin(\Omega t) \\ -\frac{1}{2}(1-\cos(\Omega t) & \frac{i}{\sqrt{2}}\sin(\Omega t) & \frac{1}{2}(1+\cos(\Omega t)) \end{pmatrix} \psi(0). \tag{3.9}$$

With the initial population of atom all in $|F = 1, m_F = 0\rangle$ ($\rho_0 = N_0/N = 1$), a resonant RF pulse will transfer all atoms from $|m_F = 0\rangle$ to $|m_F = \pm 1\rangle$ as shown in Figure 3.28. The data is fitted by

$$\rho_0(t) = A(\cos(2\pi t/T + \phi))^2 + b$$

to extract the Rabi rate T.

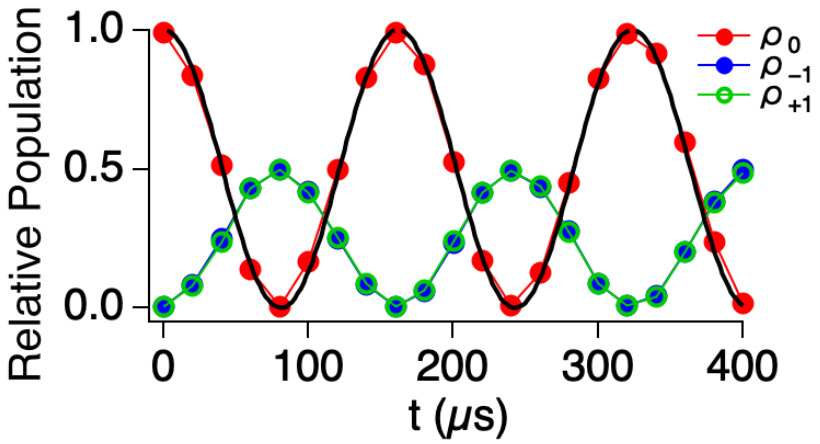

Figure 3.28: RF Rabi. The on-resonance RF pulse transfer all atoms from $|m_F = 0\rangle$ to $|m_F = \pm 1\rangle$ at $\pi/2$ period. After π period, all atoms are transferred back to $|m_F = 0\rangle$. Here $\rho_{0,\pm 1} = N_{0,\pm 1}/N$.

To detect the resonant transition frequency, the interaction time is held at the estimated π pulse time and a frequency scan is performed. If the field is carefully calibrated, then the resonance is around $f = 702.4\,\text{Hz/mG} \cdot B$. In reality, the resonance is measured to calibrate the field. The resonance is measured by fitting the data with

$$\rho_0(f) = [1 - \frac{\Omega^2}{\Omega^2 + (f_0 - f)^2}(1 - \cos(T\sqrt{\Omega^2 - (f_0 - f)^2}))] + b,$$

where Ω is the strength of the field and T is the pulse length.

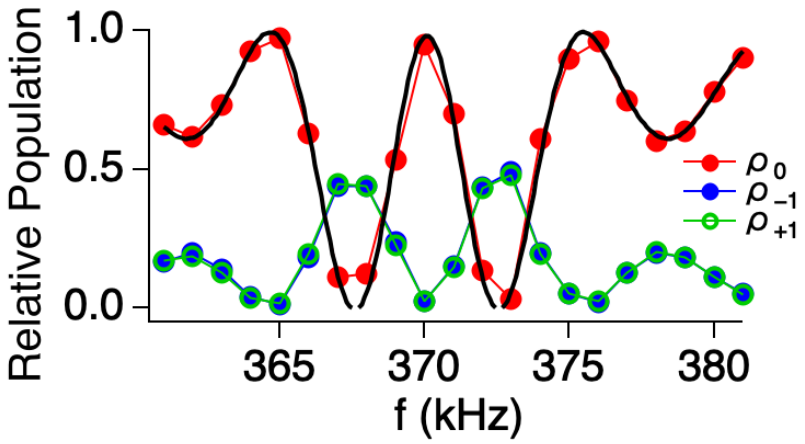

Figure 3.29: RF spectrum. The pulse length uses the estimated π period to determine the resonance. The spectrum and the Rabi rate may need to be iterated alternatively to get the precise result.

3.6 Microwave system

A microwave transition transfers atoms between sub-levels of the hyperfine structure of $F = 1$ and $F = 2$. The microwave transition can be approximated as a 2-level system, for instance, the microwave transition between $|F = 1, m_F = 0\rangle$ and $|F = 2, m_F = 0\rangle$, which shifts the spinor phase of the condensate quantum states. Moreover, the microwave spectroscopy of $\pm\Delta$ transition can be used to measure the magnetic field.

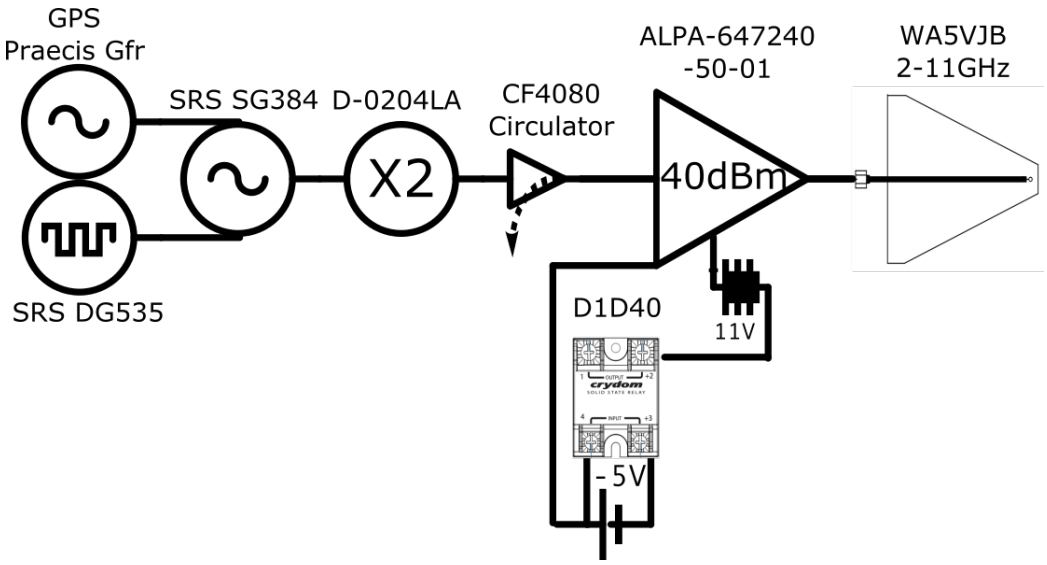

Figure 3.30: The circuit of the microwave system. The microwave system no longer uses the switch to further simplify the circuit. The turning on/off is controlled by the internal function of SRS SG384. Because the internal switch only works for the 2 to 4 GHz range (SRS SG384 is capable of generating up to 8 GHz wave), a frequency doubler needs to be in place. The circulator works as an isolator while at the same time monitoring the power reflected from the amplifier. The microwave source needs to be locked by the remote clock from GPS 10 MHz sources. The extra relay setup is for the safety of the high-power amplifier. The amplifier will not be powered until the required -5 V is on. All cables and components have their own insertion loss, the power measured with the spectrometer is around 37 dBm out of the amplifier and close to saturation.

Here we will solve the two-level system between the states $|F = 1, m_F = 0\rangle$ and $|F = 2, m_F = 0\rangle$ as a general example of the microwave transitions. The initial unperturbed Hamiltonian is

$$H_0 = \hbar \begin{pmatrix} \omega_1 & 0 \\ 0 & \omega_0 \end{pmatrix}, \tag{3.10}$$

where $\omega_1 - \omega_0 = \omega_{hfs}$. ω_{hfs} is the 6.8 GHz hyperfine splitting. B is assumed in the z direction for simplicity and the interaction picture is used

$$H'_B = e^{iH_0 t/\hbar} H_B e^{-iH_0 t/\hbar} = \hbar\Omega \cos\omega_B t \begin{pmatrix} 0 & -e^{i(\omega_1-\omega_0)t} \\ -e^{i(\omega_0-\omega_1)t} & 0 \end{pmatrix}. \tag{3.11}$$

Expanding the cosine into exponential and making the RWA give

$$H'_B \approx \hbar\frac{\Omega}{2}\begin{pmatrix} 0 & -e^{i\delta t} \\ -e^{-i\delta t} & 0 \end{pmatrix}. \tag{3.12}$$

A second interaction picture transfers the Hamiltonian into a static matrix:

$$H''_B = e^{\frac{iH'_0 t}{\hbar}} H'_B e^{\frac{-iH'_0 t}{\hbar}} = -\hbar\frac{\Omega}{2}\begin{pmatrix} 0 & 1 \\ 1 & 0 \end{pmatrix}, \tag{3.13}$$

where

$$H'_0 = \hbar\begin{pmatrix} -\frac{\delta}{2} & 0 \\ 0 & \frac{\delta}{2} \end{pmatrix}. \tag{3.14}$$

By applying the Euler formula of Pauli matrix exponential $e^{i\alpha(\vec{n}\cdot\vec{\sigma})} = \cos\alpha + i(\vec{n}\cdot\vec{\sigma})\sin\alpha$, the solution of the Schödinger equation gives

$$\begin{aligned} \psi' =& e^{-iH'_0/\hbar t} e^{-i(H''_B - H'_0)t/\hbar}\psi'(0) \\ =& e^{i\delta\sigma_z t/2} e^{i(\Omega\sigma_x - \delta\sigma_z)t/2}\psi'(0) \\ =& e^{i\delta\sigma_z t/2}[\cos(\alpha) + i\sin(\alpha))(\vec{n}\cdot\vec{\sigma})]\psi'(0), \end{aligned} \tag{3.15}$$

where $\alpha = \sqrt{\Omega^2+\delta^2}t/2$, $\vec{n} = (\Omega/\sqrt{\Omega^2+\delta^2}, 0, -\delta/\sqrt{\Omega^2+\delta^2})$. With the initial population in the $|F=1, m_F=0\rangle$ state, the solution becomes

$$\psi_{1,0} = (\cos(\alpha) + i\sin(\alpha)\frac{\delta}{\sqrt{\Omega^2+\delta^2}})e^{-i\delta t/2}.$$

For a π rotation, $t = 2\pi/\sqrt{\Omega^2+\delta^2}$ and the phase shift is $\Delta\theta_{1,0} = -(1+\frac{\delta}{\sqrt{\Omega^2+\delta^2}})\pi$.

Experimentally, the parameter we measured is the Rabi rate T from the fitting to the resonant clock transition in Figure 3.31. The relative parameters can be calculated based

on $\Omega = 2/T$ (in Hz unit), $\Delta\theta_s = -2\Delta\theta_{1,0}$,

$$\delta = \frac{\Omega}{\sqrt{1-(-\theta_s/2\pi-1)^2}}(-\frac{\theta_s}{2\pi}-1), \tag{3.16}$$

and the new Rabi rate $T(\delta) = 2/\sqrt{\Omega^2+\delta^2}$.

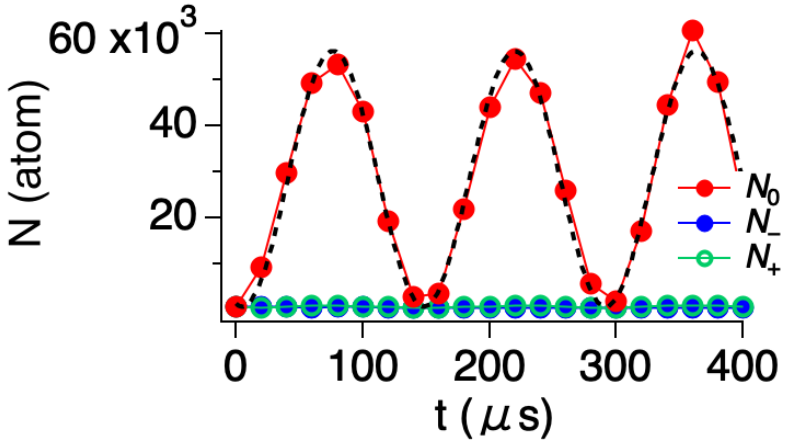

Figure 3.31: Microwave clock transition Rabi rate $|F=1, m_F=0\rangle \leftrightarrow |F=2, m_F=0\rangle$. The repump laser needs to be off for the clock transition. The absolute atom number is used instead of the relative atom number to show the population in $|F=2, m_F=0\rangle$.

To be able to shift the spinor phase θ_s precisely, the quadratic Zeeman effect needs to be accounted for. The hyperfine splitting is calculated using the Breit-Rabi formula [22]. The clock transition between $|F=1, m_F=0\rangle$ and $|F=2, m_F=0\rangle$ has the energy difference

$$\begin{aligned}\Delta_E = E_{20} - E_{10} &\approx E_{hfs} + \frac{1}{2}\frac{(g_J\mu_B)^2}{E_{hfs}}B^2 \\ &= 6834682610.9 \text{ Hz} + 572.8 \text{ Hz/G}^2 \cdot B^2.\end{aligned} \tag{3.17}$$

The resonance of the clock transition needs to be adjusted depending on the magnetic field B.

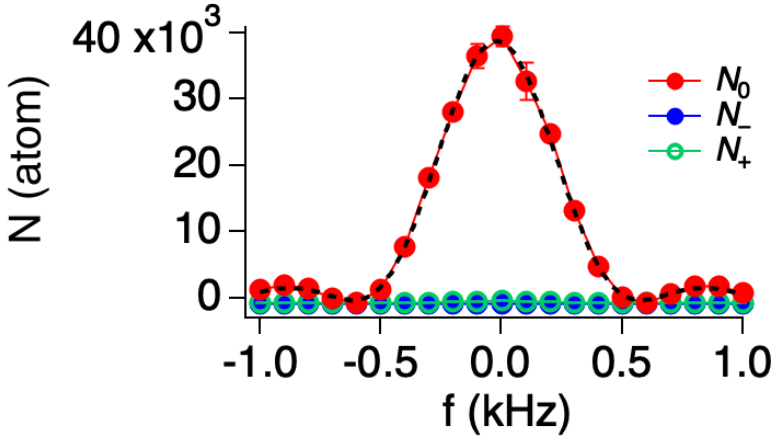

Figure 3.32: Microwave clock transition spectrum. The horizontal axis is the detuning from the clock transition 6.8 GHz plus the quadratic Zeeman shift correction ($q = 72$ Hz/G^2) at B_z =550 mG.

There is a way to verify the spinor phase θ_s shift besides doing the noise measurement. By observing the coherent oscillation (subsection 3.8.8) and measuring the phase shift from the sinusoidal fitting model, the phase difference measured agrees with Equation 3.16, as shown in Figure 3.33.

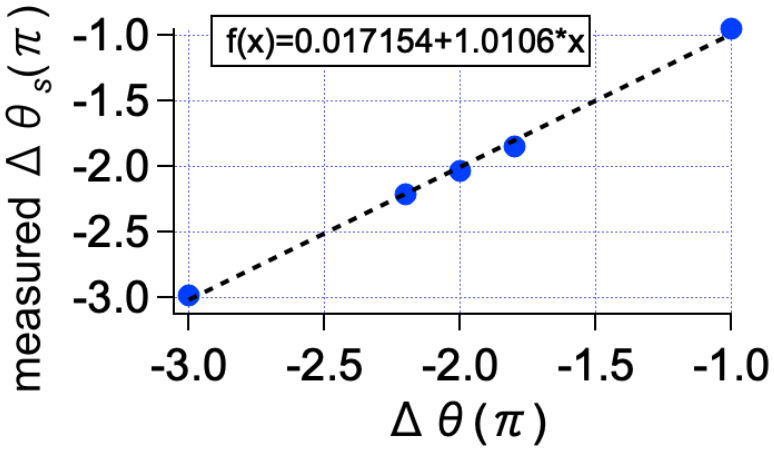

Figure 3.33: The spinor phase shift measured with the coherent oscillation.

As discussed earlier, the magnetic field B can be determined by measuring the frequency difference between the $+\Delta$ transition from $|F = 1, m_F = 0\rangle \leftrightarrow |F = 2, m_F = 1\rangle$, which uses the circularly polarized portion from the microwave.

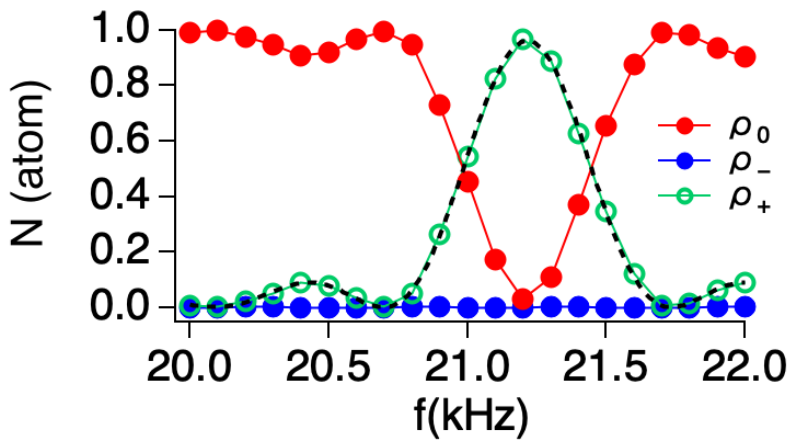

Figure 3.34: Microwave $+\Delta$ transition at B_z =200 mG. The repump laser can be on during the measurement since the SG separates the levels that are involved. The horizontal axis is the detuning from the clock resonance.

3.7 Imaging

The atomic cloud is measured using either fluorescence or absorption imaging techniques. There are three imaging systems that view from the side and the top of the trap. A 1:4 imaging system is used to view from the side and the image is recorded by a surveillance charge-coupled device (CCD) camera (Andor iKon M). This is the major imaging system for the data taken in this thesis due to its high numerical aperture (NA=0.52) with the 26 mm aspheric lens (AL3026-B) inside the chamber. A 3:1 imaging system (iXon) is used to view from the top, which is used to measure the overlap between ODT and dark MOT in the horizontal plane.

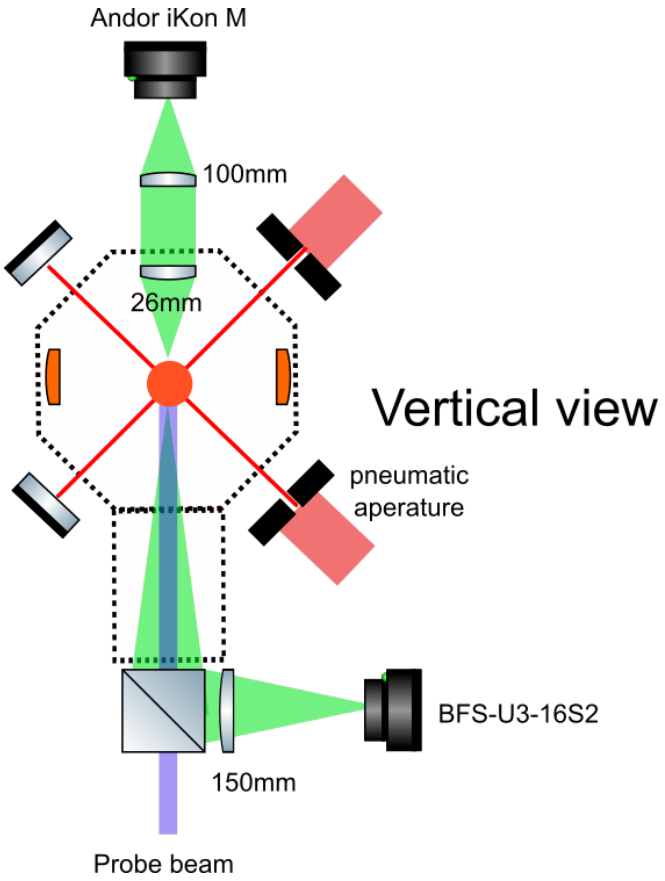

Figure 3.35: The 150 mm lens before the FLIR camera (BFS-U3-16S2) is $2''$ in diameter. The other lens are $1''$ in diameter. For the FLIR camera, $o = 15''$ and $i = 9.73''$.

A 2:1 imaging system (FLIR) is used to view from the side, which is used to constantly monitor the MOT atom number and to measure the overlap between ODT and dark MOT in the vertical plane. For fluorescence probing, we pulse on two near-resonant MOT beams at the maximum power for 200 μs. The average intensity 7.9 mW/cm^2 is above the saturation intensity. To avoid the non-fluorescent light scattering into the imaging path, two pneumatic apertures (see subsection 3.2.3) are added to trim the beam size.

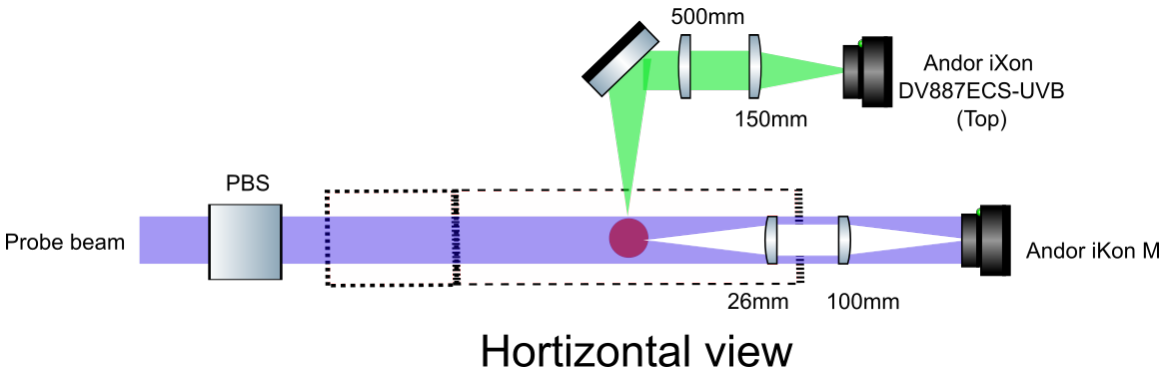

Figure 3.36: The 500 mm lens and 150 mm lens before the iXon camera (Top camera) are $2''$ in diameter.

For absorption imaging, a horizontal and weak probe laser beam is sent through the trapped atoms and directed through the imaging optics to the cooled (-40 °C) CCD camera. This beam is roughly aligned through the center of two view ports and then fine-tuned with micrometers. To image the atoms in the $F = 1$ state, the repump laser is also pulsed during imaging. The $F = 2$ atoms can be imaged by leaving the repump beam off.

Table 3.10: The iKon camera is half blocked for faster electron transfer so the active pixels is only half of the whole frame. There is an extra 780 nm line filter before the iKon camera which provide the extra 77% attenuation to the CPA. The FLIR camera collects half of the light due to the PBS so the CPA has an attenuation of 50%.

	iKon	iKon	iXon	FLIR
Imaging type	absorption	fluorescence	fluorescence	fluorescence
Pixel size (μm^2)	13×13		16×16	3.45×3.45
Active pixels	512×1024		512×512	1440×1080
Magnification	3.8462		0.3	0.65
Quantum efficiency	90%		70%	30%
κ	1		23	1
Ω		0.0676	0.000645	0.0011
$CPA \cdot 200$ μs (counts/atom)	0.025	178.5	0.0748	0.63

The magnification is calculated by $M = i/o$. The counts per atom per time (CPA/τ)

for fluorescence imaging is calculated by the following

$$CPA/\tau = \frac{n_{pix}}{N\tau} = \frac{\gamma_p \Omega \eta}{\kappa},$$

where $\Omega = (D/2)^2/(4f^2)$ is the solid angle divided by 4π, $\gamma_p = \pi \cdot 6.065$ MHz is the saturated on-resonance photon scattering rate for D_2 line [22], η is the quantum efficiency, κ is the electron to camera count conversion rate (1/gain), and τ is the exposure time. The numerical aperture (NA) is connected by $\Omega = (NA)^2/4$.

With a cloud probed absorptively, the number of atoms is given by

$$N = \frac{-A_{pix}}{\sigma_{eg}} \sum_{pix} \ln T_{pix},$$

where A_{pix} is the magnified area of each pixel, $\sigma_{eg} = 2.907 \times 10^{-9}$ cm^2 is the absorption cross section of the $\sigma^{\pm}$-polarized cycling transition [22], and T_{pix} is the transmission profile. The transmission profile is calculated by dividing the image with condensate cloud shadow by the image without the shadow. If we assume the counts from the camera is $-\ln T_{pix}$, then the CPA for absorption imaging is

$$CPA = \frac{\sigma_{eg}}{A_{pix}}.$$

3.8 Experimental sequence

The experimental sequence begins with loading the MOT for 15 s directly from thermal vapor. The magnetic field and gradient are optimized for max atom loading. After loading the MOT, the cooling configuration is changed to achieve sub-Doppler cooling (dark MOT) in order to maximize the transfer of atoms to the optical trap. The repump intensity is lowered and the MOT beam is first detuned by -93 MHz then further detuned by -182 MHz. The MOT coil gradient is turned off during the second detuning. After holding for

40 ms, all the beams are turned off. The dark MOT has the lowest temperature at 0 bais field, so the MOT coils' spatial center is adjusted to match the best location of the dipole trap. A finer adjustment is by changing the trim coil field to maximize the loading into the ODT. The CO_2 laser beam is turned on after the MOT loading.

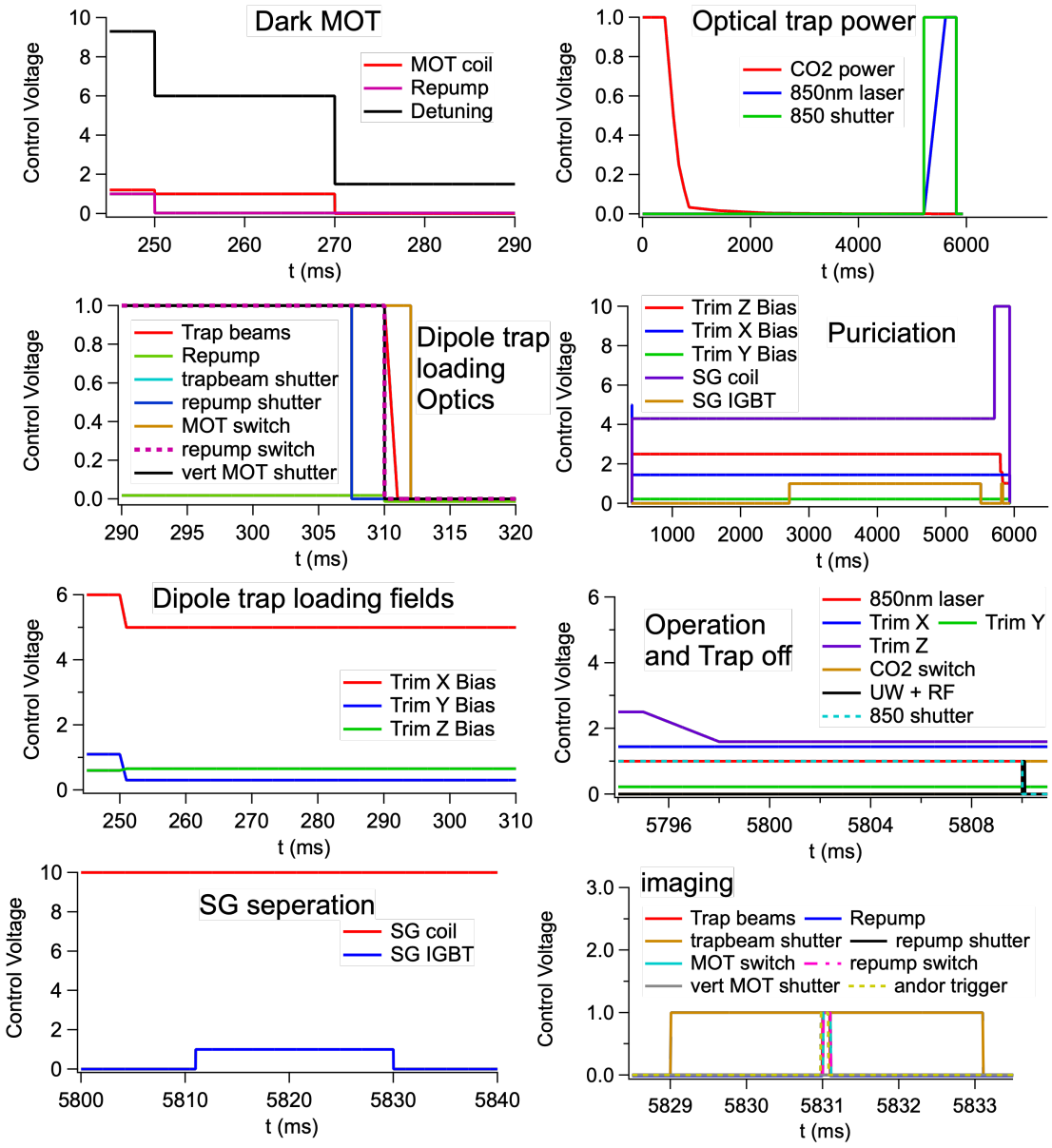

Figure 3.37: Basic experimental sequence.

Now with the ODT loaded, all resonant laser light is extinguished and evaporative cooling begins. Evaporation is accomplished in two ways. Foremost the trap power is simply

lowered adiabatically allowing the hotter atoms to escape. At the same time, the geometry of the trap is changed to maintain the radial trap frequency and re-thermalization rate (section 3.4). During evaporation, we typically apply magnetic bias and gradient to create a $m_F = 0$ condensate. This pulls the $m_F = \pm 1$ towards more weakly trapped regions causing them to be lost preferentially. After the gradient is ramped down, the 850 nm laser is ramped up to confine the condensate satisfying the single-mode approximation. For the typical experiment, we prepare a condensate of $N = 5 \times 10^4$ atoms in a cross optical dipole trap and in a $B_0 = 1.1$ G magnetic bias field. After the dynamical evolution of the spin states, the microwaves and RF pulses are used to rotate the state for measurement purposes. At this point, all trapping lasers are shut off and the atoms are allowed to fall and expand for 5-20 ms. During this time of flight (TOF) a magnetic gradient is turned on again to spatially separate the final m_F projections. At the end of this expansion, beams are turned on for the imaging (section 3.7).

Steps of checking BEC

1. Check the MOT atom number.
2. Check the slave cycling laser is following the master during the dark MOT detuning.
3. Scan the repump power during dark MOT.
4. Check the overlap between ODT and dark MOT.

3.8.1 Time of flight measurement

The time of flight (TOF) for MOT, dark MOT, dipole trap loading are measured with the top camera and the FLIR camera.

Table 3.11: Atom number and temperature measurement for each experimental stage.

	MOT	Dark MOT	Dipole trap loading
Atom number (10^6)	15	12	4
Temperature (μK)	74	18	
Density (10^9/cm^3)	5	4	

The temperature of the thermal atoms can be determined by measuring the momentum distribution of the cloud. When a cloud is released from the trap, the momentum distribution of the atoms will be converted to a spatial density distribution. By collapsing a cloud image to a 1D profile as shown in Figure 3.38, the Gaussian waist σ can be found with a fitting. With the measured Gaussian waist, the temperature can be readily found as

$$T = \frac{m}{k_B}(\frac{\sigma}{t})^2.$$

In addition, one can also measure the cloud size for various drop times, and then fit the cloud expansion rate with a quadratic equation: $\sigma^2 = \sigma_0^2 + \frac{k_B T}{m} t^2$ [40].

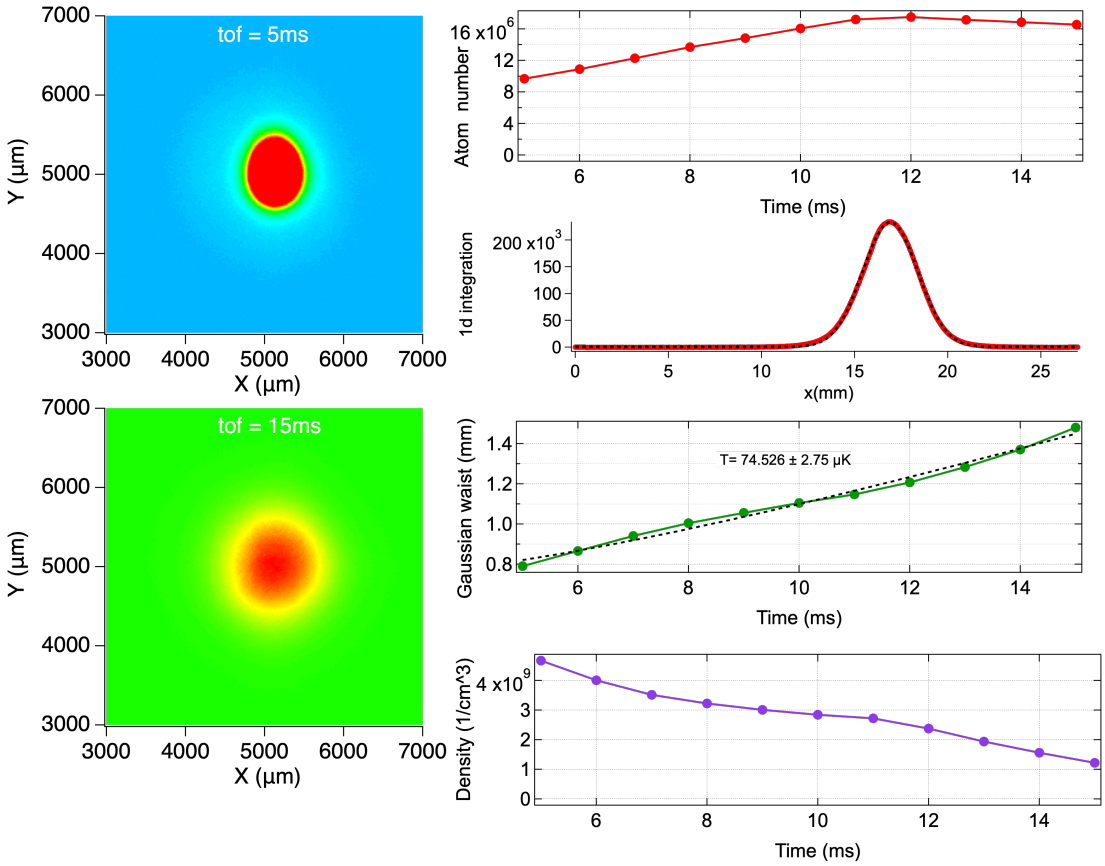

Figure 3.38: TOF measurement for MOT. The temperature is measured by fitting to the 1D Gaussian waist for different drop time.

The dipole trap loading is measured with both the top camera and the FLIR camera. The atom number is measured with a long enough TOF (50 ms) to release all the atoms from dark MOT that are not trapped. The location of the dipole trap in three-dimension can be easily overlapped with dark MOT using images from two orthogonal directions.

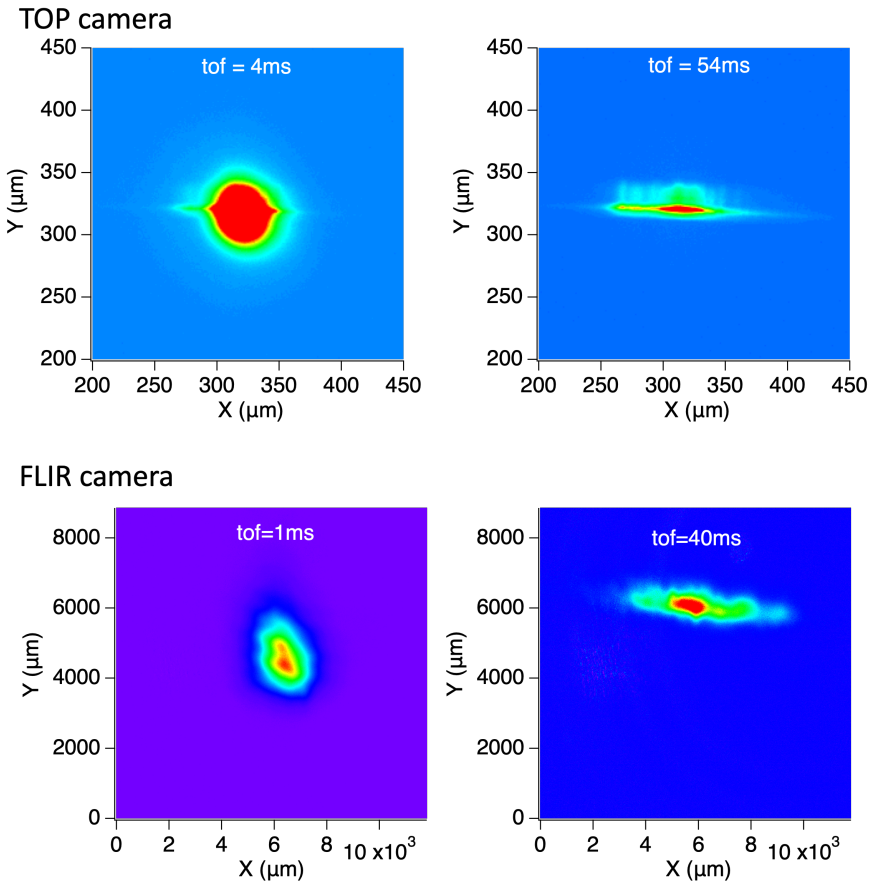

Figure 3.39: Dark MOT and ODT overlap measured with the top and FLIR camera.

3.8.2 BEC temperature and condensate fraction

When the temperature is very close to the critical temperature of a quantum phase transition, the properties of a cloud will deviate from that of a classical gas, and the treatments in the last subsection based on Boltzmann statistics are insufficient. In this temperature regime, image analysis based on Bose statistics is necessary. For $T < T_c$, the cloud has both a thermal gas and condensate component. As a result, we fit the absorption image with bimodal formula

$$n = Ag_2(e^{-\frac{x^2+y^2}{2\sigma^2}}) + B\max(1 - \frac{x^2}{R_x^2} - \frac{y^2}{R_y^2}, 0)^{3/2},$$

where A, σ, B, $R_{x,y}$ are free fitting parameters [40].

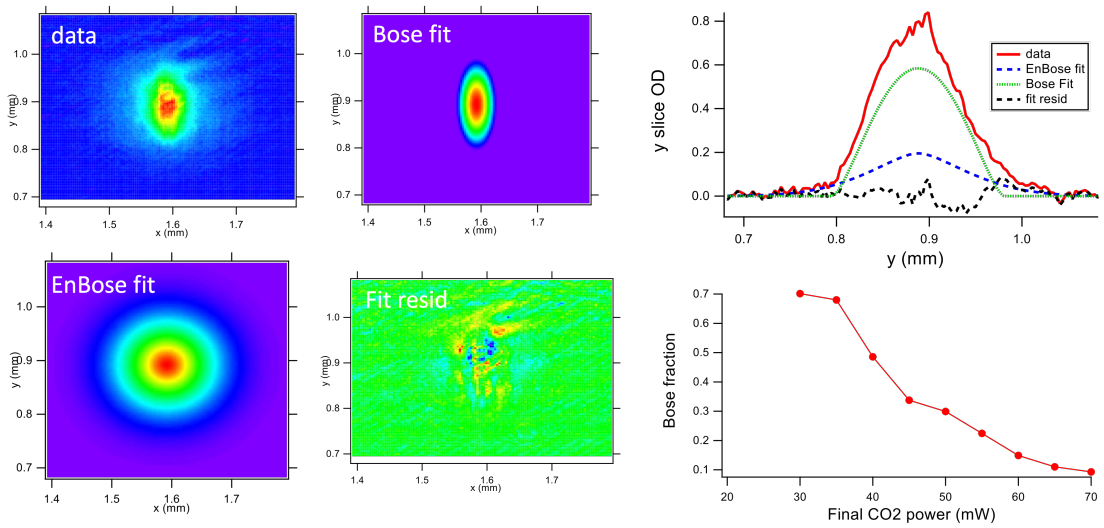

Figure 3.40: Bimodal fit to condensates. The Bose part gives the count of condensate fraction while the enBose part gives the thermal fraction. The condensate fraction is higher at lower CO_2 power.

3.8.3 RF calibration

The atom detection is calibrated using a coherent RF $\pi/2$ rotation to measure the standard quantum limit (SQL) [10]. The calibration is performed at the same final magnetic field as the squeezing measurements 4 ms after a fast quench to minimize spin evolution [11]. The quantum projection noise $\sigma^2_{QPN} = \Delta M^2 - \sigma^2_{PSN} - \sigma^2_{bkg}$ is extracted by subtracting the photon shot noise σ^2_{PSN} and the background imaging noise σ^2_{bkg} from the measured magnetization variance ΔM^2 [10]. The uncertainty of σ^2_{QPN} is given by $\text{std}(\sigma^2_{QPN}) = \sigma^2_{QPN}\sqrt{\frac{2}{N_s-1}}$, where N_s is the number of measurements. The photon shot noise $\sigma^2_{PSN} = N_e = N/(CPA/4)$, where N_e is the number of electrons. The extra factor of 4 comes from the super-pixels by combing the electrons of multiple (adjacent) pixels into a large bin [41]. A 4 by 4 binning is used in the fluorescence imaging readout which means the readout noise will be reduced by a factor of $\sqrt{16} = 4$ at the expense of the spatial information provided by the separate 16 pixels.

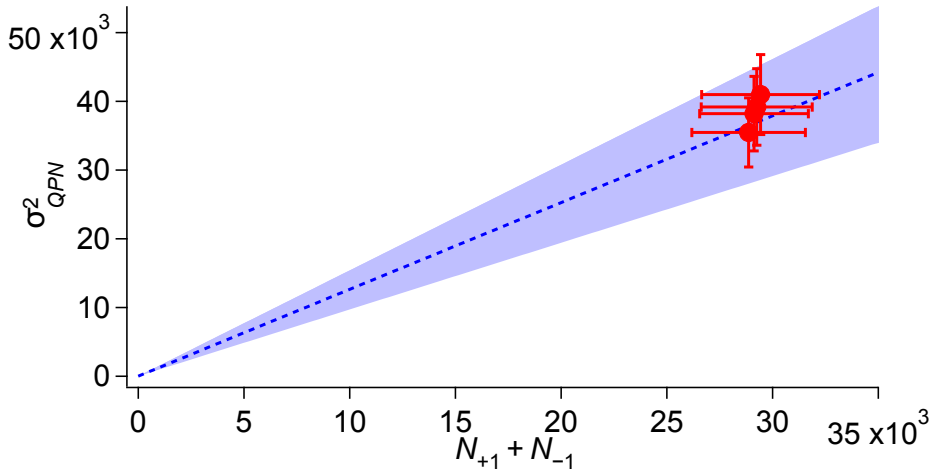

Figure 3.41: The atom detection is calibrated to measure the SQL. The calibration is performed $t = 4$ ms after a fast quench to minimize spin evolution at the same final magnetic field. Theoretical prediction gives 0.87 dB (± 1 dB) anti-squeezing. The count per atom with 200 µs exposure time is 157.9 counts/atom which is close to the estimated value in section 3.7.

3.8.4 Spin mixing

When $q < 2|c|$, the system starts to show the spin mixing phenomenon [8]. The measurement is performed after a fast quench to the magnetic field below the critical point. The mean value of ρ_0 population shows the dynamical evolution suggest correlated pairs of atoms in $m_F = \pm 1$ are generated due to the dominance of spin-spin collision energy. The behavior can be understood from the energy contour given by Equation 2.31.

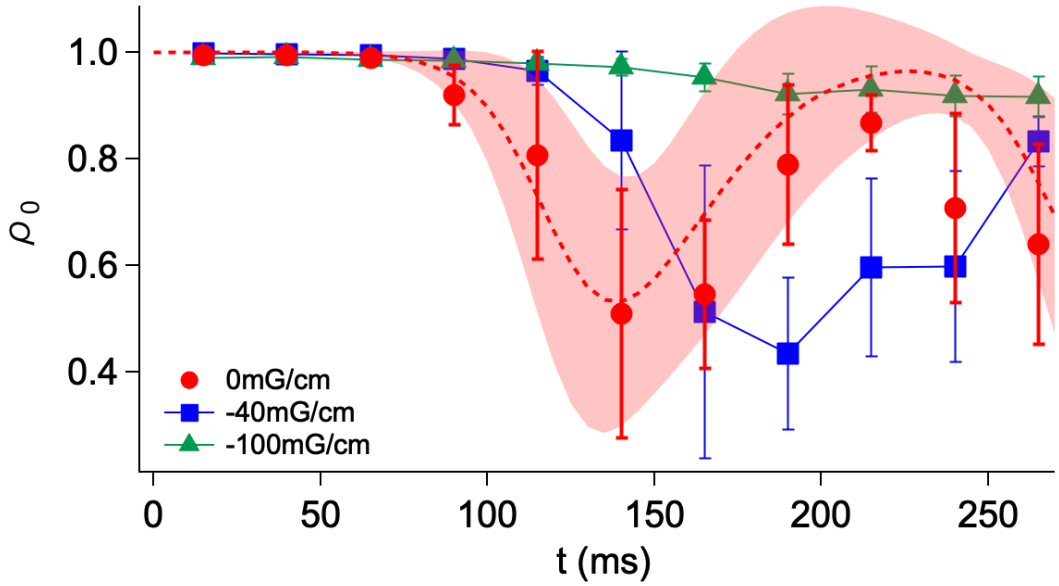

Figure 3.42: Spin dynamical evolution (spin-mixing) at $B_z = 250$ mG, 10 shots for each point. Correlated pairs of $m_F = \pm 1$ are generated, similar to the optical four-wave mixing. The data agree with the mean-field simulation prediction only with a precisely canceled $\partial B_z/\partial z$ (red circles).

3.8.5 Number squeezing

Spin-mixing in Figure 3.42 generates correlated pairs of atoms in $m_F = \pm 1$ that exhibit number squeezing in the magnetization $M = N_{+1} - N_{-1}$, similar to optical four-wave mixing. The fluctuations in magnetization at the same dynamic evolution time (t=165 ms) shows sub-Poissonian fluctuations. We therefore repeat the experiment 1000 times and acquire data sets for different degrees of spin mixing [41]. In Figure 3.43, M is plotted versus the number of atoms $N_{\pm} = N_{+1} + N_{-1}$. To quantify how much the magnetic fluctuations are suppressed in comparison with a Poissonian distribution, we define a number squeezing parameter $\xi^2_{S_z} = (\Delta M)^2/N_{\pm}$ (see Figure 3.43). With the detection noise corrected, we see a suppression of the magnetic fluctuations by up to -7 dB which sets up the detection limit [10].

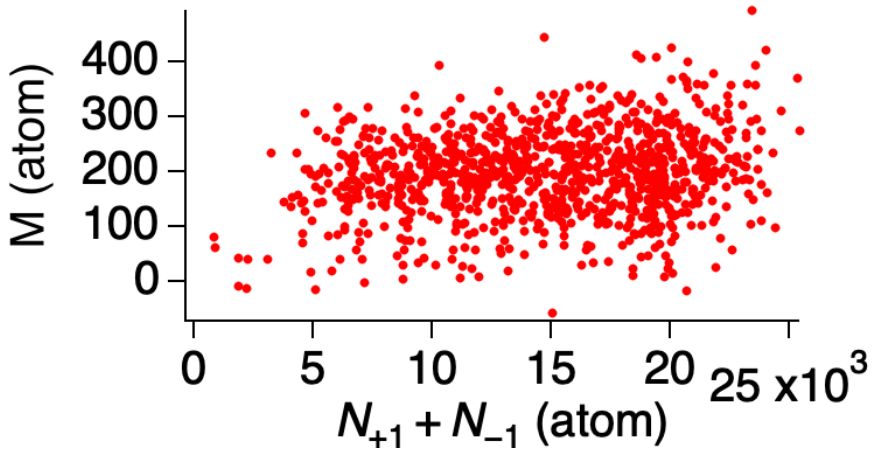

Figure 3.43: The experiment is repeated 1000 times at 165 ms after the rapid quench, which is the lowest ρ_0 point during the dynamic evolution. This data is then binned into bins with a width of $\Delta N_{\pm} = 2000$ atoms such that each data set contains a sufficiently large number of data points (around 100) to determine the fluctuations of the magnetization. There is a slight imbalance in the counting of N_+ and N_- atoms, which comes from the small beam used in imaging does not shine the light evenly on the clouds. To solve that, the aperture masks (see section 3.7) are fine-tuned using micrometers to carefully maximize the counting while minimizing the imbalance.

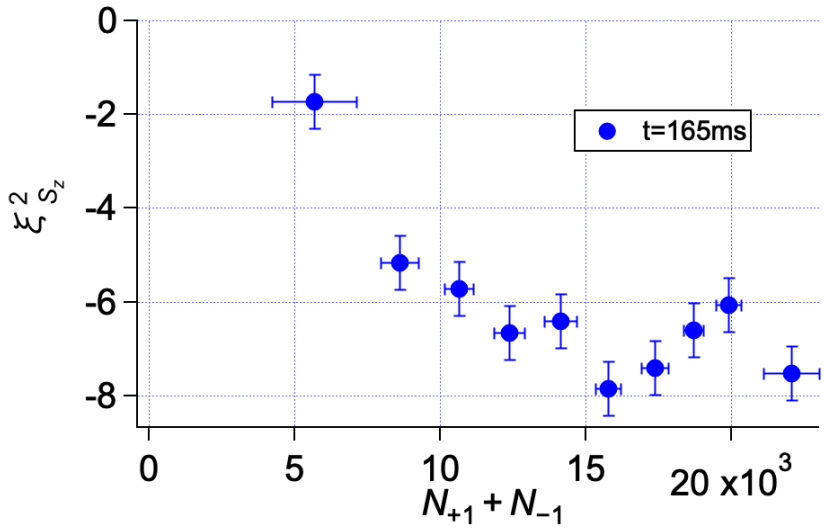

Figure 3.44: To highlight the difference between fluctuations of magnetization generated through spin-mixing compared to those of a Poissonian distribution, we contrast the data with a coherent spin state generated through an RF rotation.

3.8.6 Critical B_z field scan

The collisional spin interaction energy c is determined by careful measurement of the QCP using a quenching technique [14]. Quenching the condensate to fields close to the QCP and measuring the relative spin populations following 165 ms of evolution at the final field, it is possible to determine q_c with a precision of ± 0.1 Hz (see Figure 3.45). For the experiments, c ranged from $[-7.5, -8.7]$ Hz due to day-to-day variations of the experimental conditions. The critical point measurement is very important in the quantum Kibble-Zurek mechanism study [14] and also the squeezed ground state study in this thesis.

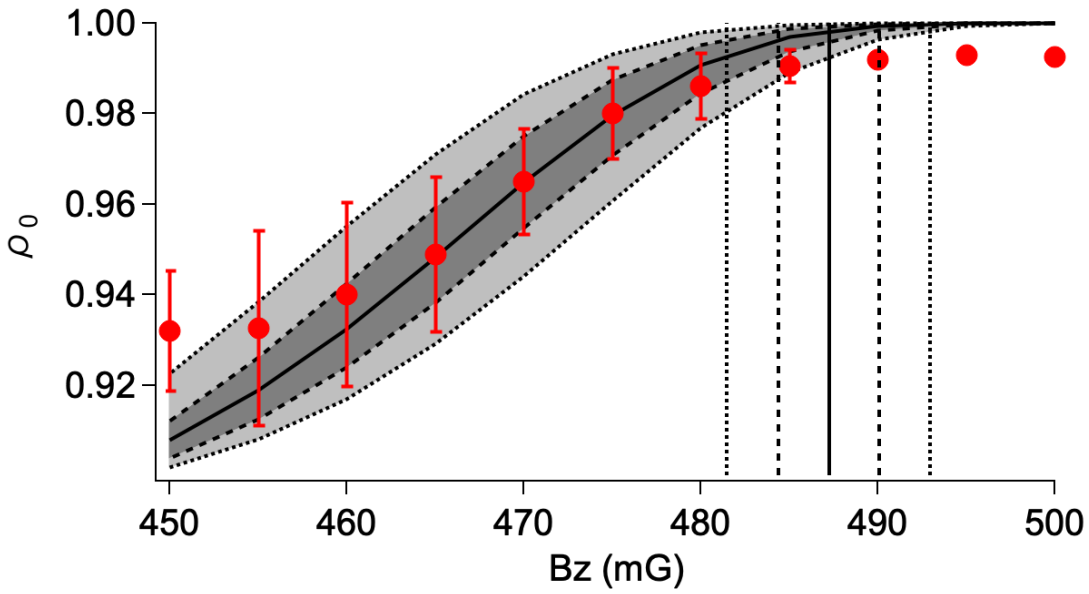

Figure 3.45: The critical point detection uses a sudden quench to B_z at $t = 165$ ms. ρ_0 is measured as a function of B_z. 1% pollution from $\lambda = 850$ nm laser is presented compared to the simulation result as discussed in Figure 5.8. The black solid line $c = -8.5$ Hz, dashed lines ± 0.1 Hz, and dotted lines ± 0.2 Hz are attached to the figure. By using the simulation, c can be decided with precision about ± 0.1 Hz.

3.8.7 Lifetime measurement

By holding the condensate inside the trap at a high magnetic field and measuring the atom number decay, the lifetime of the condensate can be detected. The lifetime τ has a very close relationship related to the vacuum and the density of the cloud. For typical measure-

ment in the single focus trap, $\tau = 4$ to 5 s, and in the cross trap $\tau = 2$ to 3 s. Figure 3.46 shows a typical measurement inside the cross trap along with c measured using the method in subsection 3.8.6. This verifies the relationship $c \propto N^{2/5}$.

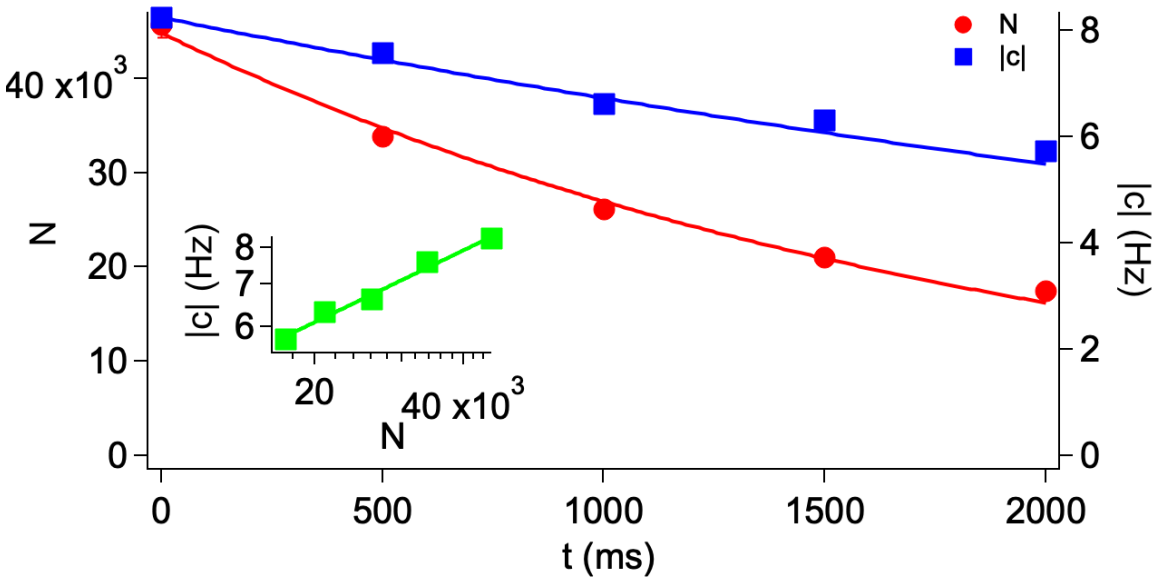

Figure 3.46: Different atom number N generated by a finite lifetime decay of BECs versus c is studied using the method in subsection 3.8.6. The measured $|c|$ agrees well with the analytic relationship $c \propto N^{2/5}$ (inset green line).

3.8.8 Coherent oscillation [9]

To investigate the coherent dynamics of the system, an initial coherent spin state superposition is created from the pure $m_F = 0$ condensates by applying an RF pulse. Following the pulse sequence, the magnetic field is ramped to either above or below the critical point and the condensate is allowed to freely evolve in the optical trap. The oscillation of the dynamics below the critical point has a bigger amplitude. A typical evolution is shown in Figure 3.47 with different initially prepared states. These oscillations demonstrate the coherence of the spin mixing process.

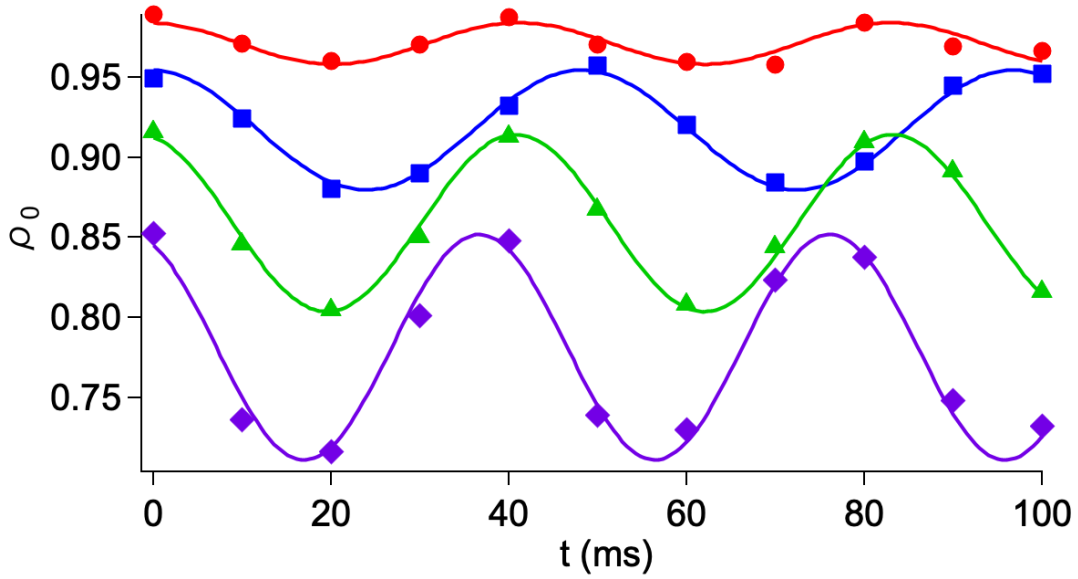

Figure 3.47: Coherent spin mixing vs. initial state. Multiple initial non-equilibrium spin populations are created and allowed to evolve in the same field above the critical point. Subsequently, the system displays small amplitude oscillations due to the coherent spin mixing. A larger initial rotation angle indicates faster oscillation frequency and larger amplitude.

3.8.9 Spin-nematic squeezing [11]

During spin-mixing, spin-nematic squeezing develops. The fluctuations of the measured magnetization and how they vary with spinor phase shift is the signal of spin-nematic squeezing. The noise tomography is performed by first shifting the spinor phase with a detuned microwave π pulse (see section 3.6) and then a $\pi/2$ RF pulse. For each combination of evolution time and phase shift, the experiment cycle is repeated 100 times to collect statistics of measured magnetization. The measurement is limited by the detection which is a combination of light scattered by the apparatus and the photo-electron shot noise. This limit (gray area in Figure 3.48) is detected in subsection 3.8.5.

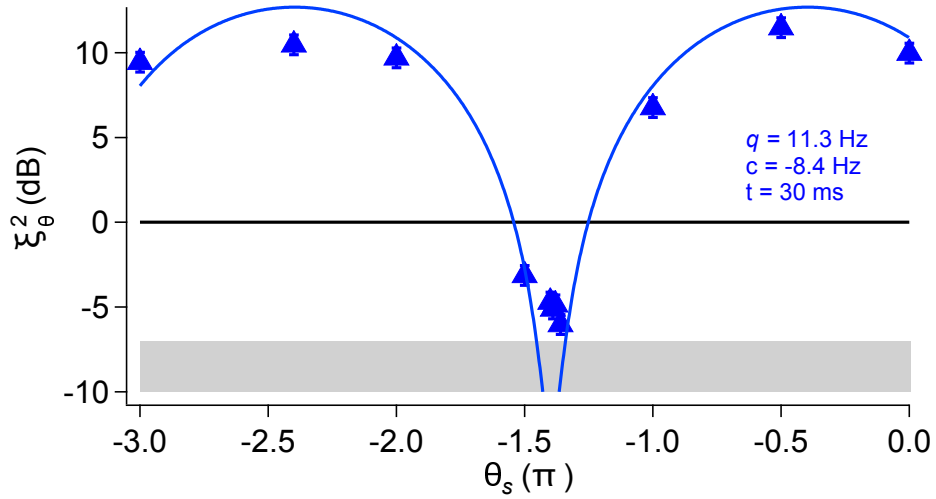

Figure 3.48: Spin-noise tomography measurement for the deep quench method at $B_z = 400$ mG, $t = 30$ ms. The simulations (blue solid line) match well without any adjustments. The maximum squeezing does not have a fixed $\theta_{s,min}$ because it is an asymptotic function of parameters $q/|c|$ and t.

Steps of checking spinor dynamics

1. Check the Aux coil to make sure the gradient is properly zeroed.

2. Check the imbalance between the ± 1 atoms and optimize it by adjusting masks' position.

3. Check the absorption image of the cross trap and single focus trap, make sure the 850 nm laser is well overlapped with the condensate.

4. Measure the critical B_z to make sure c is around -7 to -8 Hz.

5. Check the spreadsheet by using Igor Pro visualization, make sure all control sequences are logically correct.

CHAPTER 4
SQUEEZED GROUND STATE THEORY

4.1 Introduction

Creation and characterization of quantum squeezed and entangled states in atomic Bose-Einstein condensates (BECs) with internal spin degrees of freedom are frontier problems in the field of quantum-enhanced measurement and in the investigations of quantum phase transitions and non-equilibrium many-body dynamics [42, 43]. Condensates with ferromagnetic spin-dependent collisional interactions exhibit a second-order quantum phase transition, which is tunable by using external fields and available to low-noise tomographic quantum state measurement. Experimental studies of collisionally-induced spin squeezing in condensates have mainly utilized time evolution following a magnetic field quench from an initially uncorrelated state to below the quantum critical point (QCP). The squeezing is a result of the quenching and subsequent dynamics generated by the the final Hamiltonian, which is either of the one-axis twisting form [44, 45] or a close variant [11, 46]. Spin squeezed states have also been generated without quenching through the QCP by parametric/Floquet excitation [12, 47].

In addition to these inherently non-equilibrium methods, there is much interest in utilizing adiabatic evolution in spin condensates to create non-trivially entangled ground states such as Dicke states and twin-Fock states [48]. Towards this end, there have been experiments using adiabatic [13] or quasi-adiabatic [49, 30] evolution across the symmetry breaking phase transition to create these exotic entangled states. Although some of the interest in these methods has been stimulated by potential applications to adiabatic quantum computing, there are also compelling applications to quantum enhanced metrology [50]. A key feature of these approaches is that the entanglement is created in the time-stationary

states of the final Hamiltonian, at least in the limit of perfect adiabaticity.

Here, we focus on Gaussian spin squeezed states and consider methods to create time-stationary spin squeezing in a spin-1 condensate by tuning the system Hamiltonian through a pair of quenches of the external magnetic field. Similar squeezed states have previously been discussed in the context of spin-$1/2$ systems [51, 52, 53, 54]. Our protocol effectively shortcuts the adiabatic technique [55], overcoming the challenge of maintaining adiabaticity in the neighborhood of the QCP where the frequency scale of the final Hamiltonian evolution tends to zero. Although we focus our attention on spin-1 condensates because of our experimental work, the protocol in our paper is general and can be applied to the spin-$1/2$ systems [45, 56] as detailed in section 4.7. As the squeezing is time-stationary it may be observed directly without the need for balanced homodyne [57] nor Fock states population detection methods [58].

Effectively we propose to implement the quantum harmonic oscillator symplectic Heisenberg picture dynamics $(X, P) \mapsto M(t)(X, P)$, for times t greater than the squeezed state preparation time T, where

$$M(t) = \begin{pmatrix} -x_f \sin \omega_f (t-T) & x_f \cos \omega_f (t-T) \\ -x_f^{-1} \cos \omega_f (t-T) & -x_f^{-1} \sin \omega_f (t-T) \end{pmatrix},$$

satisfies $\det M(t) = 1$, and (X, P) is regarded as a column vector of initial Heisenberg/Schrödinger picture operators [1]. Here ω_f is the oscillator final frequency, i.e., at the end of the protocol, while x_f is the final oscillator dimensionless length scale, defined below. The Heisenberg-limited squeezing of position and momentum variables, associated with the reciprocal factors in the rows of matrix $M(t)$, is independent of time for $t > T$ under this dynamics. Our shortcut protocol requires a preparation time $T \sim \sqrt{\eta}$ which is $\sqrt{\eta}$ faster than the lower limit of the adiabatic passage $T_{ad} \sim \eta$. Here $1/\eta$ is the degree of squeezing of the position or momentum variance. The method solves the problem

[1] Or as classical Hamiltonian phase space coordinates

connecting the time evolution between two quantum oscillator ground states, and its simplicity renders optimal control considerations somewhat superfluous (section 4.6). We note that optimal control between canonical thermal states of collections of oscillators has been extensively investigated [59, 60, 61].

In this section, we consider the dynamics of a spin-1 condensate in a magnetic field oriented along the z direction and satisfying the single spatial mode approximation to be described by the Hamiltonian [11],

$$\hat{H} = \frac{c}{2N}\hat{S}^2 - \frac{q}{2}\hat{Q}_z, \tag{4.1}$$

The operator $\hat{Q}_z = -\hat{N}/3 - \hat{Q}_{zz}$ is defined in terms of the nematic (quadrupole) tensor. The classical phase space corresponds to intersecting unit spheres in the $\{S_x, Q_{yz}, Q_z\}$ and $\{S_y, Q_{xz}, Q_z\}$ variables.

The classical phase-space orbits of constant energy per particle are shown in Figure 4.1. For $q \gg 2|c|$, the ground state of the Hamiltonian is the polar state with all atoms having $S_z = 0$, and which in the Fock basis can be written as $|N_{+1}, N_0, N_{-1}\rangle = |0, N, 0\rangle$, where N_i labels the occupancy of the corresponding Zeeman state, $i = -1, 0, 1$. The polar state gives a symmetric phase space distribution in $\{S_x, Q_{yz}\}$ and $\{S_y, Q_{xz}\}$ as shown in Figure 4.1(a) [12]. This state is the starting point for many experiments in part because it is easily initialized and stationary in the high q limit. In previous experimental work [11], we have been able to generate a large degree of squeezing by suddenly quenching the magnetic field from $q = \infty$ into the interval $q \in (0, 2|c|)$, such that the initial state evolves along the separatix developed in the phase space shown in Figure 4.1(b). The time evolution stretches the noise distribution along the separatrix and leads to a large degree of squeezing $\xi^2_{min} < 1$ for short enough times, as shown in Figure 4.1(c).

In this section, we propose a method to create time-stationary minimum uncertainty squeezed states of a spin-1 condensate. The squeezing is a response to the deformation of

the phase space as the system Hamiltonian is tuned close to the QCP. We consider principally the low-energy polar state ($\langle \hat{Q}_z \rangle = 1$), whose phase space is shown in Figure 4.2(a). We also discuss the experimentally less accessible high-energy polar state ($\langle \hat{Q}_z \rangle = -1$) whose phase space is shown in Figure 4.2(b). In both cases, Gaussian fluctuations can be treated by means of quantum harmonic oscillator dynamics in the limit of large particle number.

The remainder of the paper is organized as follows. In section 4.2 we discuss the protocol in the quantum harmonic approximation, proving that time-stationary spin squeezed states are produced by presenting complementary arguments in the Heisenberg and Schrödinger pictures. In subsection 4.2.2 we consider the validity of the harmonic approximation as a function of system size N, by means of numerical solutions of the full dynamics. In subsection 4.2.3 we show how the harmonic approximation provides a practical method to estimate the fidelity of state preparation in the experimentally relevant limit of large system size. In section 4.3 we present our conclusions discussing the calculation of finite system-size energy gaps, the residual noise fluctuations, squeezing in the high energy polar state, and a brief comparison with the optimal control protocol for our problem.

4.2 Time-stationary squeezing: controlled double quench

We consider the condensate to be prepared in the low-energy polar state in the limit of large magnetic field $q \to \infty$. (Essential changes in the analysis needed to describe the high-energy polar state are outlined in section 4.5.) A pair of quenches of the external magnetic field is used to bring the system towards the critical point, where squeezing develops. The procedure thereby avoids the critical slowing down experienced by adiabatic methods [14].

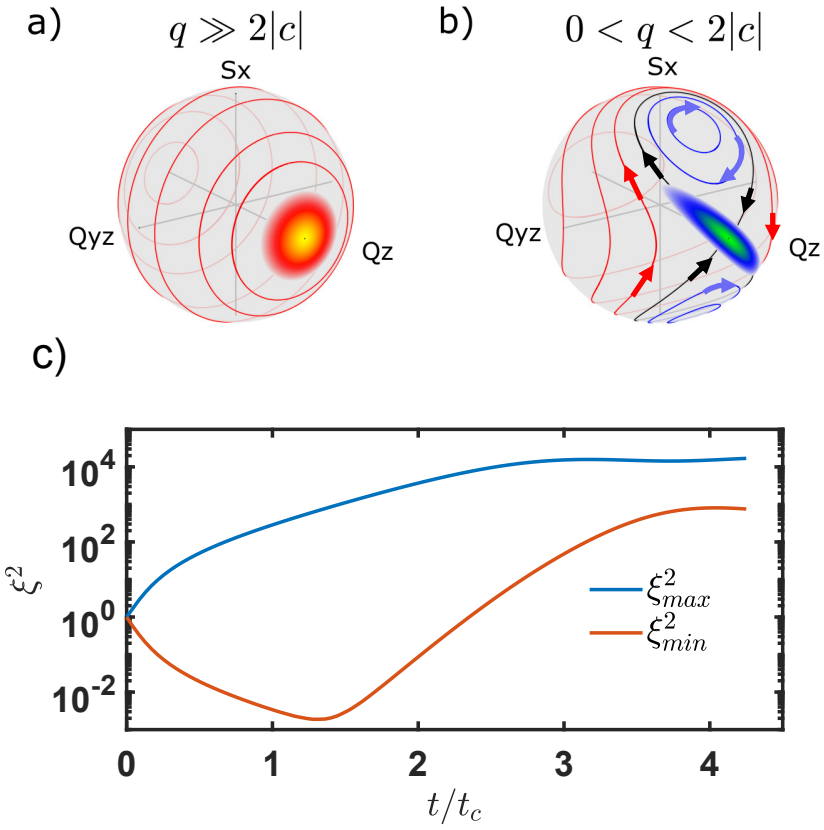

Figure 4.1: Standard method of creating (non-stationary) squeezed states in a spin-1 BEC. The phase spaces for (a) $q \gg 2|c|$, (b) $0 < q < 2|c|$, respectively. Red/blue lines indicates the energy higher/lower than the separatrix (black lines) across $(\langle \hat{S}_x \rangle, \langle \hat{Q}_z \rangle, \langle \hat{Q}_{yz} \rangle)$=(0,$N$,0) point. The red distribution is an exaggerated illustration of the polar state. The blue distribution is the non-equilibrium evolution for the state initially prepared in (a), which stretches along the seperatrix as observed in our previous work [11]. (c) The evolution of the maximum ξ^2_{max} and the minimum squeezing parameter ξ^2_{min} as a function of dimensionless time t/t_c. The squeezing is lost after a few characteristic times $t_c = 2\pi\hbar/|c|$.

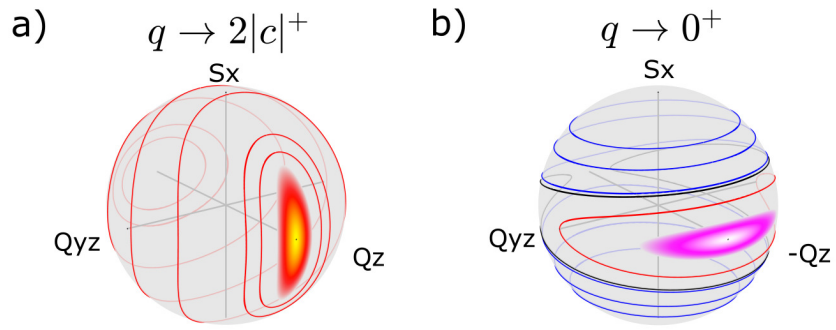

Figure 4.2: Squeezing in the low and high energy polar states. The phase spaces are shown for the low-energy polar state in (a) as $q \to 2|c|^+$ (a one-sided limit from above) and in the high-energy polar state in (b) as $q \to 0^+$. As q approaches the QCP, the states follow the deformation of the constant-energy level sets and squeeze accordingly.

4.2.1 Harmonic approximation: $N \to \infty$

In Figure 4.2(a) near the pole at $\langle \hat{Q}_z \rangle = 1$, Equation 4.1 can be approximated by

$$H = \frac{2c+q}{4} \frac{\hat{S}_x^2 + \hat{S}_y^2}{N} + \frac{q}{4} \frac{\hat{Q}_{yz}^2 + \hat{Q}_{xz}^2}{N} + O(\hat{S}_\mu^4, \hat{Q}_{\mu\nu}^4) \tag{4.2}$$

when $q > 2|c|$. We see from Equation 4.2 that the orbits near the polar axis are harmonic oscillator-like to leading order. The starting point for a quantum harmonic description of the noise fluctuations is the identification of canonically conjugate variables, in the $\hat{S}_z = 0$ subspace formed by $|N_1, N_0, N_{-1}\rangle = |k, N-2k, k\rangle =: |k\rangle$, $0 \le k \le \frac{N}{2}$.

The commutation relations for the subspace are $\langle k'|[\hat{S}_x, \hat{Q}_{yz}]|k\rangle = i(6k-2N)\delta_{k',k}$ and $\langle k'|[\hat{S}_y, \hat{Q}_{xz}]|k\rangle = i(2N-6k)\delta_{k',k}$. Near the $\hat{Q}_z$ pole where $k \ll N$, the commutation relationships are $\langle k|[-\hat{S}_x/\sqrt{2N}, \hat{Q}_{yz}/\sqrt{2N}]|k\rangle = i + O(k/N)$ and $\langle k|[\hat{S}_y/\sqrt{2N}, \hat{Q}_{xz}/\sqrt{2N}]|k\rangle = i + O(k/N)$. Hence

$$X_1 := -\hat{S}_x/\sqrt{2N}, \quad X_2 := \hat{S}_y/\sqrt{2N},$$
$$P_1 := \hat{Q}_{yz}/\sqrt{2N}, \quad P_2 := \hat{Q}_{xz}/\sqrt{2N},$$

also satisfy $[X_1, X_2] = [P_1, P_2] = -i\hat{S}_z/(2N) = 0, [X_1, P_2] = [X_2, P_1] = i\hat{Q}_{xy}/(2N) = 0$ by neglecting terms of $O(k/N)$ and are thus canonically conjugate variables analogous to a pair of position and momenta. The predictions of the harmonic approximation will be compared with numerical calculations of the full dynamics in subsection 4.2.2.

The system is accordingly described by two identical uncoupled quantum oscillators with Hamiltonian

$$H = \frac{2c+q}{2}(X_1^2 + X_2^2) + \frac{q}{2}(P_1^2 + P_2^2),$$

with $[X_\alpha, P_\beta] = i\delta_{\alpha,\beta}$. We can identify the effective mass $m = q^{-1}$ and frequency $\omega = \sqrt{q(q-2|c|)}$. As the oscillators are identical and the initial conditions uncorrelated, we treat a generic oscillator in the following discussion and omit the identifying subscript for notational simplicity.

The dimensionless length scale $\sqrt{q/\omega}$ of the oscillator is reciprocal to its momentum scale. The initial condition for the low-energy polar state of the spinor condensate corresponds to the oscillator prepared in its ground state, in which the oscillator position and momentum scales are both equal to unity, $q/|c| >> 1$. In this case the quantum fluctuations are Heisenberg limited and equally shared between position and momentum variables, corresponding to a coherent vacuum state. Regarding the quadratic Zeeman energy q as an external control variable, the target squeezed state is the ground state of a deformed oscillator in which the dimensionless length $x_f = \sqrt{q_f/\omega_f}$ and momentum x_f^{-1} scales are vastly different. This can be achieved by adjusting q to a final value q_f near to the QCP ($q_c := 2|c|$), where $\omega_f = \sqrt{q_f(q_f - 2|c|)} \to 0$ and x_f diverges. In the following we propose a procedure which implements the symplectic Heisenberg picture dynamics $(X, P) \mapsto M(t)(X, P)$, for times t greater than the squeezed state preparation time T, where

$$M(t) = \begin{pmatrix} -x_f \sin\omega_f(t-T) & x_f \cos\omega_f(t-T) \\ -x_f^{-1}\cos\omega_f(t-T) & -x_f^{-1}\sin\omega_f(t-T) \end{pmatrix} \tag{4.3}$$

satisfies $\det M(t) = 1$, and (X, P) is regarded as a column vector of Heisenberg picture

operators corresponding to the initially prepared low-energy polar state. As shown in the following subsection the Heisenberg-limited squeezing of position and momentum variables, associated with the reciprocal factors in the rows of matrix $M(t)$, is independent of time for $t > T$ under this dynamics.

Heisenberg picture

The squeezing protocol may be analyzed in the Heisenberg picture as follows. We wish to reduce the Zeeman energy q from large positive values towards $2|c|$, and in order to do this we consider a preparation time T which is bounded at its ends $t = 0$ and $t = T$ by a pair of instantaneous quenches in which q is successively reduced through piecewise constant values in the intervals $t < 0$, $0 \leq t < T$ and $T \leq t$. We will refer to these regimes as the (low-energy) polar condensate regime, the intermediate regime and the final regime, respectively, and label the oscillator parameters appropriately. The initial value of $q = 10^3|c|$, is used to represent the dominance of the quadratic Zeeman energy in the prepared polar condensate $q/|c| \to \infty$. The complete time dependence is given by

$$q(t) = 10^3|c|\chi_{(-\infty,0)}(t) + q_i\chi_{[0,T)}(t) + q_f\chi_{[T,\infty)}(t),$$

where the indicator function for a set A is defined by $\chi_A(t) = 1$ for $t \in A$ and $\chi_A(t) = 0$ for $t \notin A$, and q_i is yet to be determined. We will choose T to be a quarter of the oscillation period of the intermediate oscillator, as in previous discussions of harmonic oscillator squeezing by instantaneous change of frequency [62, 63, 64].

Just prior to the first quench at $t = 0$, the initial Heisenberg picture position and momentum operators are written as (X, P). During the first quench the Heisenberg position and momentum operators are continuous [65, 66], and with $\omega_i = \sqrt{q_i(q_i - 2|c|)}$, the length scale of the intermediate oscillator is $x_i := \sqrt{q_i/\omega_i}$. For $0 \leq t < T$, the time evolution of

the Heisenberg operators is then

$$X(t) = X\cos\omega_i t + x_i^2 P\sin\omega_i t$$
$$P(t) = P\cos\omega_i t - x_i^{-2} X\sin\omega_i t.$$

Choosing T to correspond to a quarter period of oscillation $\omega_i T = \pi/2$, gives

$$X(T) = x_i^2 P \text{ and } P(T) = -X/x_i^2.$$

This single sudden quench results in a time-periodic oscillation of position/momentum squeezing as observed previously [63, 67].

In the second quench at $t = T$, q is reduced from q_i to a value q_f closer to $2|c|$, and the operators $(X(T), P(T))$ are continuous. For $\tau := t - T \geq 0$, the subsequent harmonic motion is at the slow frequency $\omega_f = \sqrt{q_f(q_f - 2|c|)}$, and

$$X(t) = x_f\left[(x_i^2/x_f)P\cos\omega_f\tau - (x_f/x_i^2)X\sin\omega_f\tau\right]$$
$$P(t) = -x_f^{-1}\left[(x_f/x_i^2)X\cos\omega_f\tau + (x_i^2/x_f)P\sin\omega_f\tau\right],$$

where $x_f := \sqrt{q_f/\omega_f}$ is the length scale of the final oscillator.

Now selecting the quadratic Zeeman energies q_i and q_f such that

$$x_f = x_i^2$$

gives,

$$X(t) = x_f\left[P\cos\omega_f\tau - X\sin\omega_f\tau\right]$$
$$P(t) = -x_f^{-1}\left[X\cos\omega_f\tau + P\sin\omega_f\tau\right],$$

corresponding to the desired symplectic transformation $(X, P) \mapsto M(t)(X, P)$, discussed above. In this case the quantum variances for the initially prepared vacuum state associated with the polar condensate are squeezed, time-independent and Heisenberg limited for $t \geq T$,

$$\Delta X^2(t) = \frac{1}{2}\frac{1}{\sqrt{1-2|c|/q_f}} = \frac{1}{2}\frac{1}{1-2|c|/q_i}$$

$$\Delta P^2(t) = \frac{1}{2}\sqrt{1-2|c|/q_f} = \frac{1}{2}(1-2|c|/q_i).$$

Based on the above analysis, the spin-squeezing parameter in the original variables of the condensate at $q_f \to 2|c|^+$ can be described by

$$\xi^2_{Q_{yz}} = \frac{\Delta Q^2_{yz}}{N} = \sqrt{1-2|c|/q_f}. \tag{4.4}$$

We note that to achieve a squeezing variance of $1/\eta := 1-2|c|/q_i$ relative to the standard quantum limit, we need to approach within $1/\eta^2$ of the critical point $1-2|c|/q_f = 1/\eta^2$ and $q_i/q_f = 1+1/\eta$.

The sensitivity of the squeezing to the condition $x_f = x_i^2$, between q_i and q_f, can be computed by considering a small error δ in the value of q_f, i.e., $|\delta|/q_f << 1$, as the following approximate expression shows,

$$\Delta P^2(t) \approx \frac{1}{2}(1-2|c|/q_i)\left[1+\frac{\delta}{q_f}\frac{2|c|/q_f}{1-2|c|/q_f}\sin^2\omega_f\tau\right].$$

In the alternative form

$$\Delta P^2(t) \approx \frac{1}{2\eta}\left[1+\frac{\delta}{q_f}(\eta^2-1)\sin^2\omega_f\tau\right], \tag{4.5}$$

we observe that to sustain a momentum variance squeezing of $1/(2\eta)$ it is necessary that

$$\eta^2|\delta|/q_f << 1.$$

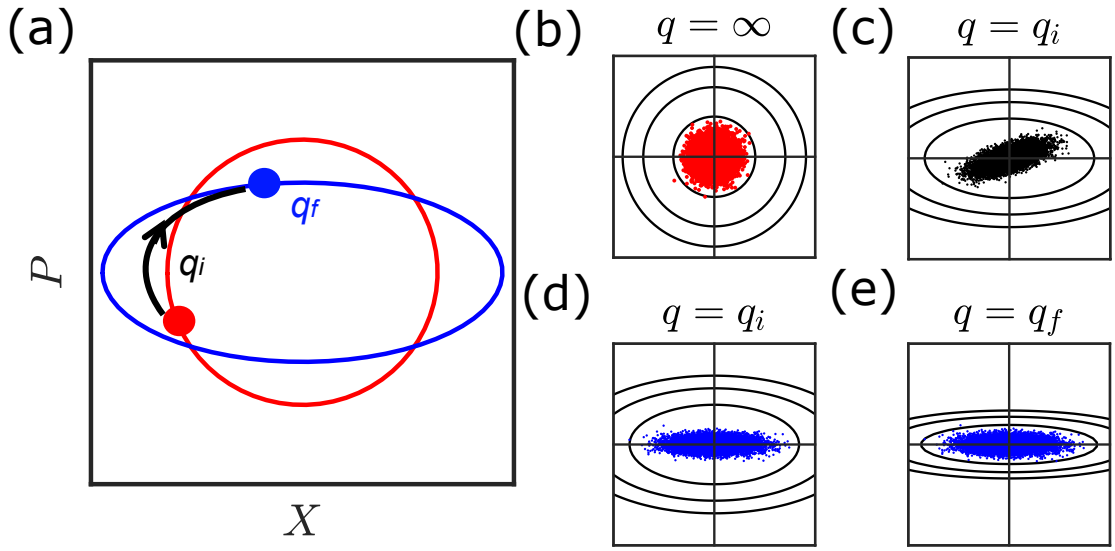

Figure 4.3: Illustration of the classical phase portrait of the double-quench protocol. (a) (X, P) (red dot) satisfies symmetric condition with an arbitrary phase in the polar state regime. The evolution creates squeezing in the final regime q_f orbit (blue solid line) by passing an intermediate q_i orbit for a quarter period (black arrow line). (b)-(e) is the ensembles evolution in $(X(t), P(t))$. The surrounding circular and elliptical curves represent the constant-energy level sets. The initial ensemble (b) satisfies the uncertainty relationships at $q = \infty$. The ensemble rotates while squeezing in the intermediate regime (c). At $t = T$, the phase space changes suddenly from $q = q_i$ (d) to $q = q_f$ (e), which locks the squeezing amplitude and angle. This is in agreement with the quantum harmonic oscillator description for achieving a time-stationary squeezed state.

A small error in control of the Zeeman energy value in the vicinity of the quantum critical point leads to a quadratic sensitivity to noise fluctuations. In experiments, the value of c is known to an accuracy of about 1% [14], while q_f is controlled to the level of several parts per million by the stability of the external magnetic field.

Analogous to the discussion in subsection 4.2.1, if we expand the system near $\rho_0 = 1$, we have two independent identical quantum harmonic variables (X, P) defined as $(-S_x/\sqrt{2N}, Q_{yz}/\sqrt{2N})$ and $(S_y/\sqrt{2N}, Q_{xz}/\sqrt{2N})$. We focus on $(-S_x/\sqrt{2N}, Q_{yz}/\sqrt{2N})$ due to the uncorrelated initial condition and the identical dynamics. The numerical simulation (Figure 4.4) shows that the double-quench protocol agrees with Equation 4.4 with a final time-invariant $\xi^2_{Q_{yz}}$. In Figure 4.5, the noise sensitivity from the numerical simulation is in good agreement with Equation 4.5. The classical phase space picture in Figure 4.3 shows the

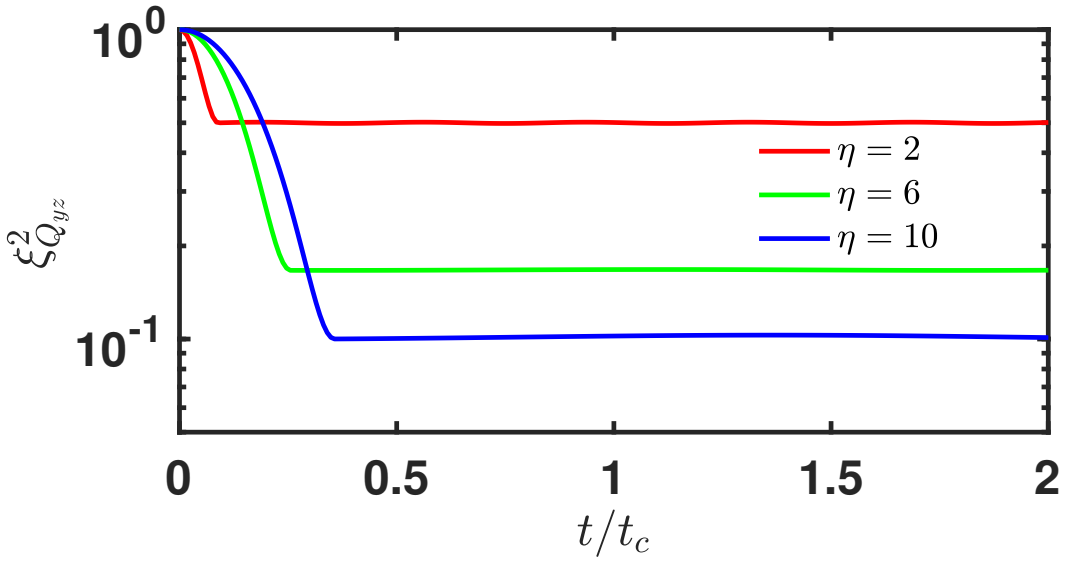

Figure 4.4: The mean-field numerical simulation result is in good agreement with Equation 4.4. A time-stationary squeezing can be generated through a pair of quenches, which maintains the squeezing after a few characteristic times.

evolution of an ensemble which passes from the initial state through a quarter period of intermediate dynamics to the final state with the most eccentric level curves.

Schrödinger picture

In the Schrödinger picture the protocol achieves a transformation from the ground state of the initial oscillator, whose quantum fluctuations are those of the polar condensate, to the ground state of the final oscillator created by a pair of quenches. The Schrödinger picture operators X and P can be written three separate ways in terms of annihilation and creation operators for the polar condensate $(a, a^\dagger)$, the intermediate oscillator $(a_i, a_i^\dagger)$ and the final oscillator $(a_f, a_f^\dagger)$, using the appropriate oscillator length scales x_i and x_f. Hence we can easily see that the oscillator variables are related by an SU(1,1) transformation [68]

$$a_i = \mu_i a - \nu_i a^\dagger, \text{ and } a_i^\dagger = \mu_i a^\dagger - \nu_i a,$$

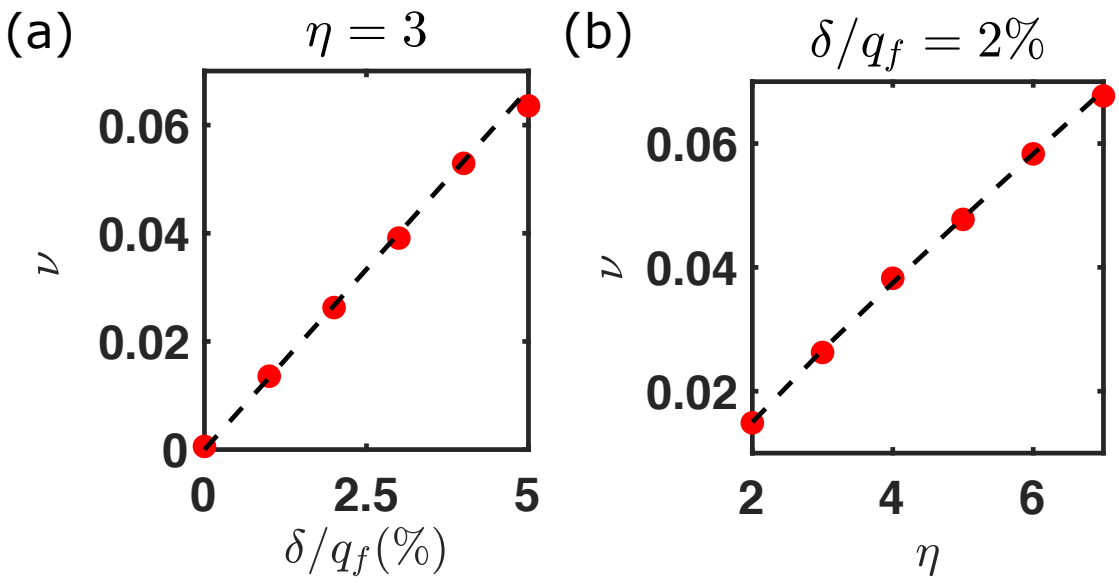

Figure 4.5: Comparison of Equation 4.5 with the mean-field simulation dynamics. We plot $\nu = 2\max(\Delta P^2(t)) - 1/\eta$ as the oscillation amplitude of $\sin^2 \omega_f \tau$ to illustrate the time-dependent noise fluctuations for $t > T$ when $\delta \neq 0$. (a) ν as a function of δ/q_f for $\eta = 3$. The red circles are the result from the simulation versus the analytic result (black dashed line). (b) The amplitude is bigger for higher squeezing η with $\delta/q_f = 2\%$.

where $\mu_i := (x_i + 1/x_i)/2$, $\nu_i := (x_i - 1/x_i)/2$, and $\mu_i^2 - \nu_i^2 = 1$. To achieve the target system discussed above we must control the Zeeman energy quenches so that $x_f = x_i^2$, and in this special case the final and intermediate oscillator variables are similarly related by

$$a_f = \mu_i a_i - \nu_i a_i^\dagger, \text{ and } a_f^\dagger = \mu_i a_i^\dagger - \nu_i a_i.$$

Let the vacuum state of the polar condensate oscillator be denoted $|\Phi\rangle$, so that $a|\Phi\rangle = 0$, and the vacuum state of the final oscillator be denoted $|\Omega\rangle$, so that $a_f|\Omega\rangle = 0$. The Schrödinger picture state vector at time $t = 0$ is $|\Psi(0)\rangle = |\Phi\rangle$, and the double quench produces $|\Psi(t)\rangle = |\Omega\rangle$, for $t \geq T$. To see this we introduce the Fock states $\{|n\rangle\}_{n=0}^{\infty}$ of the intermediate oscillator $a_i^\dagger a_i |n\rangle = n|n\rangle$.

Since for each $n = 0, 1, 2, ...$

$$\langle n|\mu_i a_i + \nu_i a_i^\dagger|\Phi\rangle = 0$$

it follows in the sudden approximation, that only even Fock states of the intermediate oscillator are generated in the first quench [69]

$$\langle 2n|\Phi\rangle = (-1)^n \frac{\sqrt{(2n)!}}{\sqrt{\mu_i} 2^n n!} \left(\frac{\nu_i}{\mu_i}\right)^n, \;\; n = 0, 1, 2, ...$$

A similar analysis shows that, $\langle 2n|\Omega\rangle = (-1)^n \langle 2n|\Phi\rangle$. Using the sudden approximation also for the second quench, with $\omega_i T = \pi/2$, gives

$$\begin{aligned} e^{-i\omega_i a_i^\dagger a_i T}|\Phi\rangle &= \sum_{n=0}^{\infty} (-1)^n |2n\rangle\langle 2n|\Phi\rangle \\ &= \sum_{n=0}^{\infty} |n\rangle\langle n|\Omega\rangle \\ &= |\Omega\rangle, \end{aligned}$$

so that the quarter period evolution between quenches prepares the final oscillator ground state, and the time independence of the position and momentum squeezing is readily understood.

The high-energy polar state

In Figure 4.2(b) near the pole at $\langle \hat{Q}_z \rangle = -1$, Equation 4.1 satisfies a quantum harmonic approximation to leading order with mass $m = (q/2)^{-1}$ and frequency $\omega^2 = q(q + 2|c|)/4$ in the high-energy polar state case (see section 4.5). The same double-quench sequence as described above can also be applied in this case, and the theory goes through with the redefinition of $x_f = \sqrt{q_f/(q_f + 2|c|)}$. All of the results for the low-energy polar state now apply when $|c| \mapsto -|c|$. The squeezing occurs in the position variable rather than the momentum. As a result, the high-energy polar state exhibits spin-squeezing given by

$$\xi_{S_x}^2 = \frac{\Delta S_x^2}{N} = \sqrt{q_f/(q_f + 2|c|)}, \tag{4.6}$$

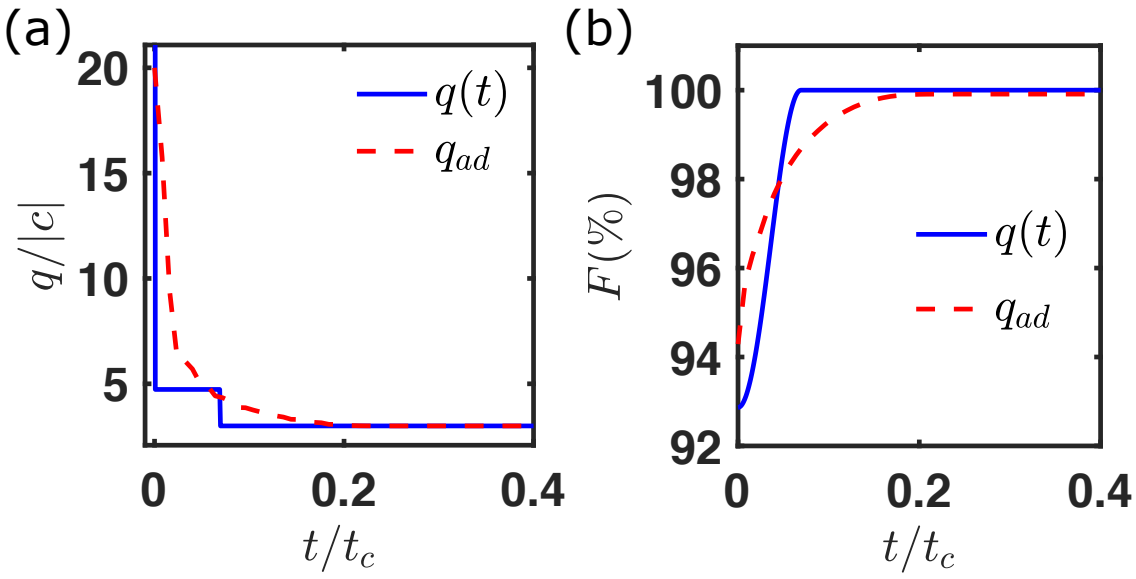

Figure 4.6: The comparison between the double-quench protocol and the adiabatic passage. (a) $q(t)$ (blue solid line) and q_{ad} (red dashed line) are shown as a function of t. (b) Fidelity F is plotted for q (blue solid line) and q_{ad} (red dashed line). Note q reaches higher fidelity of $|\Omega\rangle$ in a shorter time compared to q_{ad}.

as $q_f \to 0^+$.

4.2.2 Numerical treatment of full squeezing dynamics

To assess the limits of validity of the harmonic approximation and the role of finite system size N, we numerically solve the full quantum spin-1 dynamics in the single mode approximation (see section 2.5),

$$i\hbar\partial_t|\Psi(t)\rangle = \hat{H}(q(t))|\Psi(t)\rangle$$

with $\hat{H}(q(t))$ defined by Equation 4.1.

The time dependence of the magnetic field quench $q(t) = q_i\chi_{[0,T)}(t) + q_f\chi_{[T,\infty)}(t)$ is used in the simulation with the relation $1 + 2c/q_f = (1 + 2c/q_i)^2$ and $\omega_i T = \pi/2$ predicted by the harmonic approximation. The ground state of the final oscillator, denoted $|\Omega\rangle$ above, can be compared to the numerically computed lowest eigenvector of $H(q_f)$.

The quench dynamics may be compared to those of an alternative time-dependence

governed by the adiabatic passage function, $t \mapsto q_{ad}(t)$ [13]. The latter is determined by taking an initial value of $q = 20|c|$ and then optimizing the computed ground state fidelity, defined below, over a set of linear decreasing functions of time in the first time interval. The procedure is then repeated over the sequence of time intervals, to ensure that the fidelity with respect to the instantaneous Hamiltonian ground state at each step exceeds 99.9%. We note that this method outperforms the linear q ramp [14], the Landau-Zener ramp [70, 71, 72, 73] and the exponential ramp [74].

To verify that we achieve the many-body ground state, the computed fidelity $F = |\langle\Psi(t)|\Omega\rangle|^2$ is shown in Figure 4.6(b), where $|\Omega\rangle$ is the numerically-computed lowest eigenvector of $H(q_f)$. In these simulations, the quench function $t \mapsto q(t)$ results in a final fidelity F that satisfies $1 - F < 10^{-6}$, with the squeezing parameter $\eta \approx 2$, $N = 10^3$ and $q_f = 3|c|$. Although the overall quench sequence is apparently non-adiabatic, we can see the final state is indeed the many-body ground state at $q = q_f$. It is clear that the function $t \mapsto q(t)$ outperforms the optimized adiabatic ramp fidelity and does so in a shorter preparation time. For the squeezing variance factor η the preparation time is given by

$$T = \frac{\pi}{2\omega_i} = \frac{\pi}{2q_f}\frac{\eta}{\eta+1}\sqrt{\eta}.$$

By comparison, the adiabatic passage preparation time T_{ad} can be estimated by the Landau-Zener [70, 71] and Kibble-Zurek theories [75, 76], and is bounded by the relaxation time

$$T_{ad} \geq \frac{2\pi}{\omega_f} = \frac{2\pi}{q_f}\eta.$$

In Figure 4.6, this is illustrated for the case of $\eta \approx 2$.

We note that similar numerical computations can be used to investigate the high-energy polar state by employing the initial state $|\Psi(t=0)\rangle = |N/2, 0, N/2\rangle$ in the Schrödinger equation and the relation $1 - 2c/q_f = (1 - 2c/q_i)^2$ in the quench function $t \mapsto q(t)$.

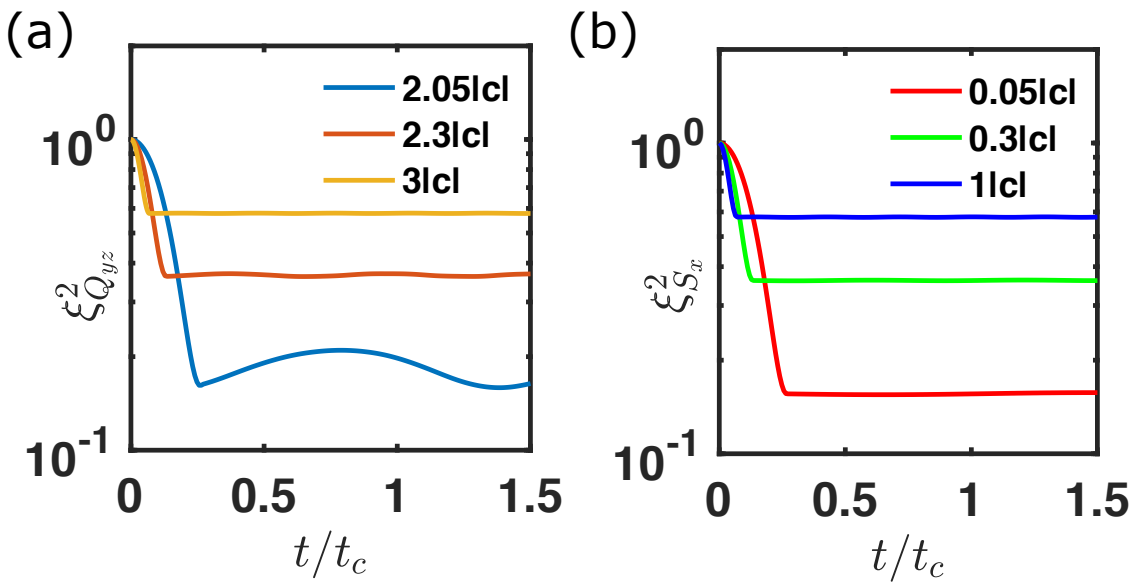

Figure 4.7: The system-size dependent effect ($N = 10^3$) on the shift of the QCP will lead to time-dependent oscillations in the final regime. (a) $\xi^2_{Q_{yz}}$ versus t curves are plotted for the low-energy polar state with $q_f \in [2.05|c|, 3|c|]$; (b) $\xi^2_{S_x}$ versus t curves are plotted for the high-energy polar state with $q_f \in [0.05|c|, 1|c|]$. By contrast with (a), there is no time-dependent oscillation as the critical point has no system-size dependent shift.

Numerical investigation of finite N effects

When we consider finite atom number N, system-size effects become important. For the high-energy polar state, the critical point is unshifted. For the low-energy polar state, q_c is a function of N and is shifted by an N dependent quantity

$$2 - q_c(N)/|c| = e^{1.462} N^{-0.6467} =: f(N)$$

(see section 4.4). Note that as $N \to \infty$, $q_c = 2|c|$ as assumed in the previous section. In the harmonic approximation, we showed the time-dependent oscillation is suppressed when $\eta^2|\delta|/q_f \ll 1$. If we assume δ is caused by the N-dependent shift $\delta = q_f(1 - q_c/|2c|) = q_f f(N)/2$ [2], then $\eta^2|\delta/q_f| = 0.02\eta^2$, where η^2 takes the values $(2^2, 3^2, 10^2)$ in Figure 4.7(a), where $N = 10^3$. This simple approximation gives good qualitative agreement with the numerical data. In Figure 4.7(b) by contrast, the high-energy polar state

[2] δ is estimated by the system-size shift from $q_f/q_c(\infty) = (q_f - \delta)/q_c(N)$

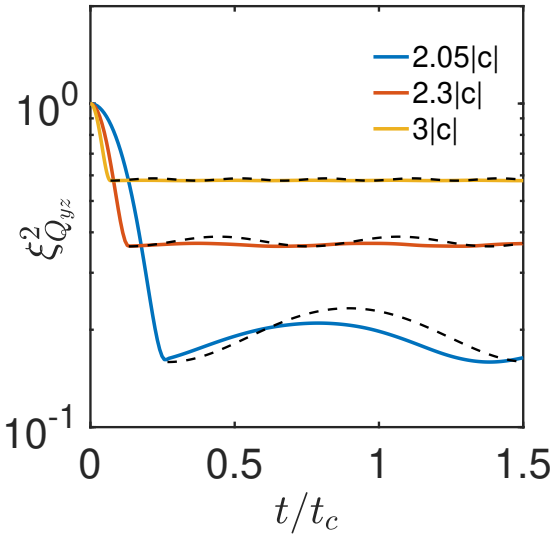

Figure 4.8: The oscillation from Equation 4.5 is compared to the simulation results of finite N. The black dashed curve is the estimation from imperfect final control assuming $\delta/q_f = 1 - q_c/2|c|$. The solid lines are from the finite N numerical quantum simulation. The simulation shows qualitative agreement with Equation 4.5.

shows no oscillation in the final regime due to the absence of a system-size dependent shift.

In the harmonic oscillator description, the maximum squeezing occurs at the QCP where the frequency $\omega_f \to 0$. However, there is a non-zero minimal energy gap Δ between the ground state and the first excited state [48] due to the finite atom number for the low-energy polar state. Thus the maximum squeezing computed by solving the ground state of $H(q_f)$ is limited by N as shown in Figure 4.9(a). The same maximum squeezing limit occurs for the high-energy polar state with a non-zero minimal energy gap Δ_E between the highest and the second highest excited states [77] (see section 4.4).

The fidelity of target states generated with the double-quench protocol is summarized in Figure 4.10 as a function of q_f and N.

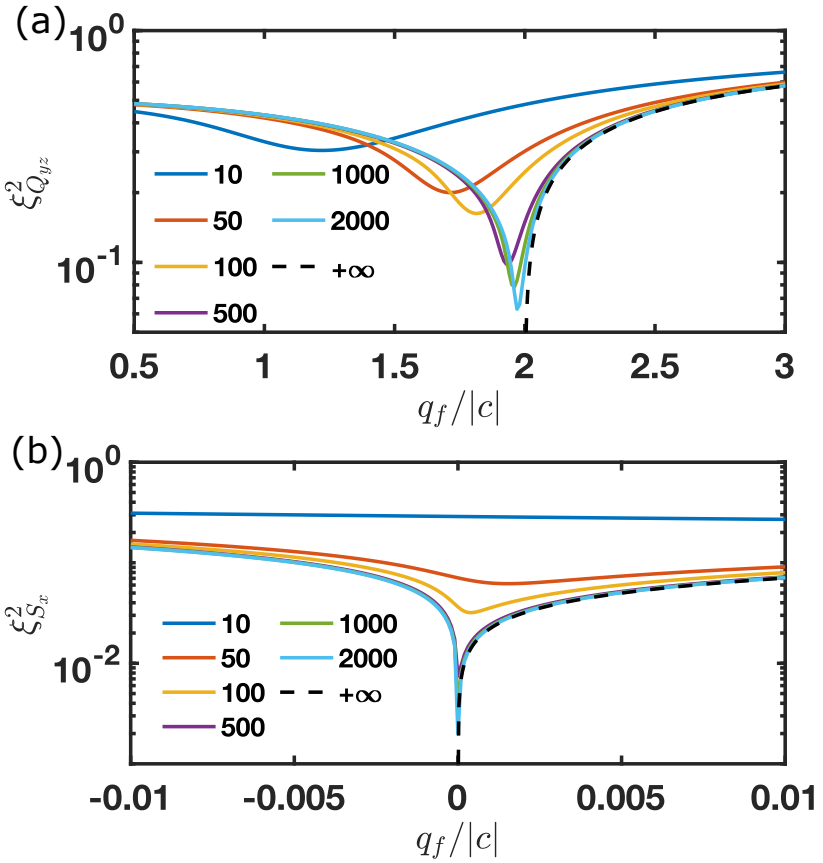

Figure 4.9: The finite system-size effect on the maximum squeezing due to the non-zero minimal energy gap. Analytic curves (black dashed lines) are compared with the full quantum simulation of $N \in [10, 2000]$ (solid lines). A sufficiently large N is necessary for the preparation of a highly squeezed state in the low-energy polar state case (a) and the high-energy polar state case (b).

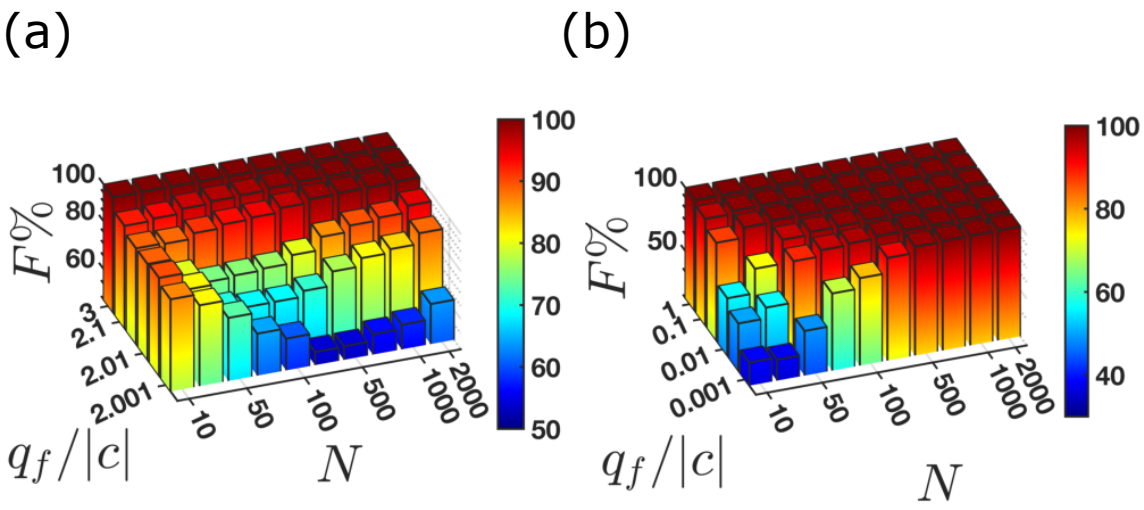

Figure 4.10: The fidelity of the target state is numerically computed as a function of atom number N and q_f: (a) low-energy polar state: as q_f approaches $2|c|$, large N is necessary but not sufficient for large squeezing due to the shifted QCP. (b) high-energy polar state: as q_f approaches $2|c|$, large N is sufficient for large squeezing due to the unshifted QCP.

4.2.3 Estimating the target state fidelity

In this section, we discuss a simple practical method to experimentally estimate the fidelity of production of the final oscillator ground state ($|\Omega\rangle := |0\rangle$) in the limit of large N (say $N \geq 10^3$). In practice, $N \approx 10^5$ is commonly measured in a spinor condensate of ^{87}Rb. If the system is prepared in the final target ground state $|0\rangle$, the squeezing uncertainties will be time-independent. On the other hand, if the system has an admixture of excited states, then the squeezed and antisqueezed quadrature fluctuations will vary harmonically at the frequency ω_f and produce a modulation in time given by the oscillation of the variances Osc$[\xi_\mu^2]$, $\mu = S_x, Q_{yz}$, defined below. By a spectral analysis of the numerically-computed wavefunctions, we find that only the ground and the first-excited states are significantly occupied.

The simplest model which mixes an excited state component to the final oscillator ground state is a coherent superposition in which the first excited state, $|1\rangle$, has probability

p_e,

$$|\Psi(t)\rangle = \sqrt{1-p_e}|0\rangle + e^{-i(\omega_f t+\phi)}\sqrt{p_e}|1\rangle,$$

with ϕ a relative phase.

We note the matrix elements for the final oscillator at $q = q_f$ are

$$\begin{aligned}\langle 0|\Delta X^2|0\rangle = -\langle 0|\Delta X^2|1\rangle = \frac{1}{2}\sqrt{\frac{q_f}{q_f+2c}} \\ \langle 1|\Delta X^2|1\rangle = \frac{3}{2}\sqrt{\frac{q_f}{q_f+2c}}.\end{aligned} \tag{4.7}$$

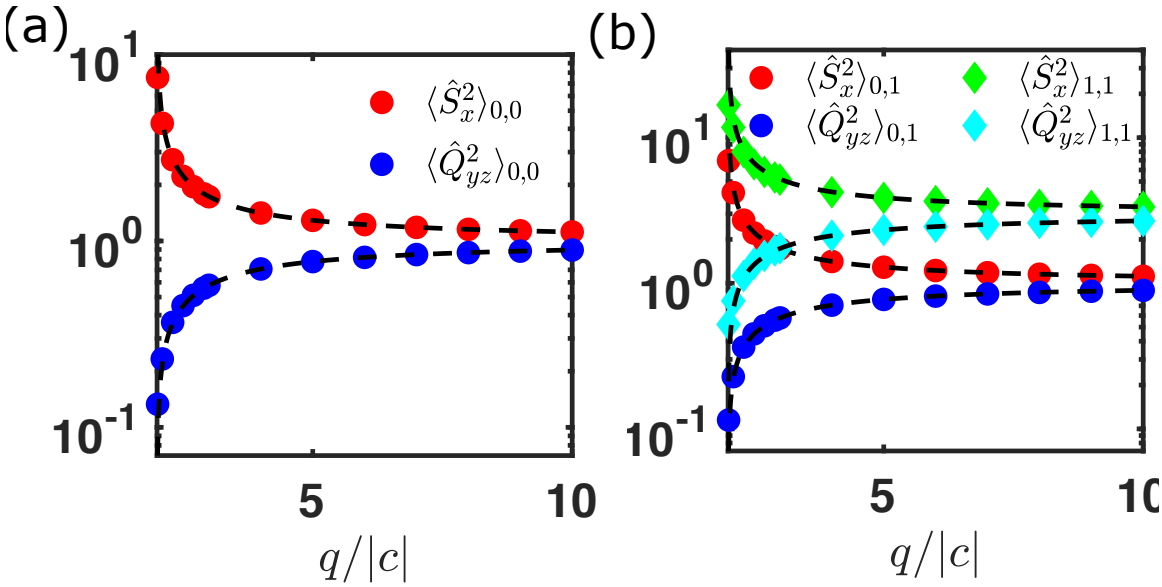

Figure 4.11: As noted in subsection 4.2.2, Equation 4.7 is checked against a full numerical computation of matrix elements of $\hat{S}_x^2/2N = X^2$ and $\hat{Q}_{yz}^2/2N = P^2$ using the ground and the first excited states of the final Hamiltonian. Here the subscripts $(0,0)$, $(0,1)$, and $(1,1)$ are the states used for the bracket. We have obtained excellent agreement for all matrix elements in the case of $N = 10^3$ and $q_f \in (2|c|, 10|c|]$.

The model predicts the mean-square oscillator fluctuations for $|\Psi(t)\rangle$ is given by, with

as before $1 - 2|c|/q_f =: 1/\eta^2$,

$$\begin{aligned}
&\langle\Psi(t)|\Delta X^2|\Psi(t)\rangle \\
&\quad = \left((1+2p_e) - 2\cos(\omega_f t+\phi)\sqrt{p_e(1-p_e)}\right)\frac{\eta}{2} \\
&\langle\Psi(t)|\Delta P^2|\Psi(t)\rangle \\
&\quad = \left((1+2p_e) + 2\cos(\omega_f t+\phi)\sqrt{p_e(1-p_e)}\right)\frac{1}{2\eta}.
\end{aligned} \tag{4.8}$$

To compare the simple model with the full numerical solutions we should first check that the ratio of the mean to the oscillation of the $\cos(\omega t)$ harmonic is independent of $x_f^2 = \sqrt{q_f/(q_f - 2|c|)}$ and depends only on p_e. In Figure 4.12(a), we show that this feature of the model is indeed consistent with full numerical computations.

In Equation 4.8, the amplitude of $\cos(\omega t)$ is defined as Osc$[\xi_\mu^2]$ and follows the relationship

$$(\text{Osc}[\xi_{S_x}^2]/\eta)^2 = (\eta\text{Osc}[\xi_{Q_{yz}}^2])^2 = 4p_e(1-p_e), \tag{4.9}$$

where $\xi_{S_x}^2 = 2\Delta X^2$ and $\xi_{Q_{yz}}^2 = 2\Delta P^2$. This result may also be compared with numerical computations (Figure 4.12(b)). Since in the model p_e is directly related to the fidelity F through $p_e = 1 - F$, measurement of Osc$[\xi_\mu^2]$ provides an estimate of the fidelity of the final ground state.

4.3 Conclusion

In summary, we have discussed a protocol for the preparation of time-stationary squeezed states in spin-1 BECs. The protocol simply involves a sequence of two reductions in the Zeeman energy of the system in an external magnetic field, in order to tune the system Hamiltonian close to a QCP. The proposed method appears to be simpler and faster than the typical adiabatic techniques. We also propose a procedure to measure the fidelity of

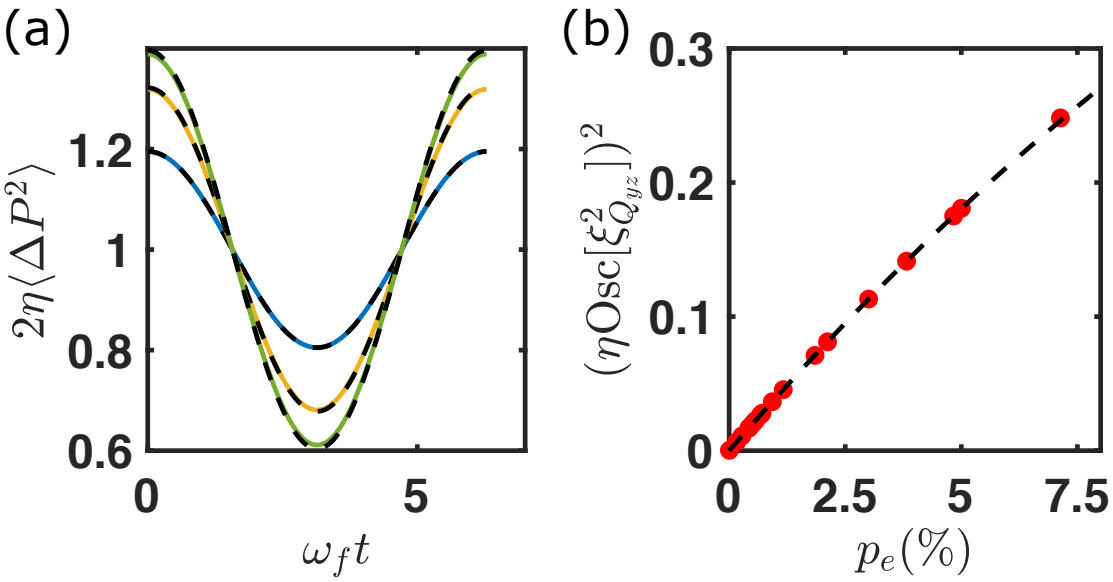

Figure 4.12: (a) The relative time-dependent oscillation in the final regime is compared with the prediction from the coherent superposition model of Equation 4.8 (dashed lines). $2\eta\langle\Delta P^2\rangle$ are numerical simulated as the solid curves with $\{p_e, q_f\} = \{0.01, 2.7\}, \{0.03, 2.1\}, \{0.05, 2.05\}$, $N = 4000$. (b) The relative oscillation amplitude predicted by the coherent superposition model of Equation 4.9 (dashed line) and the full quantum simulation show good agreement with each other. The correlation between $(\eta\mathrm{Osc}[\xi^2_{Q_{yz}}])^2$ versus p_e with $\eta \in [2, 6]$ suggest we can use $\mathrm{Osc}[\xi^2_\mu]$ as an indicator of the target state fidelity.

the state preparation by monitoring the harmonic oscillation of the asymptotic squeezing dynamics.

We expect the methods proposed in this paper may be applied to other similar many-body systems, for example, anti-ferromagnetic spinor condensates with $c > 0$ [78, 74], bosonic Josephson junctions [79] and the Lipkin-Meshkov-Glick model [80]. We believe that the proposed method is ideal for experiments, and could enable the observation of time-stationary squeezing in spin-1 systems for the first time.

4.4 Energy gap for finite system-size N

The energy gaps Δ and Δ_E and lowest energy eigenvectors are computed by numerical diagonalization of $\hat{H}(q)$ as a function of q and N in the Fock state basis as mentioned in subsection 4.2.2. The energy gaps are shown in Figure 4.13. Here the low-energy polar state gap is defined to be $\Delta := E_1 - E_0$. Similarly the two highest energy eigenstates can be computed with the energy eigenvalues of $E_{N/2}$ and $E_{N/2-1}$. The high-energy polar state gap is computed as $\Delta_E := E_{N/2} - E_{N/2-1}$. The value of q_c is system size-dependent for the low-energy polar state case following the approximate relationship $2 - q_c/|c| = e^{3/2}N^{-2/3}$ as plotted in Figure 4.14. From this q_c is computed by finding the location of the minimal energy gap over the simulated range. Using this relationship, the oscillation amplitude for ΔP^2 can be estimated assuming $\delta/q_f = 1 - q_c/2|c|$ from the quantum phase transition point shift relation $q_f/2|c| = (q_f - \delta)/q_c$ in Equation 4.5. The quantum phase transition for the low-energy polar states is second order [81] while for high-energy polar states is first order [77].

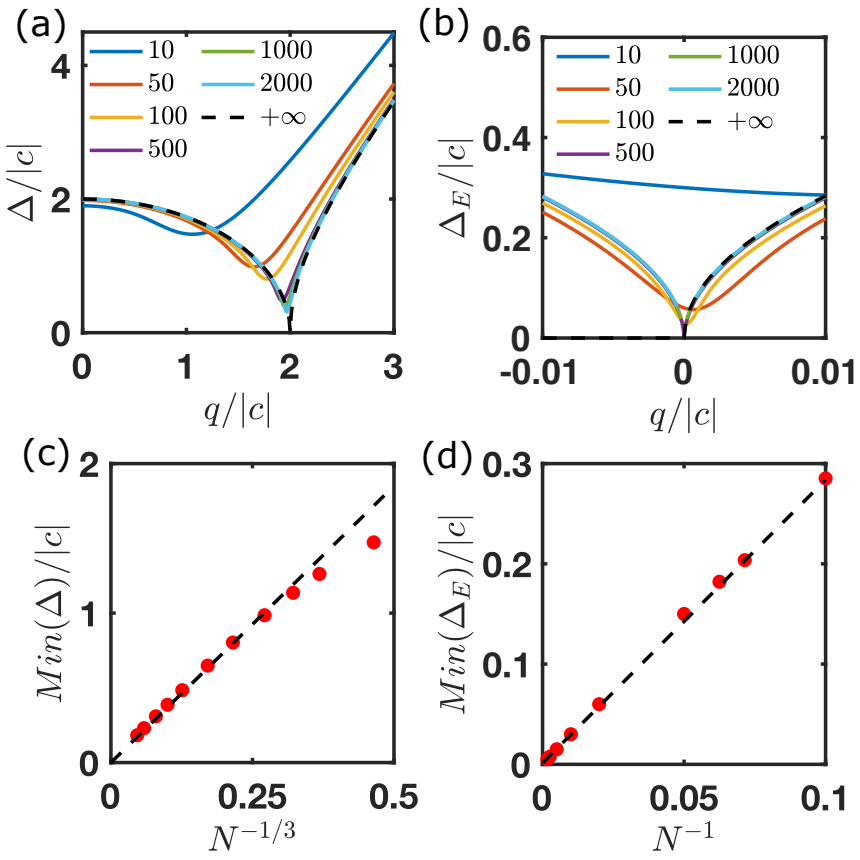

Figure 4.13: The finite system-size effect on the QCP shift and the minimal energy gap. Energy gap (a) Δ and (b) Δ_E are simulated for $N \in [10, 2000]$. (a) The QCP for the low-energy polar state is system-size dependent. (c) The minimum energy gap $Min(\Delta)$ is proportional to $N^{-1/3}$. (b) The QCP for the high-energy polar state is fixed when the system size varies. (d) The minimum energy gap $Min(\Delta_E)$ is linearly correlated to N^{-1}.

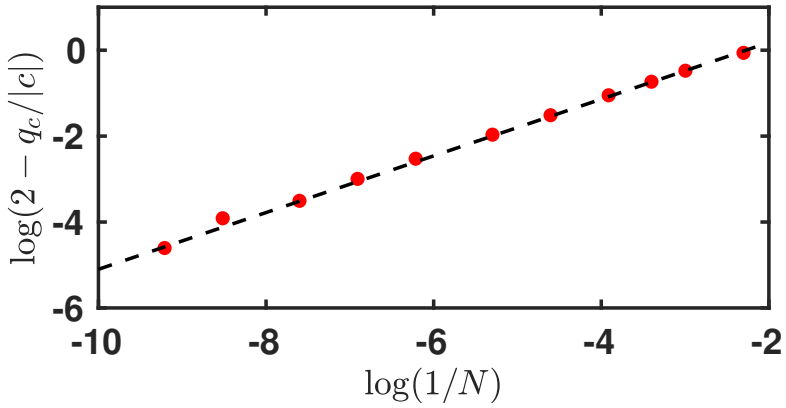

Figure 4.14: The QCP shift in Figure 4.13 (a) is computed as a function of N. The dashed curve is $\log(2-q_c/|c|) \approx \log(1/N)/3 + 3/2$ (the least square linear fit gives $\log(2-q_c/|c|) = 0.6467\log(1/N) + 1.462$). This gives the estimation of the system-size when applying the double-quench shortcut with good robustness.

4.5 Harmonic approximation for the high energy polar state

For $q \gg 2|c|$, the initial high-energy polar state of the Hamiltonian is the twin-Fock state, which in the Fock basis can be written as $|N/2, 0, N/2\rangle$. The twin-Fock state also gives a symmetric phase space distribution in $\{S_x, Q_{yz}\}$ and $\{S_y, Q_{xz}\}$. Near the pole on the $\langle \hat{Q}_z \rangle = -1$, Equation 4.1 can be approximated by

$$H = \frac{2c-q}{4}\frac{\hat{S}_x^2 + \hat{S}_y^2}{N} - \frac{q}{4}\frac{\hat{Q}_{yz}^2 + \hat{Q}_{xz}^2}{N} + O(\hat{S}_\mu^4, \hat{Q}_{\mu\nu}^4).$$

The commutation relationships are $\langle k|[-\hat{S}_x/\sqrt{N}, \hat{Q}_{yz}/\sqrt{N}]|k\rangle = i + O(N/2-k)/N)$ and $\langle k|[\hat{S}_y/\sqrt{2N}, \hat{Q}_{xz}/\sqrt{2N}]|k\rangle = i + O((N/2-k)/N)$ when $(N/2-k) \ll N$. The conjugate variables can be hence defined by neglecting the $O((N/2-k)/N)$ terms as

$$X_1 := -i\hat{S}_x/\sqrt{N}, \quad X_2 := i\hat{S}_y/\sqrt{N},$$
$$P_1 := i\hat{Q}_{yz}/\sqrt{N}, \quad P_2 := i\hat{Q}_{xz}/\sqrt{N}.$$

The quantum fluctuations are again controlled by two identical uncoupled quantum

oscillators with Hamiltonian

$$H = \frac{q-2c}{4}(X_1^2 + X_2^2) + \frac{q}{4}(P_1^2 + P_2^2).$$

With $[X_\alpha, P_\beta] = i\delta_{\alpha,\beta}$, we can identify the mass $m = (q/2)^{-1}$ and frequency $\omega^2 = q(q + 2|c|)/4$. Under this definition, the double-quench treatment can be applied. In this case the quantum variances for an initially prepared twin-Fock state are squeezed, time-independent and Heisenberg limited for $t \geq T$,

$$\Delta X^2(t) = \frac{1}{2}\frac{1}{\sqrt{1+2|c|/q_f}} = \frac{1}{2}\frac{1}{1+2|c|/q_i}$$
$$\Delta P^2(t) = \frac{1}{2}\sqrt{1+2|c|/q_f} = \frac{1}{2}(1+2|c|/q_i).$$

4.6 Optimal control considerations

The optimal control method minimizing the preparation time T through the cost function $J(T) = \int_0^T 1dt$ proposed for thermal states in [59] also provides the time-optimal solution to the transfer between initial and final oscillator ground states. In our system, the initial polar condensate state is prepared in a large quadratic Zeeman energy q_0 before $t = 0$. The optimal control sequence is a three step jump between q_0 and q_f (or equivalently, between $x_0 = \sqrt{q_0/\omega_0}$ and $x_f = \sqrt{q_f/\omega_f}$) characteristic of the so-called "bang-bang" switching between $\sup q(t)$ and $\inf q(t)$.

For the initial condition $x_0 = 1$ and $\tau := t - T \geq 0$, the phase space map $(X, P) \mapsto M(\tau)(X, P)$ is given by

$$M(\tau) = \frac{x_f}{1+x_f^2} \begin{pmatrix} x_f \cos(\omega_f \tau) - \sqrt{1+x_f^2+x_f^4}\sin(\omega_f\tau), \sqrt{1+x_f^2+x_f^4}\cos(\omega_f\tau) + x_f \sin(\omega\tau) \\ -x_f^{-1}\sin(\omega_f\tau) - x_f^{-2}\sqrt{1+x_f^2+x_f^4}\cos(\omega_f\tau), -x_f^{-2}\sqrt{1+x_f^2+x_f^4}\sin(\omega_f\tau)) + x_f^{-1}\cos(\omega_f\tau) \end{pmatrix}.$$

This matrix still satisfies the condition $\Delta X^2(t) = x_f^2/2$ and $\Delta P^2(t) = 1/(2x_f^2)$ although unlike our double quench protocol it is not a symplectic transformation. The total time required to complete the optimal control is $T = \frac{\eta}{2q_f} \arccos\left((1+\eta^2)/(1+\eta)^2\right) \approx \sqrt{\eta}/2|c|$, $\eta \to +\infty$. This time-optimal method has the same leading order dependence in η for the total time as the double-quench method but a short-pulse variation in Zeeman energy is very difficult to achieve experimentally in a spin-1 BEC system. (see Figure 4.15).

For Zeeman energy values in the compact set $q \in [q_f, q_0]$ the optimal control function is piecewise constant in time, as shown in the figure. The case in which the oscillator is initially prepared in a coherent vacuum state corresponds to $q_0 \to \infty$, so that the control values lie in a non compact set $q \in [q_f, \infty)$. In this case the optimal control reduces to a constant function plus a Dirac measure in time.

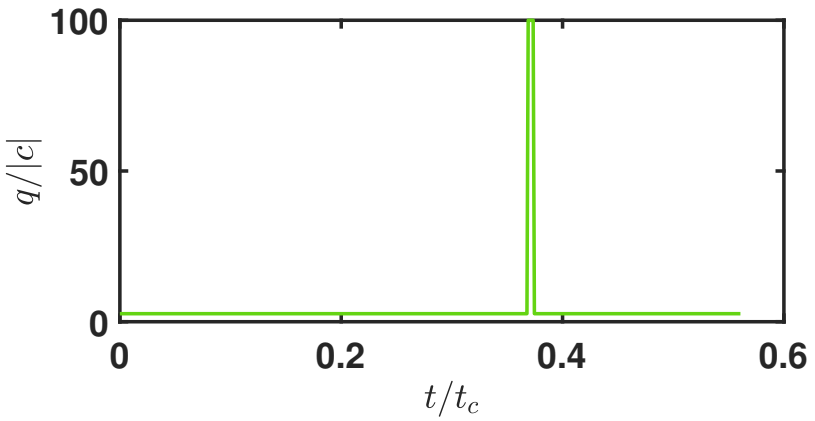

Figure 4.15: The optimal control function calculated for $q_0 = 100|c|, q_f = 3|c|$. The evolution begins with a switch from q_0 to q_f at $t = 0$ and then a double switch $q_f \to q_0 \to q_f$ over a very short interval below $t/t_c = 0.4$.

4.7 Spin-1/2 systems

While the main focus in this paper is the spin-1 condensate, we can also apply our theory to time-stationary quadrature squeezing in the spin-$1/2$ condensate, while previous works have focused on time-stationary number squeezing [82, 83] or time-varying quadrature squeezing [45]. For the spin-1/2 condensate we consider the Hamiltonian

$$\hat{H} = \frac{\Lambda}{2N}\hat{J}_z^2 - \hat{J}_x$$

[42], where $\hat{J}_{x,y,z}$ are collective spin-1/2 operators and Λ is a dimensionless atom-atom collision parameter. The classical phase space corresponds to the Bloch sphere. For $\Lambda = 0$, the ground state of the Hamiltonian is the polar state having $J_x = N/2$ and isotropy with respect to J_y and J_z. Near the $J_x = N/2$ pole, the Hamiltonian can be approximated by

$$\hat{H} = \frac{\Lambda + 1}{2N}\hat{J}_z^2 + \frac{1}{2N}\hat{J}_y^2 + O(\hat{J}_z^4, \hat{J}_y^4).$$

Since the commutation relation gives $\langle[\hat{J}_y, \hat{J}_z]\rangle = \langle i\hat{J}_x\rangle = iN/2$ near the J_x pole, the variables

$$X := \hat{J}_y/\sqrt{N/2}, P := \hat{J}_z/\sqrt{N/2}$$

are canonically conjugate. The system is accordingly described to leading order by the quantum harmonic oscillator

$$\hat{H} = \frac{\Lambda+1}{4}P^2 + \frac{1}{4}X^2.$$

We can identify the effective mass $m := ((\Lambda+1)/2)^{-1}$ and the frequency $\omega := \sqrt{\Lambda+1}/2$. The quantum phase transition point is $\Lambda = -1$. The dimensionless length scale $x = \sqrt{1/(m\omega)} = \sqrt{\Lambda+1}$ of the oscillator is reciprocal to its momentum scale.

We consider a double quench protocol analogous to that discussed in subsection 4.2.1. The double quench is described by the function

$$\Lambda(t) = 0\chi_{(-\infty,0)}(t) + \Lambda_i\chi_{[0,T)}(t) + \Lambda_f\chi_{[T,\infty)}(t)$$

and the time-stationary squeezing condition requires $x_i^2 = x_f$ and $T = \pi/(2\omega_i)$, that is $\Lambda_f = \Lambda_i^2 + 2\Lambda_i$ and $T = \pi/\sqrt{\Lambda_i+1}$. In this case, $(X, P) \mapsto M(t)(X, P)$, where $M(t)$ is given by Equation 4.3 as in the spin-1 case. The quantum variances for the initially prepared polar state are squeezed, time-independent and Heisenberg limited for $t \geq T$,

$$\Delta X^2(t) = \frac{1}{2}(\Lambda_f+1)$$
$$\Delta P^2(t) = \frac{1}{2}\frac{1}{\Lambda_f+1}.$$

Based on the analysis above, the spin-squeezing parameter in the original variables of the

condensate can be described by

$$\xi_{J_y}^2 = \frac{\Delta J_y^2}{N/4} = \Lambda_f + 1$$

which is squeezed as $\Lambda_f \to -1^+$ and

$$\xi_{J_z}^2 = \frac{\Delta J_z^2}{N/4} = \frac{1}{\Lambda_f + 1}$$

is squeezed as $\Lambda_f \to +\infty$. The analysis of the quantum fluctuations presented above is valid in the limit as $N \to \infty$. In common with the low-energy polar states of the spin-1 system, the quantum critical point $\Lambda = -1$ is shifted by an N dependent contribution, which we do not consider further here.

CHAPTER 5

SQUEEZED GROUND STATE EXPERIMENT

For quantum-limited metrology with N uncorrelated particles in an atomic clock or optical interferometer for example, the uncertainty principle provides the standard quantum limit (SQL) of relative measurement precision, $1/\sqrt{N}$. An important frontier of research in metrology is the development of techniques to surpass this limit using quantum squeezed states or other entangled states [42, 43]. These techniques are expected to play an important role in the next generation of quantum sensors [84, 85, 86]. Atomic Bose-Einstein condensates (BECs) with internal spin degrees of freedom are a promising platform for creating and characterizing atomic spin squeezed and other entangled states [87, 21]. These systems feature strong collisional spin interactions, tunable Hamiltonians with quantum phase transitions (QPT) and low-noise tomographic quantum spin state measurement capabilities that allow exploration of a wide range of interesting phenomena including squeezing [82, 11, 29], dynamical stabilization [15], parametric excitation [12], and studies of the quantum phase transition [13, 88, 49] including Kibble-Zurek universality [14].

The focus of this section is the creation and investigation of Gaussian squeezed ground states. These states arise naturally as the Hamiltonian is tuned near the symmetry-breaking QPT and offer the advantage that the squeezed state properties are determined by the properties of the final Hamiltonian rather than the details of the non-equilibrium evolution and are thus easier to characterize and control. In particular, the minimum squeezed quadrature angle for the ground state has a fixed orientation independent of the Hamiltonian parameters such as density and magnetic field. In contrast, the minimum squeezing quadrature angle in non-equilibrium methods is both time and atom number dependent [11], which poses serious challenges for highly squeezed states. Finally, spin squeezed ground states provide opportunities to more carefully investigate long-term evolution of entanglement in

spin ensembles because the squeezing is now in a stationary state. A distinguishing feature of the investigation described in this letter is the use of a double-quench shortcut [17] to approach the QPT that significantly shortens the state preparation time compared to adiabatic methods. Decreasing the preparation time improves both the fidelity of the target state and the detection limit due to uncorrelated atom losses.

For the ^{87}Rb $F = 1$ hyperfine state, $c < 0$ meaning the condensate has a ferromagnetic (FM) phase and a polar phase, separated by a QCP at $q = 2|c| \equiv q_c$.

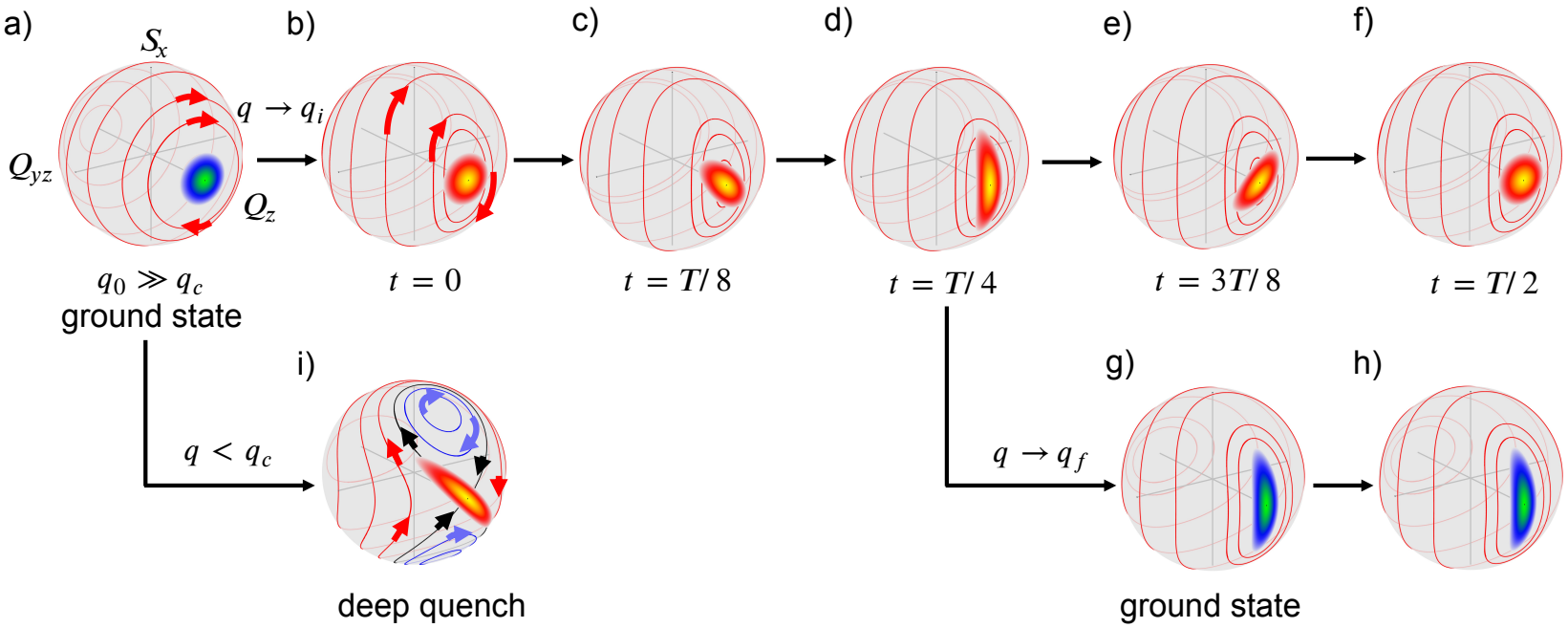

Figure 5.1: **The spin-1 states in the $\hat{S}_z = 0$ subspace and their evolution can be visualized on a $\{S_x, Q_{yz}, Q_z\}$ Bloch sphere. (a)** The initial state is an uncorrelated ground state at $q \gg q_c$ with symmetric uncertainties in S_x and Q_{yz}. **(b)-(f)** following a sudden quench to $q_i \gtrsim q_c$ at $t = 0$, the ground state remains polar, but the fluctuations evolve periodically along elliptical orbits with a frequency $\omega_i = 2\pi/T$. **(g)-(h)** A second quench at $T/4$ to a suitably chosen q_f will de-excite the condensate into a stationary squeezed ground state. **(i)** Standard non-equilibrium method of generating spin-1 squeezing following a sudden deep quench across the QCP to the FM phase [11, 28].

We begin by describing the basic idea behind the experiment. The starting point is a spin-1 condensate prepared in the $m_F = 0$ Zeeman state at a high magnetic field such that $q = q_0 \gg q_c$ and the spin interaction term of the Hamiltonian can be ignored. This is an uncorrelated ground state with Heisenberg uncertainty for the complimentary observables $\Delta S_x \Delta Q_{yz} = N$, where $\hat{S}_x$ is the collective spin operator in x direction, and $\hat{Q}_{yz}$ is the collective nematic operator between y and z direction. Throughout the text, operators are indicated by carets, while the corresponding symbol without the caret indicated their expectation value. The phase space of the system can be visualized on a Bloch sphere of $\{S_x, Q_{yz}, Q_z\}$ (see Figure 5.1) where the ground state is located at the $Q_z = 1$ pole with symmetric uncertainties in S_x and Q_{yz}. In earlier demonstrations of spin-nematic squeezing [11, 28], the squeezing was generated by non-equilibrium evolution from an unstable fixed point following a deep quench across the QCP to the FM phase as shown in Figure 5.1(i). In this work, we are interested in creating squeezing in the polar phase in the neighborhood of the QCP and, in particular, creating squeezing in the ground state of the system with $q \gtrsim q_c$. We again begin with a sudden quench from q_0, but now to a final field above the QCP, $q_i \gtrsim q_c$. At this field, the ground state remains polar in character, but the spin interactions are no longer negligible and distort the semi-classical orbits of the system into ellipses. Subsequent evolution of the initially symmetric uncertainties gives rise to periodic squeezing and unsqueezing with a frequency $\omega_i = \sqrt{q_i(q_i - q_c)}$ as shown in Figure 5.1(b)-(f) from the energy gap [12]. Of course, this is an excited state of the system with dynamically evolving observables, in this case the uncertainties ΔS_x and ΔQ_{yz}. Although this state is not a ground state of the Hamiltonian $\hat{H}(q_i)$, it is the ground state of another Hamiltonian $\hat{H}(q_f)$ where $q_i > q_f > q_c$. To end with the condensate in a ground state, we perform a second quench with a timing and final field value chosen to match the evolving state with the shape of the ground state of the final Hamiltonian. This second quench results in the system in the ground state of $\hat{H}(q_f)$ as shown in Figure 5.1(g)-(h).

The ground state of $\hat{H}(q_f)$ exhibits squeezing in the variance of Q_{yz} by an amount [17]:

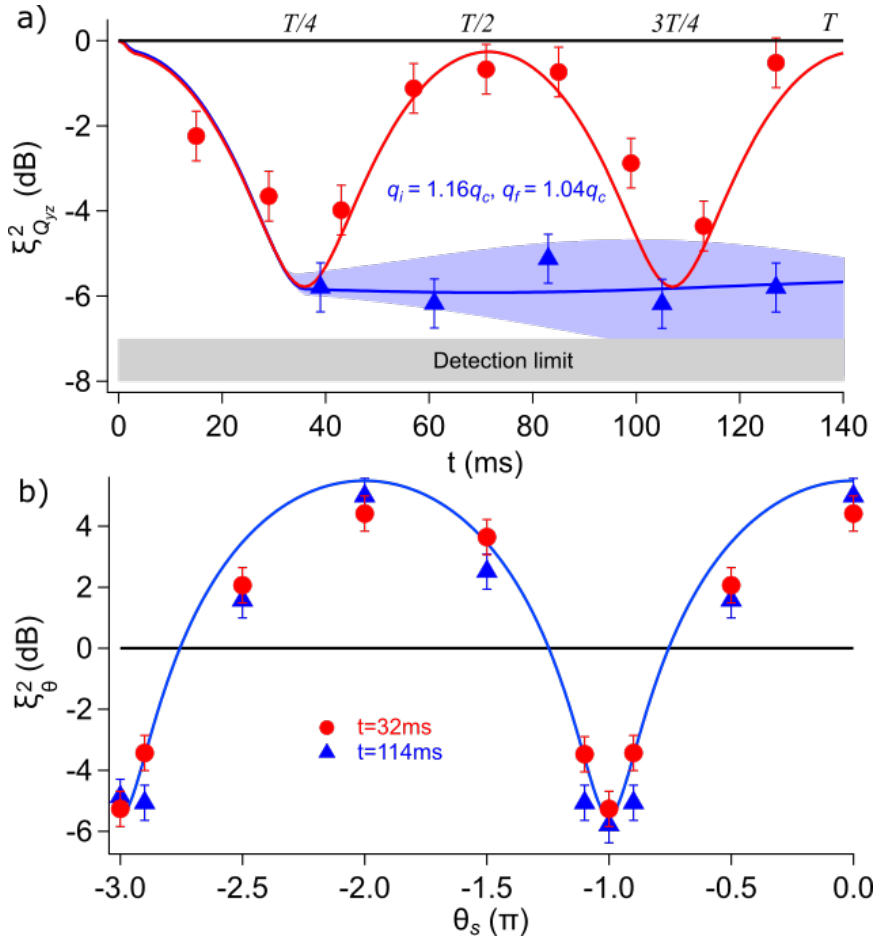

Figure 5.2: **Time-stationary squeezing and periodic squeezing.** **(a)** Measurement of time-stationary squeezing in the ΔQ_{yz} observable following the double quench sequence $q_0 \to q_i \to q_f$ designed to create a squeezed ground state at q_f (blue triangles). These data are compared to a single quench $q_0 \to q_i$ (red circles), which exhibit periodic squeezing and unsqueezing in ΔQ_{yz}. Simulation results with $c = -8.2 \pm 0.1$ Hz (blue shaded area) are compared with the data. **(b)** Tomographic measurements of the fluctuations at $t = T/4$ (red circles) and at a much later time ($t \sim 3T/4$) after the second quench (blue triangles). The error bars indicate the standard deviation of measured variance determined from 100 repeated measurements per data point.

$$\xi^2_{Q_{yz}} = \Delta Q^2_{yz}/N = 1/\eta, \tag{5.1}$$

where $1/\eta = \sqrt{1 - q_c/q_f}$, and anti-squeezing by an amount η in the complimentary observable S_x. In order to end in the ground state, the second quench needs to occur at a time $T/4 = \pi/(2\omega_i)$ and q_f needs to satisfy the relation $(q_i - q_c)/q_i = 1/\eta$. Of course, it is also possible to adiabatically ramp the Hamiltonian directly from $q_0 \to q_f$, but the double quench shortcut method is at least $\sqrt{\eta}$ faster than the shortest adiabatic ramp time $T_{adiab} \geq 2\pi\eta/q_f$ (see [17] for details).

We now turn to the experimental measurements. We first investigate the single quench non-equilibrium periodic squeezing following Figure 5.1(b)-(f). A condensate of 50k atoms is prepared in the $m_F = 0$ state in an optical dipole cross trap at a high field, $q_0 = 5q_c$. Following a sudden quench to $q_i = 1.16q_c$, the condensate is allowed to freely evolve. The mean spin populations do not significantly change as the condensate is still in the polar phase, however the spin fluctuations do evolve. In Figure 5.2(a), measurements of the time evolution of ΔQ_{yz} are shown that exhibit periodic squeezing and unsqueezing; measurements of ΔS_x show complimentary behavior of periodic anti-squeezing (see Figure 5.3). In Figure 5.2(b), tomographic measurements of the fluctuations at the point of maximum Q_{yz} squeezing ($t = T/4$) are shown. Each data point corresponds to a measurement at a different quadrature phase $\theta = \theta_s/2$, where θ_s is the relative phase between $m_F = 0$ and $m_F = \pm 1$ spin components:

$$\xi^2_\theta = \Delta(S_x \cos\theta + Q_{yz} \sin\theta)^2/N. \tag{5.2}$$

The data show up to -6 dB of squeezing and symmetric anti-squeezing. The data are compared with simulations that show good qualitative agreement; however, it is necessary to scale the simulations by $\xi^2 = (\xi^2_{sim})^{0.7}$ to quantitatively match the observed squeezing. In the figures throughout, the simulations are scaled to account for this discrepancy.

The simulations agree with the experimental data qualitatively but require a correction of $\xi^2 = (\xi^2_{sim})^{0.7}$ to match quantitatively. Interestingly, this correction is only required to match the squeezing measurements in the neighborhood of the QCP. For squeezed state generation using the deep quench method, the simulations match well without any adjustments, as shown in Figure 3.48. We do not currently understand this discrepancy; perhaps normally negligible effects such as magnetic anisotropy [89] or dipolar interactions [90] become significant near the critical point where the energy scale goes to zero.

We have also studied the periodic squeezing for different q_i, as shown in Figure 5.3. The temporal evolution rotates the distribution and creates periodic squeezing described by

$$\xi^2_{Q_{yz}} = \frac{1+\cos(\omega_i t)}{2} + \frac{1-\cos(\omega_i t)}{2\eta} \tag{5.3}$$

and $\xi^2_{S_x} = 1/\xi^2_{Q_{yz}}$. As q_i approaches q_c, $|\xi^2_{S_x}|$ and $|\xi^2_{Q_{yz}}|$ become bigger while ω_i gets smaller.

Also shown in Figure 5.2 are data taken following the double quench sequence $q_0 \rightarrow q_i \rightarrow q_f$ designed to achieve the squeezed ground state of $\hat{H}(q_f)$. In Figure 5.2(a), the data show that following the second quench to $q_f = 1.04 q_c$, the time evolution of ΔQ_{yz} remains constant at the level of the maximum squeezing previously observed, as expected for the ground state. The data are compared with a simulation result including a ± 0.1 Hz uncertainty in c. The precise values of T and q_f are determined from the single quench data. Tomographic measurements of the fluctuations of the ground state shown in Figure 5.2(b) taken at a much later time ($t \sim 3T/4$), are indistinguishable from measurements made of the periodic squeezing at ($t = T/4$), as expected. Furthermore, in addition to a constant squeezing amplitude, the maximum squeezing angle (the minimum quadrature angle) $\theta_{s,min} = \min\{\xi^2_\theta | \theta_s\} = -\pi$ remains constant following the second quench. This is in stark contrast to the deep quench method (Figure 5.1(i)) for which $\theta_{s,min}$ is a function of c, q and evolves dynamically. The experimental data is corrected for the photon shot noise and the background imaging noise and the detection limit of the squeezing is -7 dB. From the

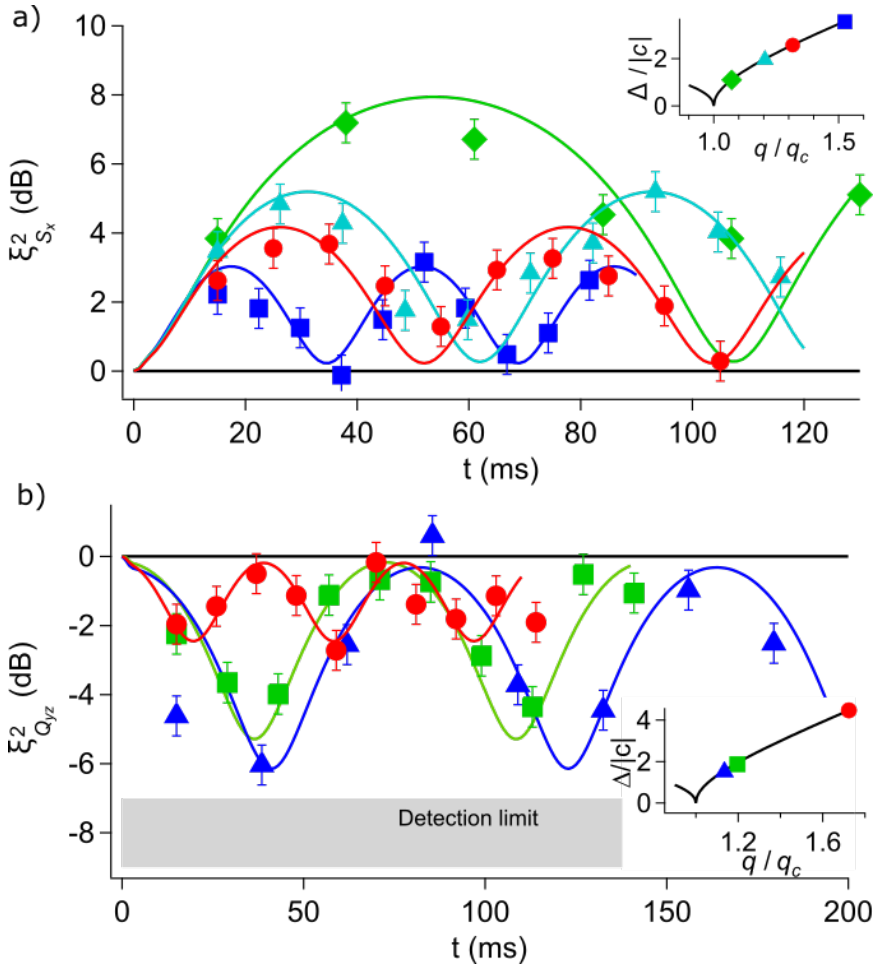

Figure 5.3: The periodic quadrature variance data of (a) S_x and (b) Q_{yz}. The insets show the relative distance from the QCP. As q_i approaches q_c, $|\xi^2_{S_x}|$ and $|\xi^2_{Q_{yz}}|$ become bigger while ω_i gets smaller. Solid curves are the simulation result with corrections. Inset: The measured oscillation frequency from the data is converted into the energy gap $\Delta = \hbar\omega_i$ and it measures the distance between q_i and q_c.

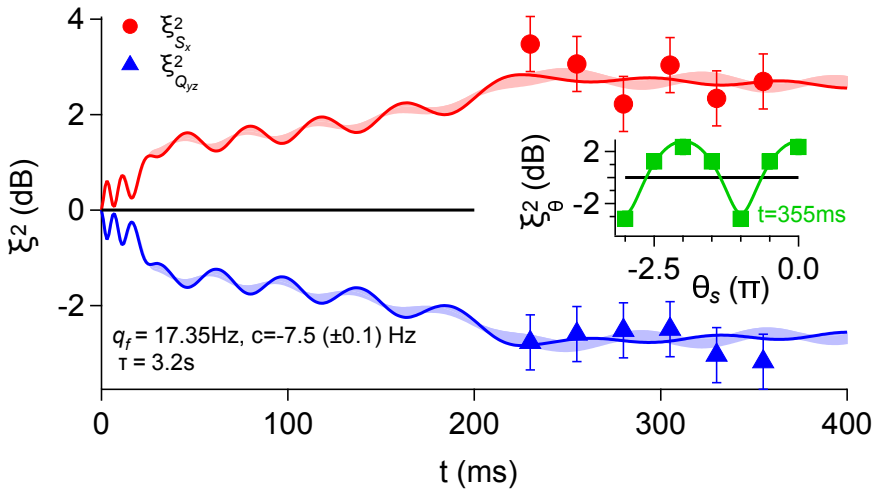

Figure 5.4: A squeezed ground state is generated with an adiabatic ramp. The adiabatic passage is more robust but slower compared to the shortcut protocol. The inset shows the spin-noise tomography measured at $t = 355$ ms. The simulations take the lifetime of the BEC into consideration with $\tau = 3.2$ s.

measurement of -6 dB of squeezing, it is possible to determine the entanglement breadth of the spin ensemble [91, 29, 30]. From this, we can conclude that a non-separable (entangled) subset of 600 particles is detected in the squeezed ground state. For comparison, we have also used an adiabatic ramp method to create the squeezed ground state. It is clear that the double quench method is superior, offering $\geq \sqrt{\eta}$ faster preparation and higher squeezing by minimizing atomic losses.

A high fidelity -3 dB squeezing generated by the adiabatic passage is measured in Figure 5.4. The assumption of constant atom number is no longer valid at timescale $>$ 100 ms due to the finite lifetime ($\tau = 3.2$ s) of our condensates. The simulation with $c(t) = -7.5 \exp\big(-2t/(5\tau)\big)$ Hz is plotted in Figure 5.4. As the time increases, the spin correlations loss $\sigma^2_{loss} = p(1-p)N^0$ [10] due to the lifetime leads to smaller detecable squeezing, where N^0 is the number of atoms without loss and $p = 1 - \exp(-t/\tau)$ is the probability of atom loss. A two-step linear ramp is used to realize the adiabatic passage. The adiabatic passage ramp takes 30 ms to ramp from B_0 to 600 mG and then takes 200 ms to ramp to B_f.

The degree of squeezing in the ground state increases as q_f approaches q_c according to

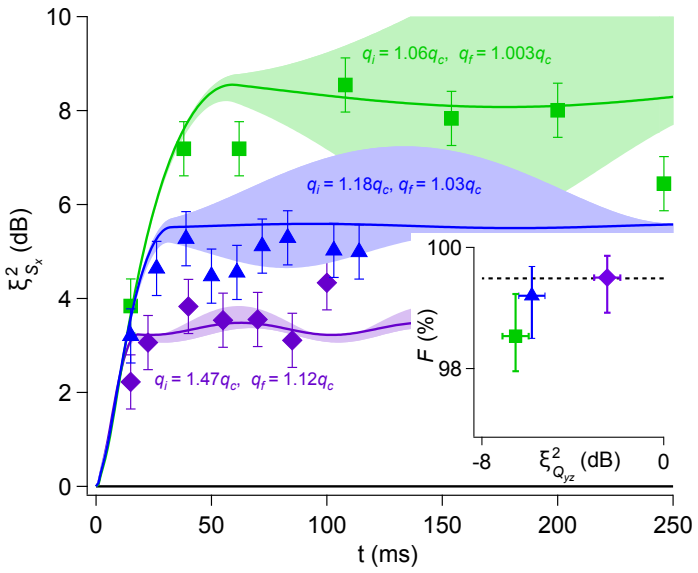

Figure 5.5: **Measurement of $\xi^2_{S_x}$ versus t following the double quench sequence for different q_f.** The solid lines are simulation results and the shaded regions reflect the sensitivity of the simulations to the uncertainty in $c = -8.5 \pm 0.1$ Hz. For the $q_f = 1.003q_c$ data (green squares), the uncertainty of c may lead to crossing over to the FM phase. Inset: the fidelity of the ground state F determined from the residual oscillation of $\xi^2_{S_x}$ after the second quench. The maximum fidelity that can be detected (dashed line) is limited by the detection noise.

Equation 5.1 because the semi-classical orbits near the pole become more elliptical (Figure 5.5). In Figure 5.5, noise measurements are made for three different final q_f values to show this dependency. We measure the anti-squeezed quadrature $\xi^2_{S_x}$ instead of the squeezing in ΔQ_{yz} to avoid limitations due to the detection noise limit. The sensitivity of the final state on the uncertainty in c (and hence q_c) increases at higher anti-squeezing amplitudes as shown by the shaded envelopes on the simulation curves. Tomographic measurements in Figure 5.7 confirm that the maximum squeezing angle $\theta_s = -\pi$ is independent of q_f.

Following the second quench, any residual oscillation of the measured fluctuations $A = \left(\max(\xi^2_{S_x}) - \min(\xi^2_{S_x})\right)/2$ is an indication of imperfect transfer into the ground state. Using a simple harmonic oscillator model [17], and defining $F = |\langle\Psi(t)|\Omega\rangle|^2$ as the fidelity of the targeted ground state $|\Omega\rangle$ of $\hat{H}(q_f)$, the fidelity can be determined from the

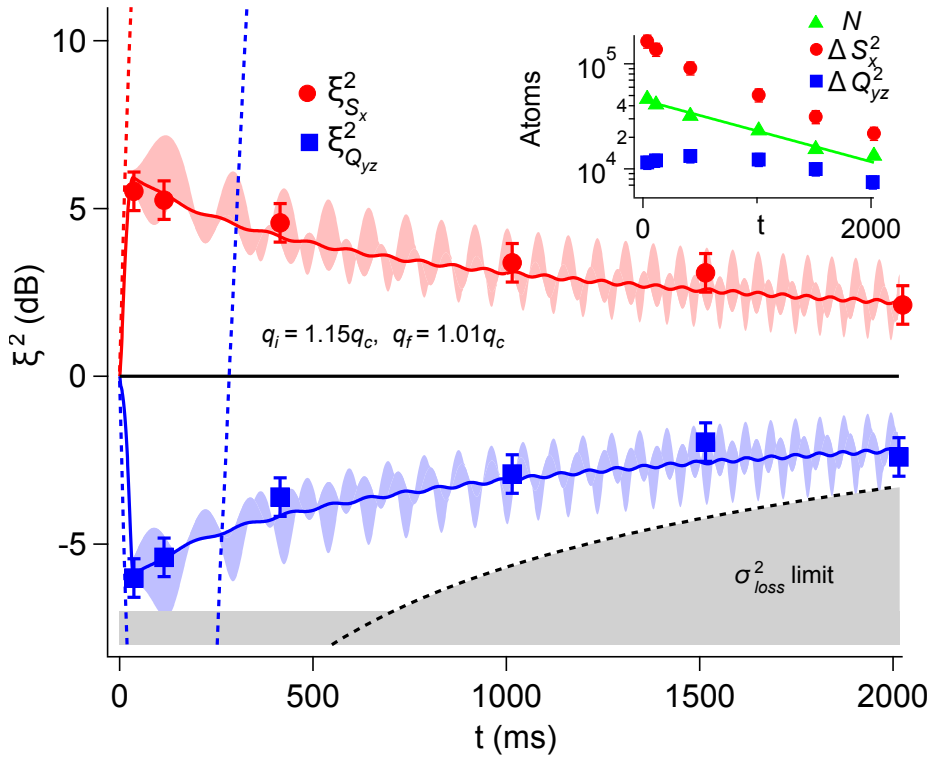

Figure 5.6: **Measurement of the long-term evolution of $\xi^2_{S_x}$ and $\xi^2_{Q_{yz}}$ in the squeezed ground state.** The simulations (solid lines) include the effects of atom loss $c(t) = (-8.7 \pm 0.1)\exp(-2t/5\tau)$ Hz. Here $q_c = 2|c(0)|$ is the critical point in the beginning of dynamics. The detection limit is dominated by the uncorrelated atom loss σ^2_{loss} (black dashed line) after 600 ms. The blue and red dashed lines are the maximum and minimum variance of the deep-quench squeezed state [11]. The inset shows ΔS_x^2 (red circles), ΔQ_{yz}^2 (blue squares) and N (green triangles) versus t.

oscillation amplitude through:

$$F \approx 1 - (A/2\eta)^2. \tag{5.4}$$

Using this result, we determine that $F > 98\%$ for squeezed ground states as shown in Figure 5.5 inset. The tolerance to the oscillation is high because a small amount of excitation can lead to significant noise fluctuation. F is lower at bigger $\xi^2_{S_x}$ because the sensitivity to c robustness increases. The maximum fidelity that can be detected is limited by the noise detection uncertainty.

In Figure 5.6, the long-term evolution of the squeezed ground state is measured. Atom

loss due to the finite lifetime of the condensate leads to a decrease in peak density n_0, with $n_0 \propto N^{2/5}$ in the Thomas-Fermi model [92]. This in turn affects the spinor dynamical rate and the QCP because $q_c \propto c \propto n_0$. Hence, as the condensate decays, one expects that q_f/q_c will increase, leading to a decrease in the squeezing. The data in the figure show this trend and compare well with simulations that include exponential atom loss with a time constant $\tau = 3.2$ s thus leading to the attenuation of the squeezing amplitude. The ground state maintains squeezing for over 2 s, and spin-noise tomography shows that the minimum squeezing quadrature angle remains fixed at $\theta_{s,min} = -\pi$ throughout the entire evolution. The atom loss also degrades the squeezing due to uncorrelated atom loss [10]. This limit to the squeezing is also included in Figure 5.6 as σ^2_{loss}. The uncorrelated loss becomes more important at longer timescales comparable to the condensate lifetime. The inset shows directly the time evolution of the variances ΔS_x^2 and ΔQ_{yz}^2 together with the exponentially decaying total atom number, N.

The extra spin-noise tomography data for the stabilized squeezing in the main context is plotted in Figure 5.7. It is evident that the squeezed ground state has a fixed $\theta_{s,min} = -\pi$ that is independent of q_f and t. One of the attractive features of our method is that no searching is needed to align the minimum squeezing direction to the detection variables.

The double quench method can be easily adapted to (pseudo) spin-1/2 systems such as bosonic Josephson junctions (BJJs) governed by a Hamiltonian of the form $\hat{H} = \alpha \hat{J}_z^{\,2} + J_x$. It can also be employed for spin-1 condensates with $c > 0$ [78, 74, 93, 94, 89] such as for sodium condensates. These systems have a QCP at $q = 0$ but lack a continuous quantum phase transition. The result in this paper can be also extended to other systems similar to ours, such as bosonic Josephson junction systems [79] and the Lipkin-Meshkov-Glick model [80].

In summary, this is the first realization of spin squeezed ground states in a spin-1 BEC within the proximity of the quantum phase transition point and provides a solid foundation for the application of our protocol. The result shows metrology improvements at a

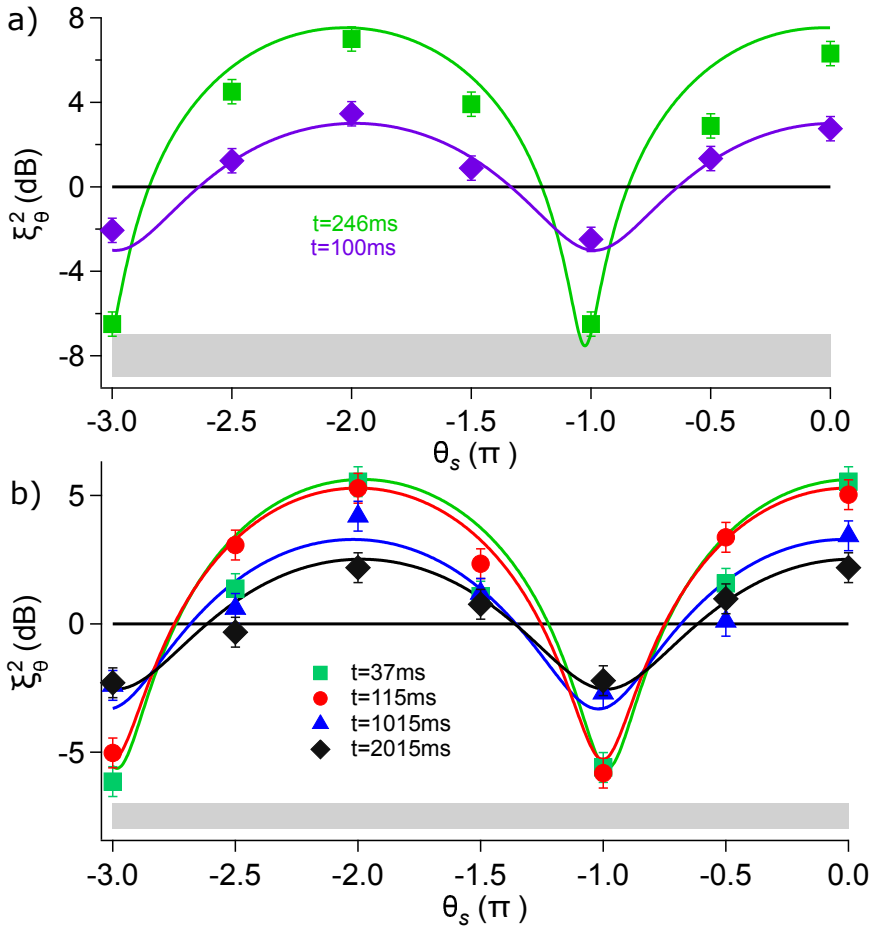

Figure 5.7: (a) Spin-noise tomography for stabilized squeezing with $q_f = 19.1$ Hz, $t = 100$ ms and $q_f = 17.05$ Hz, $t = 246$ ms. (b) Spin-noise tomography for states held inside the trap for $37, 115, 1015, 2015$ ms shows that $\theta_{s,min} = -\pi$ is fixed during the entire evolution.

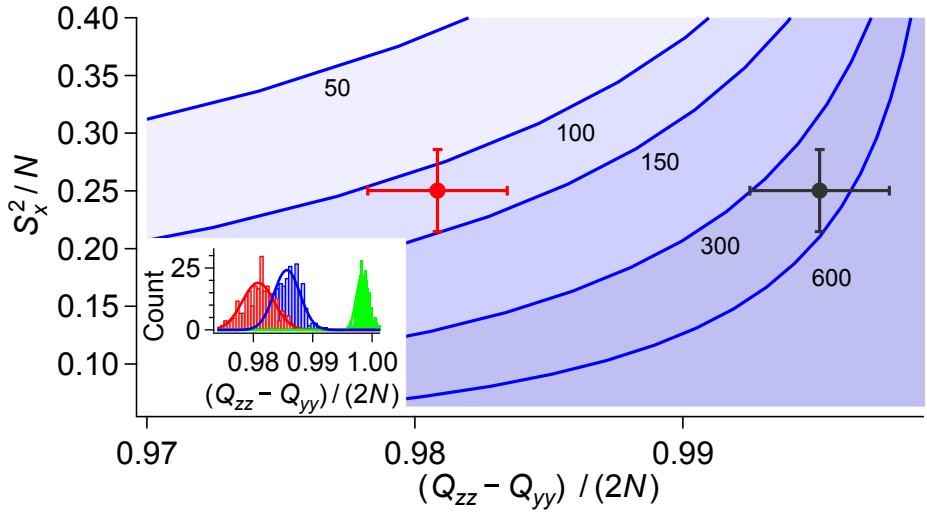

Figure 5.8: A non-separable subset of 150 particles (red dot) is detected in the squeezed ground state based on the entanglement breadth measurement. The corrected spin length based on $\lambda = 850$ nm laser pollution (black dot) shows a 600 particles entanglement. Inset: Measurement of the spin length under different experimental conditions. Green bars are the measurement in the CO_2 trap which sets the detection limit for the maximum spin length. Blue bars are the data inside the cross trap at the condition $q \gg q_c$. The red bars are the measurements for a -6 dB squeezed ground state.

lifetime scale and the maintenance of the maximum squeezing angle in good agreement with theoretical predictions. Our method, implemented here near a second-order quantum phase transition, can also be used as a tool to measure the quantum phase transition precisely. This is exceptionally useful in condensed matter systems [95], for example, it can help answer the relationship between high-temperature superconductivity and the QCP in copper-oxide [96, 97, 98].

We measure the entanglement of squeezed ground states through the entanglement breadth as shown in Figure 5.8. The entanglement breadth in the basis of the spin-nematic operators can be calculated in analogy with the Bloch sphere operators [29, 30]. The boundary labeled by the number k is given by the state

$$|\Psi\rangle = |\psi_k\rangle^{\otimes n} \otimes |\psi_p\rangle \tag{5.5}$$

which is a product of n ($= [N/k]$, integer part of N/k) copies of state $|\psi_k\rangle$ containing k

nonseparable spin-1 particles and state $|\psi_p\rangle$ composed of the remaining $p\ (= N - nk)$ particles. The state $|\psi_\mu\rangle$ $(\mu = k, p)$ represents the ground state of the μ particles Hamiltonian

$$H_\mu = (\hat{S}_x^{(\mu)})^2 - \lambda(\hat{Q}_{zz}^{(\mu)} - \hat{Q}_{yy}^{(\mu)})/2 \tag{5.6}$$

The boundary points are obtained as

$$\begin{aligned}\langle(\hat{Q}_{zz} - \hat{Q}_{yy})/2\rangle = n\langle(\hat{Q}_{zz}^{(k)} - \hat{Q}_{yy}^{(k)})/2\rangle_{|\psi_k\rangle} \\ + \langle(\hat{Q}_{zz}^{(p)} - \hat{Q}_{yy}^{(p)})/2\rangle_{|\psi_p\rangle}\end{aligned} \tag{5.7}$$

$$(\Delta\hat{S}_x)^2 = n(\Delta\hat{S}_x^{(k)})^2_{|\psi_k\rangle} + (\Delta\hat{S}_x^{(p)})^2_{|\psi_p\rangle} \tag{5.8}$$

The spin length here is different from the Dicke state's case because the spin vector is well-pointed in the $(Q_{zz} - Q_{yy})/2$ direction.

In the inset of Figure 5.8, the spin length $|(Q_{zz} - Q_{yy})/2| = 2N_0 - N$ is measured and studied for different experimental conditions. The $\lambda = 850$ nm laser contamination at the condition $q \gg q_c$ leads to a 1% fraction of atoms in $m_F = \pm 1$ compared to the ideal case in the sole CO_2 laser trap. The squeezed ground state at $q_f \gtrsim q_c$ further reduces the spin length by 1%. A non-separable subset of 150 (600 with correction) particles is detected in the squeezed ground state in Figure 5.8.

CHAPTER 6

OTHER THEORETICAL PROJECTS

6.1 All-microwave spin-1 control

The scheme for all-microwave control utilizes the time-delayed microwave pulses with different tones so that the transition degeneracies can be avoided by using the intermediate states. The purpose of applying all-microwave control instead of the RF + microwave control [16] is to convert the magnetic field fluctuation effect from phase (first-order sensitivity) to detuning (second-order sensitivity). This allows the measurement of noise tomography with $\vec{S} \neq 0$ state with a high-fidelity target state.

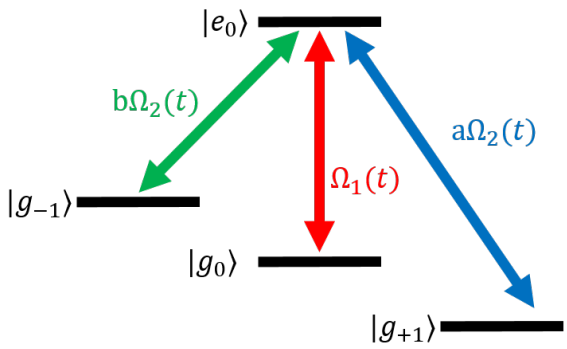

Figure 6.1: All-microwave scheme and 4-level system. For ^{87}Rb, $|g\rangle$ is $|F = 1\rangle$ and $|e\rangle$ is $|F = 2\rangle$.

The Hamiltonian of the all-microwave control is

$$H(t) = \frac{\hbar\Omega_1(t)}{2}(|e_0\rangle\langle g_0| + H.c.) + \frac{\hbar\Omega_2(t)}{2}(a|e_0\rangle\langle g_{+1}| + b|e_0\rangle\langle g_{-1}| + H.c.), \qquad (6.1)$$

where $\Omega_{1,2}(t)$ is the Rabi rates for different tunes and H.c. stands for Hermitian conjugate. Here $|a|^2 + |b|^2 = 1$ is the normalized ratio of Rabi rates between $\pm\Delta$ transition.

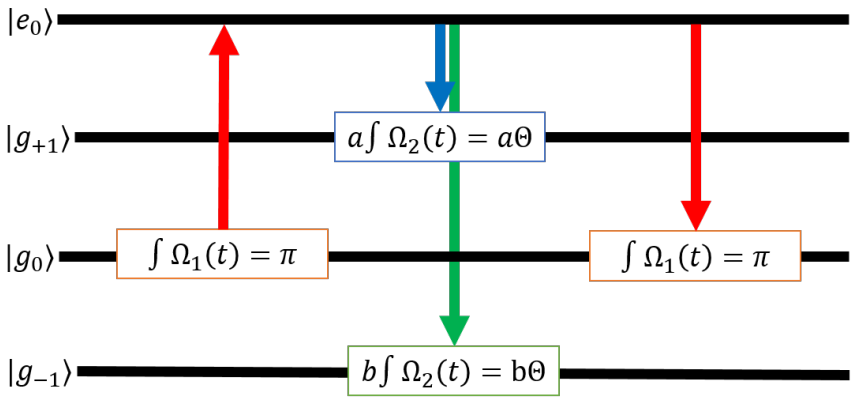

Figure 6.2: Gate sequence. $\int_0^{\tau_1} \Omega_1(t) = \pi$ (π pulse) brings all atoms from the initial state $|g_0\rangle$ to all atoms in $|e_0\rangle$. $\int_0^{\tau_2} \Omega_2(t) = \Theta$ transfers atoms in to $|g_{+1}\rangle, |g_{-1}\rangle)$ with a ratio $|a|^2/|b|^2$. Another π pulse afterwards brings the rest of atoms back to $|g_0\rangle$.

The gate sequence is shown in Figure 6.2 and the resulting state is derived as following. After the first π pulse, where $\frac{\Omega_1 t_1}{2} = \frac{\pi}{2}$ and $t = t_1$,

$$\begin{pmatrix} e_0(t) \\ g_{+1}(t) \\ g_0(t) \\ g_{-1}(t) \end{pmatrix} = \begin{pmatrix} -i \\ 0 \\ 0 \\ 0 \end{pmatrix}. \tag{6.2}$$

All atoms are transferred into $|e_0\rangle$ with an extra $-\pi/2$ phase. Then the two-tones pulse provides $\sigma\pm$ transitions, where $\frac{\Omega_2 t_2}{2} = \frac{\Theta}{2}$ and $t = t_1 + t_2$,

$$\begin{pmatrix} e_0(t) \\ g_{+1}(t) \\ g_0(t) \\ g_{-1}(t) \end{pmatrix} = -i \begin{pmatrix} \cos(\frac{\Theta}{2}) \\ -ia^* \sin(\frac{\Theta}{2}) \\ 0 \\ -ib^* \sin(\frac{\Theta}{2}) \end{pmatrix}. \tag{6.3}$$

A $\sin^2(\Theta/2)$ proportion of atoms is in $|g_{+1}\rangle, |g_{-1}\rangle)$ with a ratio $|a|^2/|b|^2$. The relative phase is also encoded in the coefficient a^* and b^*. The second π pulse bring all atoms back to the

spin-1 manifold, $t_3 = \frac{\pi}{\Omega_1}$ and $t = t_1 + t_2 + t_3$,

$$\begin{pmatrix} e_0(t) \\ g_{+1}(t) \\ g_0(t) \\ g_{-1}(t) \end{pmatrix} = \begin{pmatrix} 0 \\ -a^* \sin(\frac{\Theta}{2}) \\ -\cos(\frac{\Theta}{2}) \\ -b^* \sin(\frac{\Theta}{2}) \end{pmatrix}. \tag{6.4}$$

The atoms in $|g_0\rangle$ get an extra π phase due to the entire evolution. For a spin-1 system, the global phase ϕ_{global} can be ignored:

$$\begin{pmatrix} \xi_{+1} \\ \xi_0 \\ \xi_{-1} \end{pmatrix} = e^{i\phi_{global}} \begin{pmatrix} \sqrt{\frac{1-\rho_0+m}{2}} e^{i\frac{\theta_s+\theta_m}{2}} \\ \sqrt{\rho_0} \\ \sqrt{\frac{1-\rho_0-m}{2}} e^{i\frac{\theta_s-\theta_m}{2}} \end{pmatrix} = - \begin{pmatrix} a^* \sin(\frac{\Theta}{2}) \\ \cos(\frac{\Theta}{2}) \\ b^* \sin(\frac{\Theta}{2}) \end{pmatrix}. \tag{6.5}$$

As a result,

$$\begin{aligned} &\rho_0 = \cos(\frac{\Theta}{2})^2, m = (|a|^2 - |b|^2)\sin(\frac{\Theta}{2})^2, \\ &\theta_s = -(\phi_a + \phi_b), \theta_m = -(\phi_a - \phi_b). \end{aligned} \tag{6.6}$$

To achieve a known target state, the all-microwave pulse sequence needs to satisfy

$$\begin{aligned} &\Theta = 2\arccos(\sqrt{\rho_0}), |a| = \sqrt{(1 + \frac{m}{1-\rho_0})/2}, |b| = \sqrt{(1 - \frac{m}{1-\rho_0})/2}, \\ &\phi_a = -\frac{\theta_s + \theta_m}{2}, \phi_b = -\frac{\theta_s - \theta_m}{2}. \end{aligned} \tag{6.7}$$

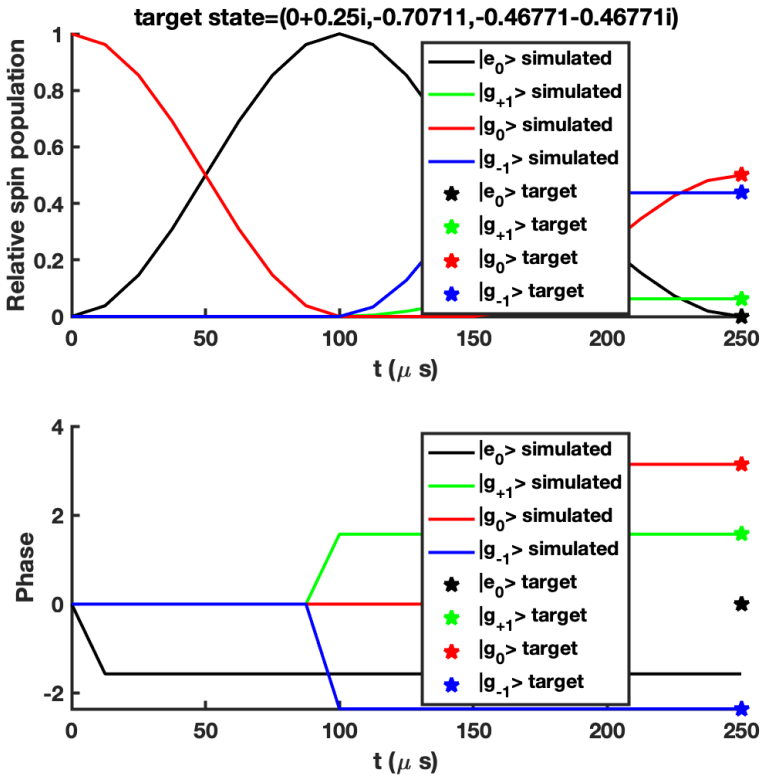

Figure 6.3: An illustration about using Equation 6.7 to generate a randomly-generated target state.

The Bloch sphere is represented by the spin vector $\vec{S} = (\langle S_x \rangle, \langle S_y \rangle, \langle S_z \rangle)$, where

$$
\begin{aligned}
\langle S_x \rangle =& \sqrt{\rho_0}(\sqrt{1-\rho_0+m}\cos(\frac{\theta_s+\theta_m}{2}) + \sqrt{1-\rho_0-m}\cos(\frac{\theta_s-\theta_m}{2})) \\
=& \cos(\frac{\Theta}{2})\sin(\frac{\Theta}{2})(\sqrt{1-(|a|^2-|b|^2)}\cos(\phi_a) + \sqrt{1+(|a|^2-|b|^2)}\cos(\phi_b)), \\
\langle S_y \rangle =& -\sqrt{\rho_0}(\sqrt{1-\rho_0+m}\sin(\frac{\theta_s+\theta_m}{2}) - \sqrt{1-\rho_0-m}\sin(\frac{\theta_s-\theta_m}{2})) \\
=& -\cos(\frac{\Theta}{2})\sin(\frac{\Theta}{2})(-\sqrt{1-(|a|^2-|b|^2)}\sin(\phi_a) + \sqrt{1+(|a|^2-|b|^2)}\sin(\phi_b)), \\
\text{and } \langle S_z \rangle =& m = (|a|^2-|b|^2)\sin(\frac{\Theta}{2})^2.
\end{aligned}
\tag{6.8}
$$

The spin vector length is defined as $|S|^2 = |S_x|^2 + |S_y|^2 + |S_z|^2$

$$\begin{aligned}|S|^2 =& 2\rho_0((1-\rho_0) + \sqrt{(1-\rho_0)^2 - m^2}\cos(\theta_s)) + m^2 \\ =& 2\cos(\frac{\Theta}{2})^2 \sin(\frac{\Theta}{2})^2 (1 + \sqrt{1-(|a|^2-|b|^2)^2}\cos(\phi_a + \phi_b)) + (|a|^2 - |b|^2)^2 \sin(\frac{\Theta}{2})^4\end{aligned} \tag{6.9}$$

A couple of special cases are discussed below to show how the control parameters change the spin vector.

case 1: $\Theta = \pi$,

$$\langle S_x \rangle = \langle S_y \rangle = 0, \langle S_z \rangle = |a|^2 - |b|^2, |S|^2 = |S_z|^2. \tag{6.10}$$

By controlling $|a|$, $\langle S_z \rangle$ is altered.

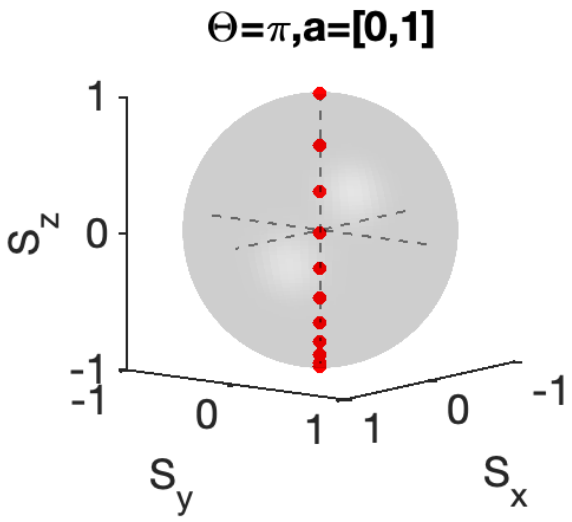

Figure 6.4: Bloch sphere scan a when $\Theta = \pi$, $|a|$ modulates the spin vector length.

case 2: $|a| = |b| = \sqrt{1/2}$,

$$\begin{aligned}
\langle S_x \rangle =& \cos(\frac{\Theta}{2}) \sin(\frac{\Theta}{2})(\cos(\phi_a) + \cos(\phi_b)) \\
\langle S_y \rangle =& -\cos(\frac{\Theta}{2}) \sin(\frac{\Theta}{2})(-\sin(\phi_a) + \sin(\phi_b)) \\
\langle S_z \rangle =& 0 \\
|S|^2 =& \sin(\Theta)^2(1 + \cos(\phi_a + \phi_b))/2 \\
\frac{\langle S_x \rangle}{\langle S_y \rangle} =& \frac{\cos(\phi_a) + \cos(\phi_b)}{\sin(\phi_a) - \sin(\phi_b)} = \cot((\phi_a - \phi_b)/2).
\end{aligned} \tag{6.11}$$

Θ and $\phi_a + \phi_b$ modulate the overall spin length. $\phi_a - \phi_b$ modulates the direction of the spin vector in S_x, S_y plane.

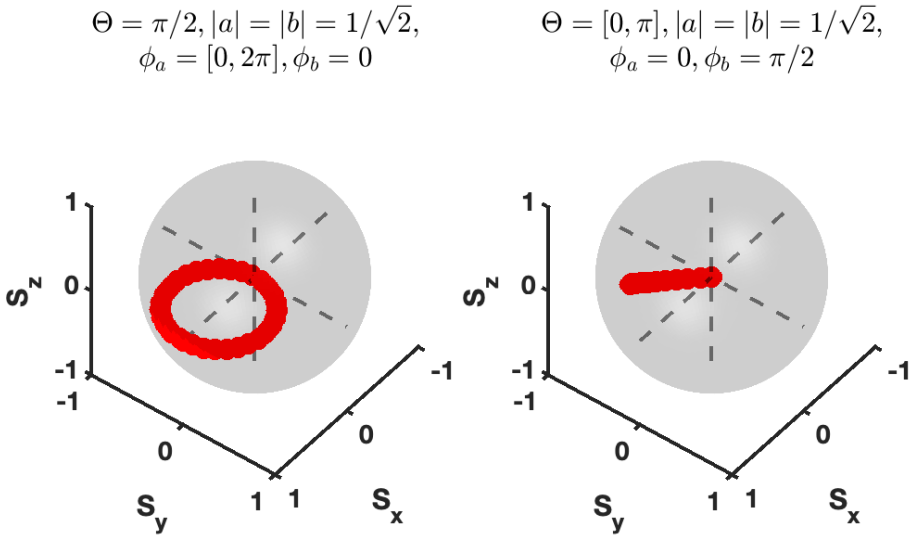

Figure 6.5: Bloch sphere ϕ_a and Θ scan when $|a| = |b| = 1/\sqrt{2}$. ϕ_a modulates the spin vector length and at the same time magnetic phase. Θ modulates the spin vector length while maintains the magnetic phase.

From the perturbation analysis, the sensitivity of the fidelity F of target state to the

parameters is studied.

$$
\begin{aligned}
F =& |\langle a'|a\rangle|^2 \\
\approx& |1 + a\Delta a \sin^2(\frac{\Theta}{2})(e^{-2i\phi_a} - e^{-2i\phi_b})|^2 = 1 + O(\Delta a), \\
F =& |\langle \Theta'|\Theta\rangle|^2 \\
\approx& |1 - \frac{1}{2}\Delta\Theta^2|^2 = 1 + O(\Delta\Theta^2), \\
F =& |\langle \phi'_a|\phi_a\rangle|^2 \\
\approx& |1 + i|a|^2\Delta\phi_a a \sin^2(\frac{\Theta}{2})|^2 = 1 + O(\Delta\phi_a),
\end{aligned}
\tag{6.12}
$$

where $a' = a + \Delta a$, $\Theta' = \Theta + \Delta\Theta$, and $\phi'_a = \phi_a + \Delta\phi_a$.

The experiment can be done by adding a mixer and an arbitrary function generator into the microwave circuits before the amplifier as shown in section 3.6. The arbitrary function generator is programmed with three tones to satisfy the parameters calculated in this section.

6.2 Periodic two-axis squeezing

The concept of squeezed spin states (SSSs) and the general principles have been established by [99]. Two mechanisms have been proposed in that paper. One-axis twisting (OAT) works as the building block for spin squeezing. Then, a two-axis counter-twisting mechanisms (TAT) is introduced as a natural extension of OAT and it is shown to further reduce quantum noise. Inspired by the work of [100, 101, 102] on spin-$1/2$ systems, we extended the idea to a spin-1 system. In this section, we present a way to produce TAT in a spin-nematic squeezed system by Floquet driving [103].

In the case $q = 0$, Equation 4.1 generates OAT for an atomic sample prepared in $|0, N, 0\rangle$.

$$
\hat{H}_{OAT} = \frac{c}{2N}\hat{S}^2 \tag{6.13}
$$

To further reduce quantum noise, simultaneously twisting about two orthogonal axes in opposite directions is introduced. Equation 6.14 creates TAT for initial state $|0, N, 0\rangle$.

$$\hat{H}_{TAT} = \frac{c}{2N}(\hat{S}^2 - (\hat{Q}_{yz}^2 + \hat{Q}_{xz}^2)) = \frac{c}{2N}(\hat{S}_x^2 - \hat{Q}_{yz}^2 + \hat{S}_y^2 - \hat{Q}_{xz}^2) \tag{6.14}$$

H_{OAT}, H_{TAT} and H_{SN} are displayed in Figure 6.6, using the mean-field method.

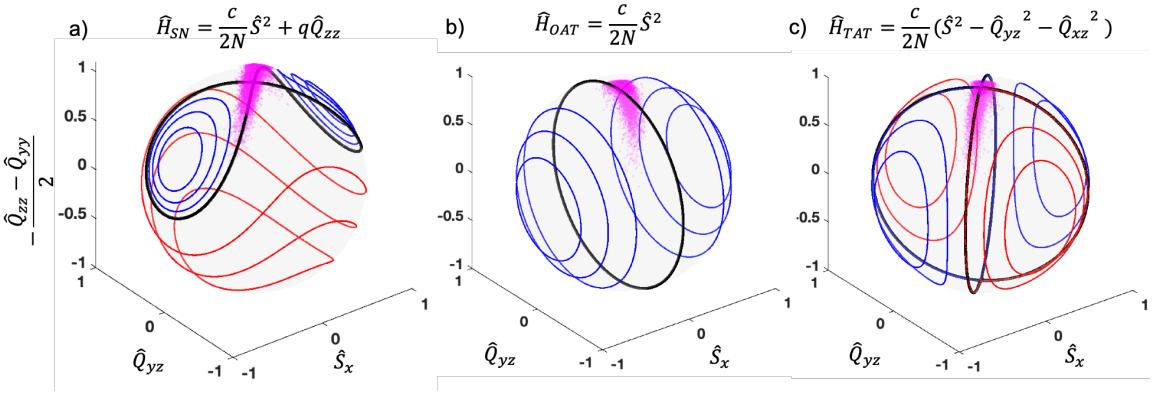

Figure 6.6: The level sets of a) $\hat{H}_{SN}$, b) $\hat{H}_{OAT}$ and c) $\hat{H}_{TAT}$. The black lines are the separatrix and the squeezing axis. The blue (red) lines indicate lower (higher) energy compared to the separatrix. Magneta points are the quasi-probability distribution of temporal evolution. Initial distributions squeeze along the separatrix. $\hat{H}_{OAT}$ and $\hat{H}_{TAT}$ have bigger squeezing amplitude compared to $\hat{H}_{SN}$ because the separatrix goes through great circles of SN sphere.

In order to generate the two axis squeezing Hamiltonian from H_{SN}, the method of periodic driving is applied. Our idea for transforming the SN squeezing to the TAT makes use of multiple $\pi/4$ pulse affected with the coupling term $\Omega\hat{Q}_{yz}$ and periodically modulating q. In the Rabi limit $\Omega \gg \frac{c}{2}$, the nonlinear interaction can be neglected while the collective spin undergoes driven Rabi oscillation. A $\pi/4$ pulse corresponds to $\int_{-\infty}^{\infty}\Omega(t) = \pi/4$ which transforms $R_{-\pi/4}(\hat{Q}_{yz})e^{i\hat{S}_x{}^2}R_{\pi/4}(\hat{Q}_{yz}) = e^{i((\hat{Q}_{zz}-\hat{Q}_{yy})/2)^2}$, where $R_{\pi/4}(\hat{A}) = e^{-i\hat{A}\pi/4}$. The Hamiltonian after transformation becomes

$$\begin{aligned}\hat{H}_F &= -i\log(R_{-\pi/4}(\hat{Q}_{yz})\hat{H}_{OAT}R_{\pi/4}(\hat{Q}_{yz})) \\ &= \frac{c}{2N}[(\frac{\hat{Q}_{zz} - \hat{Q}_{yy}}{2})^2 + (\frac{\hat{S}_y + \hat{Q}_{xy}}{\sqrt{2}})^2 + (\frac{\hat{S}_z - \hat{Q}_{xz}}{\sqrt{2}})^2].\end{aligned} \tag{6.15}$$

When the system evolves under $\hat{H}_{SN}$ for time t_1 and then $\hat{H}_F$ for time t_2 for a single period, the evolution operator becomes

$$\begin{aligned}\hat{U} &= e^{-it_1\hat{H}_{SN}}e^{-it_2\hat{H}_F} \\ &\approx e^{-i(t_1\hat{H}_{SN}+t_2\hat{H}_F)}exp(t_1t_2/2[\hat{H}_{SN},\hat{H}_F]+O(t_1t_2))\end{aligned} \tag{6.16}$$

due to Baker-Campbell-Hausdorff formula. Expanding for small t_1, t_2, $exp(t_1t_2[\hat{H}_{SN},\hat{H}_F]+O(t_1t_2)) \approx 1$. Hence we end up with $U = e^{-i(t_1\hat{H}_{SN}+t_2\hat{H}_F)}$ and $U^n \approx e^{-in(t_1\hat{H}_{SN}+t_2\hat{H}_F)} = e^{-it(\alpha\hat{H}_{SN}+\beta\hat{H}_F)}$. Here α, β are the relative scale of t_1 and t_2 compare to the period length $T = t_1 + t_2$.

The coefficients (α, β, q) are chosen to be $(\frac{13}{29}, \frac{16}{29}, \frac{3}{26}c)$ to create the effective TAT Hamiltonian.

$$\hat{H}_{EFF} = \frac{13}{29}(\frac{c}{2N}\hat{S}^2 + \frac{3c}{26}\hat{Q}_{zz}) + \frac{16}{29}\frac{c}{2N}\hat{S}_F^2 \approx \frac{1}{2}\frac{13}{29}\hat{H}_{TAT}. \tag{6.17}$$

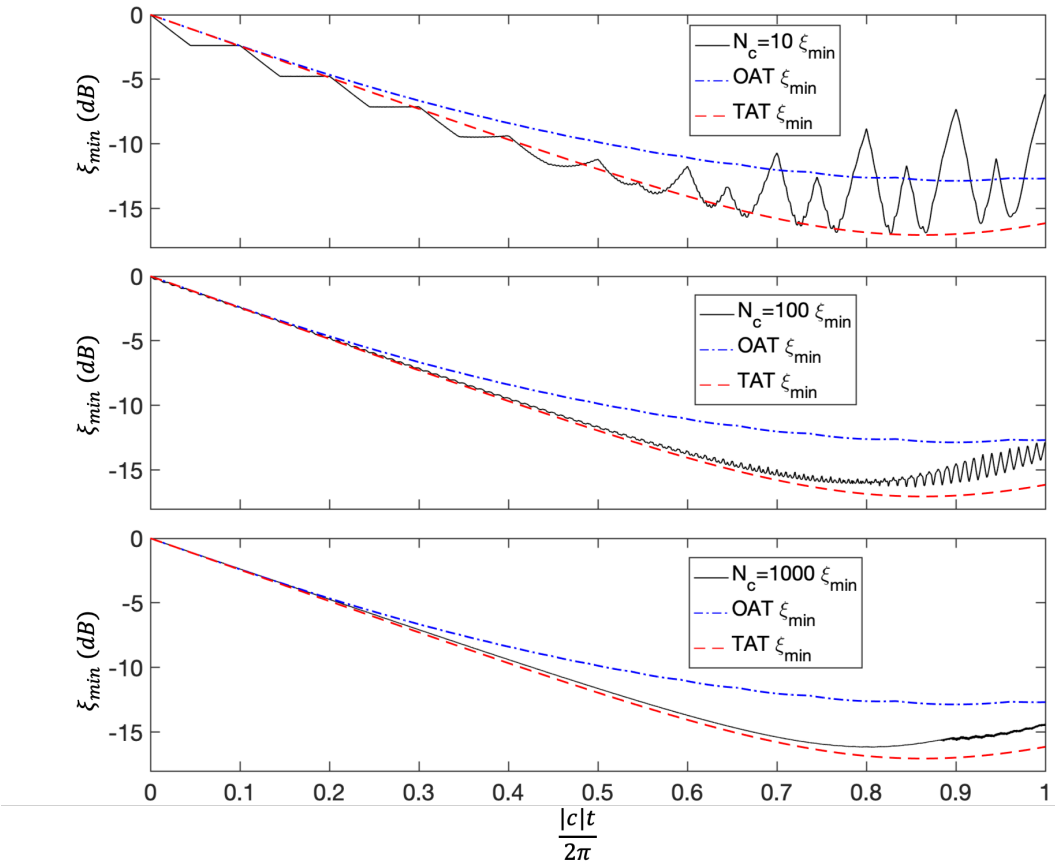

Figure 6.7: Spin squeezing parameter at different pulse numbers $N_c = 10$ (upper), 100 (middle), and 1000 (lower) in black solid lines compared with the $\hat{H}'_{OAT} = \frac{13}{29}H_{OAT}$ in blue dash-dot line and the $\hat{H}'_{TAT} = \frac{1}{2}\frac{13}{29}\hat{H}_{TAT}$ dynamics in red dashed lines, all for $N = 100$ atoms.

To compare with the Floquet drive results with the OAT and TAT results, we consider the case $N = 100$ numerically. The number of cycles of pulses N_c is used to calculate the time of one period $t_c = \frac{|c|t}{2\pi}/N_c$. To make the comparison on the same time scale, the TAT and OAT model are modified to be $\hat{H}'_{TAT} = \frac{1}{2}\frac{13}{29}\hat{H}_{TAT}$ and $\hat{H}'_{OAT} = \frac{13}{29}\hat{H}_{OAT}$ in Figure 6.7. In Figure 6.7, results for $N_c = 10, 100, 1000$ are displayed. With the increase of pulse number N_c, the Floquet dynamics approaches and eventually settles down closely to the effective dynamics of $\hat{H}_{TAT}$.

6.3 Fast generation of Dicke-like states

Dicke states are one of the entangled states that can beat the standard quantum limit to the Heisenberg limit. For spin-1 Dicke states, they can be represented as an annulus on the generalized Bloch sphere. Recently, a couple of breakthroughs [30, 49] is done by successfully generating Dicke-like states, which take advantage of all three components and thus offer higher interferometric sensitivity. The main difference between the Dicke-like states and Dicke states is that Dicke states are no longer a singly occupied ground state of the Hamiltonian $H = -S^2$. Instead, it can be a combination of hundreds of excitation states as long as the angular momentum $\langle L^2 \rangle / N^2 \approx 1$.

So far, the main method of generating the Dicke-like states is by quasi-adiabatically going across the phase transition, which requires a complicated ramp sequence as well as a long evolution time. In this section, a non-adiabatic shortcut is introduced to generate Dicke-like states with significant metrological gain. A single-step quench to $q \approx 1|c|$ across the quantum phase transition produces the largest anti-squeezing (angular momentum).

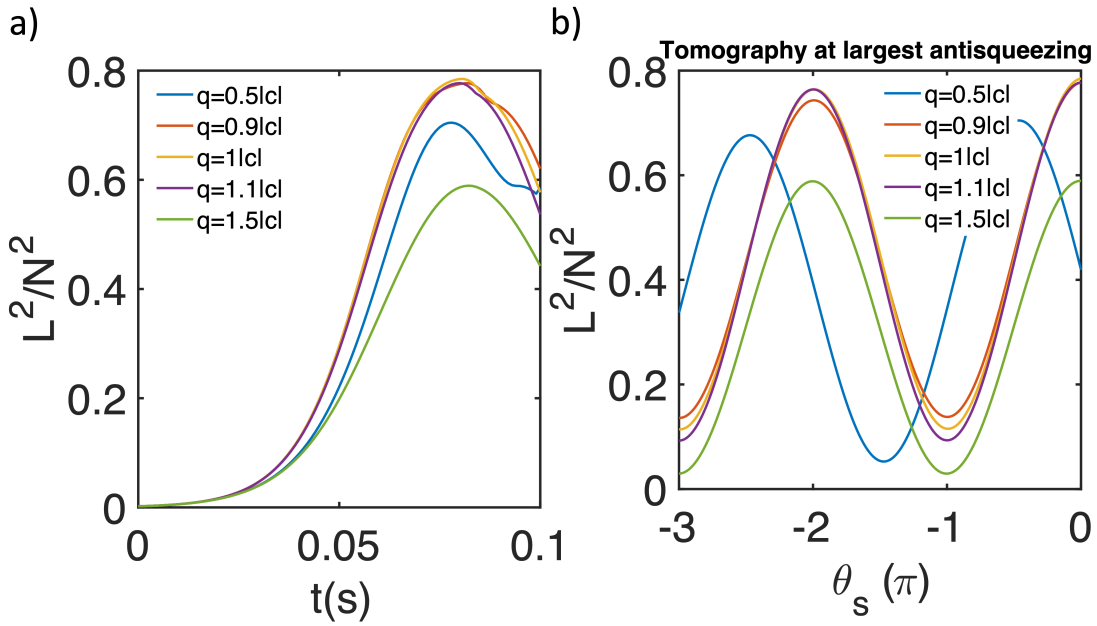

Figure 6.8: (a) By using a single step quench time evolution from $q = +\infty$ to near $q = 1|c|$, the max anti-squeezing searched with θ_s scan (Equation 5.2) is $\langle L^2 \rangle / N^2 = 0.8$ which is only 1 dB smaller than the Heisenberg limit. $c = -8.5$ Hz is used in the simulation. (b) The spin-noise tomography of the maximum anti-squeezing. The tomography suggests that the max angular momentum direction is at $\theta_s = 0$, which means the max anti-squeeizng is in S_x and S_y direction.

From the excitation spectrum in the Dicke basis (the eigenstates of $H = -S^2$), the initial state $|0, N, 0\rangle$ is at the highest excitation state of the system. After a certain amount of evolution time (70 ms), the non-equilibrium state has a strong overlap with the ground and low-excited states, where the angular momentum is maximized.

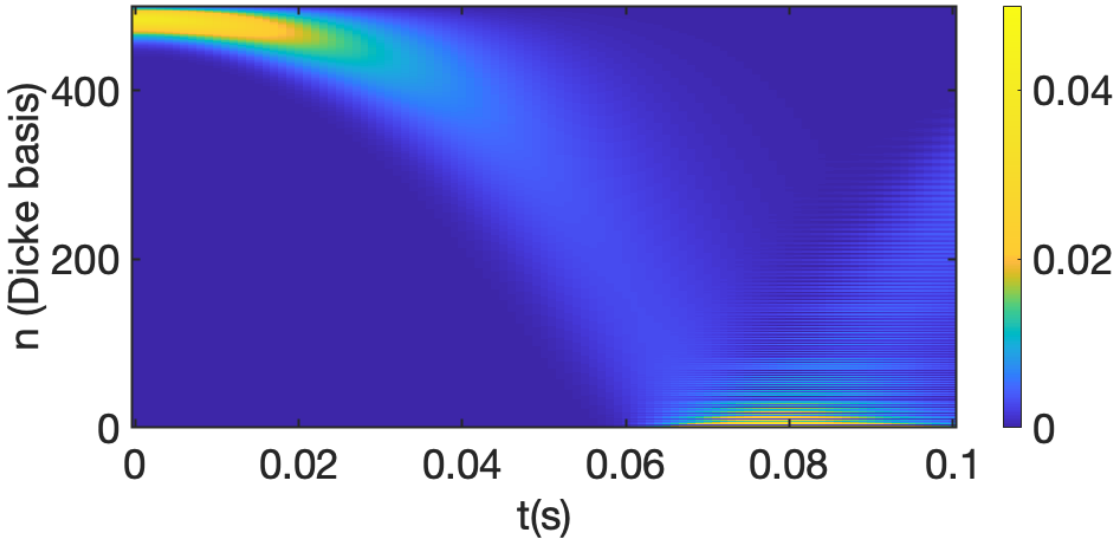

Figure 6.9: The excitation spectrum of the $q = 1|c|$ evolution in the Dicke basis.

Using the semi-classical simulation, the max anti-squeezed state is visualized in the Bloch sphere.

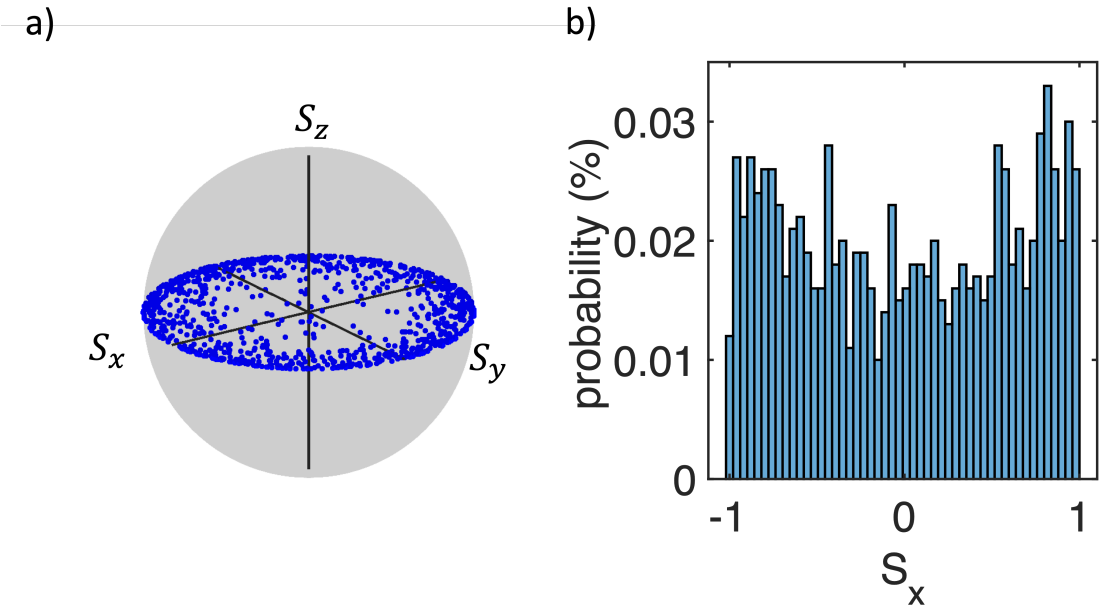

Figure 6.10: (a) Ensemble points simulated with the semi-classical method are plotted in the Bloch sphere. (b) Histogram of the state in the S_x variable which can be measured in an experiment.

Similar to the double quench used for the squeezed ground state, a second quench can also be applied to the Dicke like state to generate time-stationary anti-squeezed $q(t) = +\infty\chi_{(-\infty,0)}(t) + q_i\chi_{(0,T)}(t) + q_f\chi_{(T,+\infty)}(t)$. A second quench to $q_f = 0|c|$ at the max anti-squeezing point is simulated in Figure 6.11.

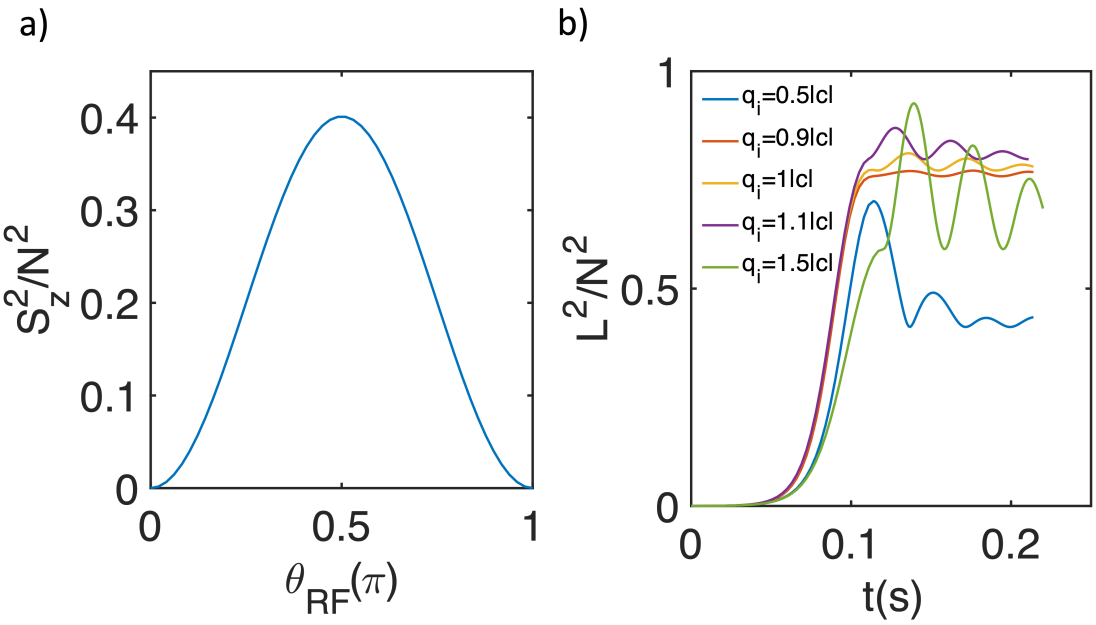

Figure 6.11: (a) S_z^2 noise measurement with RF rotation angle θ_{RF}. (b) $q_i = 0.9|c|$ gives the best time-stationary anti-squeezed state.

6.4 Gap opening induced by the finite system size effect

As shown in the Figure 4.13, the finite system size will lead to the gap opening effect. This effect is essential for going across the quantum phase transition adiabatically within a relatively short time against the lifetime of the system, which has been studied in ^{23}Na [94]. For ^{87} Rb, the entire region can be divided into three. In the regime, $q = +\infty \to 3|c|$, the nonadiabatic shortcut from the squeezed ground state can be applied disregarding the atom number change. Similarly, a nonadiabatic shortcut $q(t) = 1|c|\chi_{(0)}(t) + 0.5|c|\chi_{(0,T)}(t) + 0|c|\chi_{(T,+\infty)}(t)$ utilizes the coherent oscillation in the regime $q = 1|c| \to 0|c|$. In the regime $q = 3|c| \to 1|c|$, the energy gap plays a significant role and total ramp time varies as the

atom number changes.

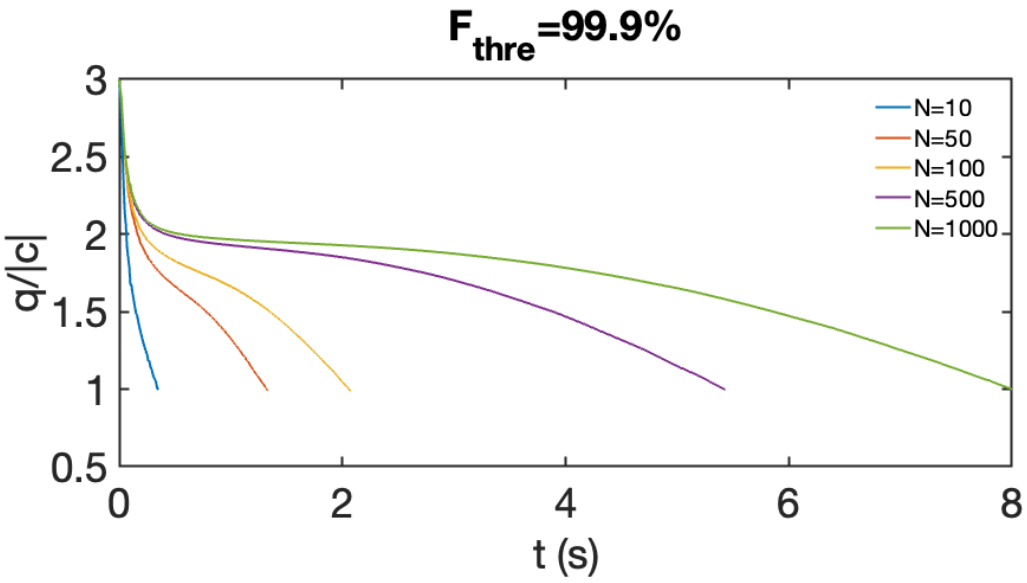

Figure 6.12: Piecewise ramp optimization for a threshold fidelity $F_{thre} = 99.9\%$. Each optimization step asks for the fastest speed of a linear ramp to achieve the instantaneous ground state fidelity above F_{thre}. The time required to finish the ramp is shortened with a smaller atom number.

There exists a universal relationship for the numerical optimized ramp sequence, all sequences overlapped when plotting q versus $t\min(\Delta)^2$. Here $\min(\Delta)^2$ is the minimum energy gap (at the quantum phase transition) between the ground state and the first excited state. An analytic explanation can be derived based on the Landau-Zener theory [104]. The Landau-Zener parameter is defined as

$$LZ := \frac{|v|}{\min(\Delta)^2},$$

which determines the excitation probability of a two-level system across the phase transition. $dt = d\Delta/(LZ\min(\Delta)^2)$ because $v = d\Delta/dt$. As a result, the total ramp time

$$T = \frac{1}{LZ\min(\Delta)^2}(\Delta_{ini} - \Delta_{fin})$$

can be estimated based on the excitation probability and the minimum energy gap because the initial and final energy gap is the same. From the above equation, $T \min(\Delta)^2$ should be a constant for the same fidelity of the ground state, which agrees with Figure 6.13.

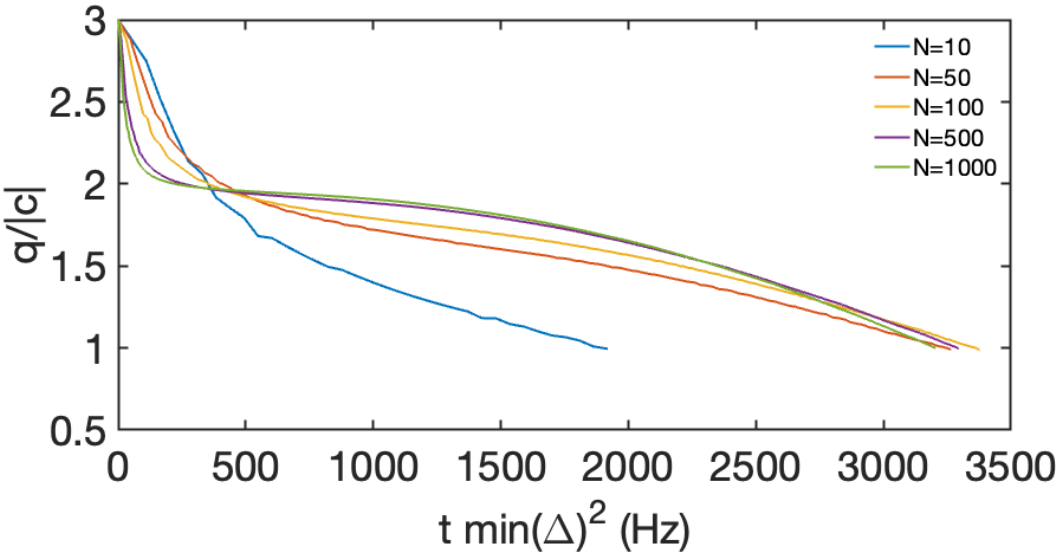

Figure 6.13: All traces overlap with each other when plotting q versus $t \min(\Delta)^2$. This is the universal relationship for the numerically optimized ramp.

If the final state generated isn't 100% fidelity, the oscillation of ρ_0 can be used to measure the energy gap and the fidelity. In Figure 6.14, the oscillation shows great agreement with the energy gap.

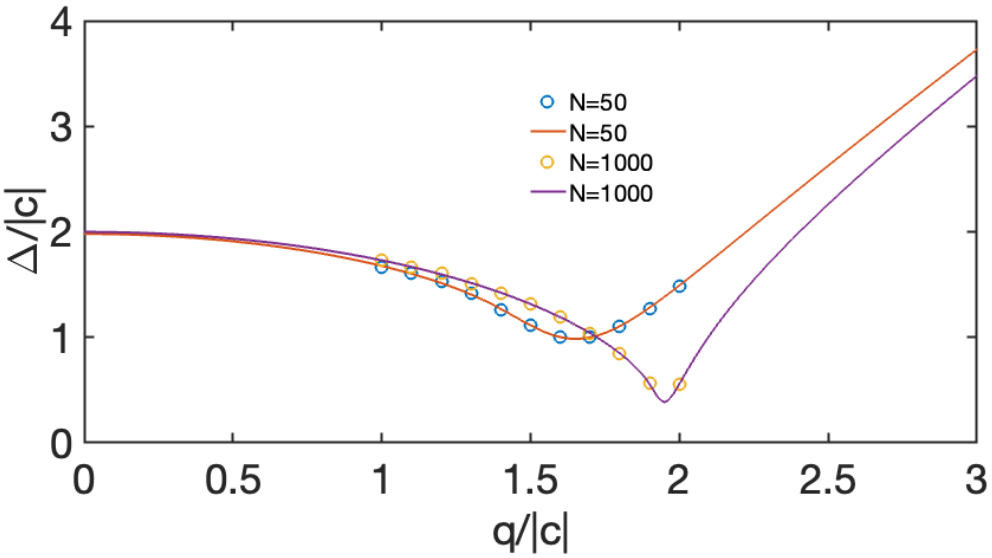

Figure 6.14: The energy gap is measured by detecting the ρ_0 oscillation frequency after holding the state at the target q. The circles are the measured oscillation frequency (converted into energy) and the solid line is the numerically calculated gap.

The oscillation amplitude $\Delta\rho_0$ can be analytically derived from the perturbation theory. Assuming the excitation is only in the first excited state $|\psi_1\rangle$, the final wave function can be expressed as $|\psi\rangle = \sqrt{1-p_e}|\psi_0\rangle + \sqrt{p_e}|\psi_1\rangle$. Consequently,

$$\Delta\rho_0 = 2\sqrt{p_e(1-p_e)}\langle\psi_0|\rho_0|\psi_1\rangle = 2\sqrt{p_e(1-p_e)}\sqrt{\frac{\Delta}{8|c|N}},$$

which can be used to estimate the fidelity of the ground state.

CHAPTER 7

OTHER EXPERIMENTAL PROJECTS

7.1 Mini MOT

This is a project done by collaborating with Thomas Dellaert and Bharath Hebbe Madhusudhana. The purpose is to create a miniaturized MOT setup that is portable due to the size and small laser power required. This setup can also be used to test the laser locking quality.

A pair of anti-Helmholtz coils with 20 windings each works as the MOT coil. The current required to generate the gradient is 8.4 A. The vacuum chamber is sealed by pinching off a cooper tube instead of a valve. An ion pump is included in the system to provide an ultrahigh vacuum.

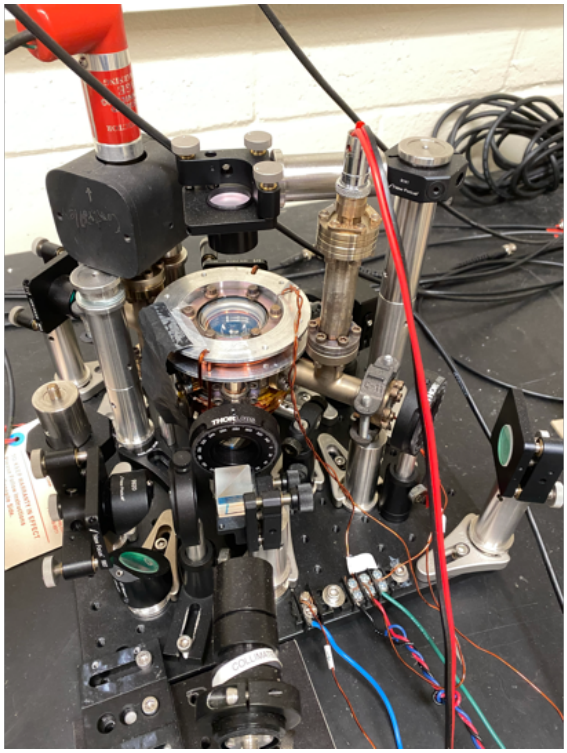

Figure 7.1: Mini MOT vacuum chamber setup.

One ECDL is used to work for both cycling and repump transitions. The laser beam is expanded into a 1.5 cm diameter. A minimum of 2.3 mW in cycling transition and 8.2 μW in repump transition is needed for generating MOT. The laser is locked on the cycling transition. The repump transition is created by using an electro-optic modulator (EOM) with the model Jenoptik 635. The EOM is modulated by phase with a 6777 MHz RF source with an amplifier (ZVE-8G 30dBm). The insertion loss of EOM is -6 dB which means the output beam power is 25% of the input beam. To avoid the interfering problem between the carrier frequency of EOM and the cycling transition when input with a single fiber, an extra AOM is added. The 0th order of AOM is used as the cycling transition beam.

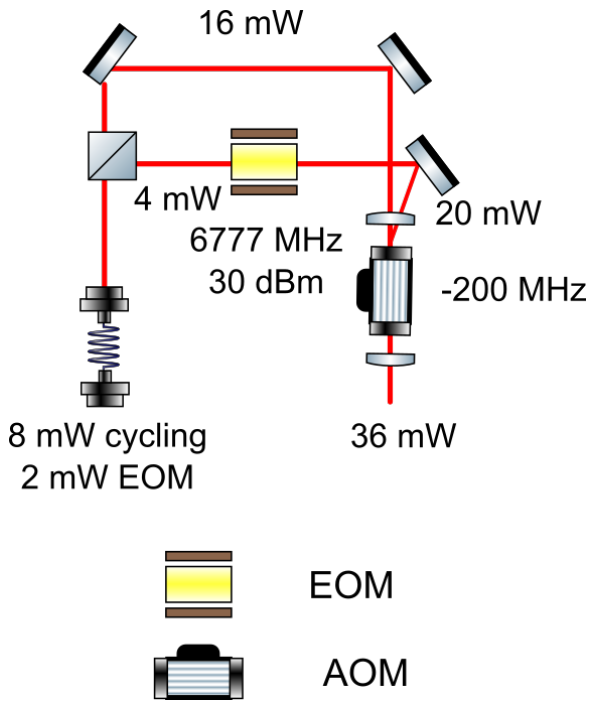

Figure 7.2: Single ECDL setup with EOM generates both the cycling and repump transition frequency.

7.2 EOM laser

This is a project done by collaborating with Mikai Hulse. One major problem of ECDL laser locking is its narrow tunable range. AOMs can only provide 100 MHz range compared

to the locked point which is typically an absorption feature of ^{87}Rb. One way to further improve the tunable range to GHz is by replacing AOMs with EOMs.

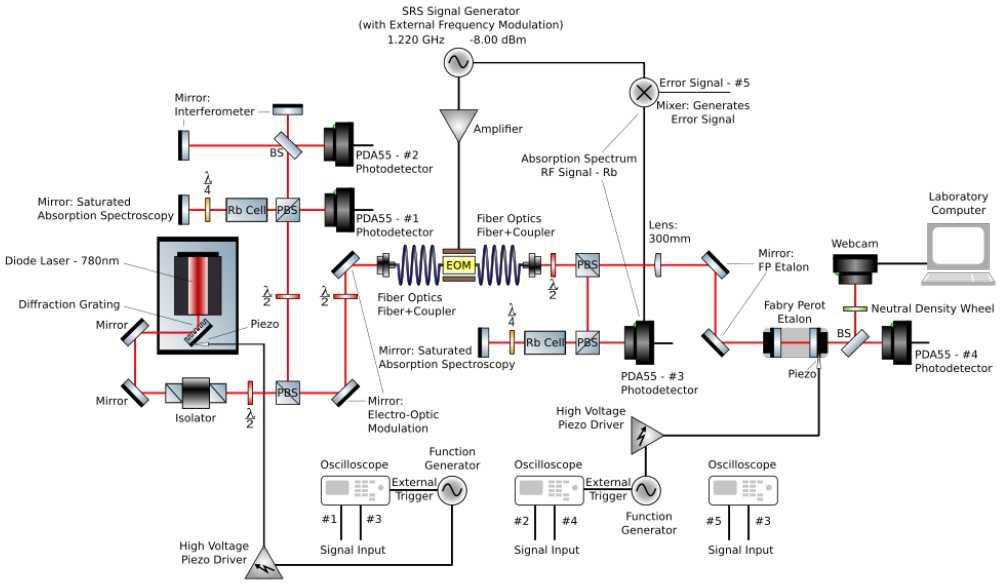

Figure 7.3: Setup for using the laser after the EOM to perform a satspec. The satspec before the EOM is also used to show the comparison.

By applying different RF frequencies, the satspec after the EOM shows a direct difference compared to the satspec before the EOM.

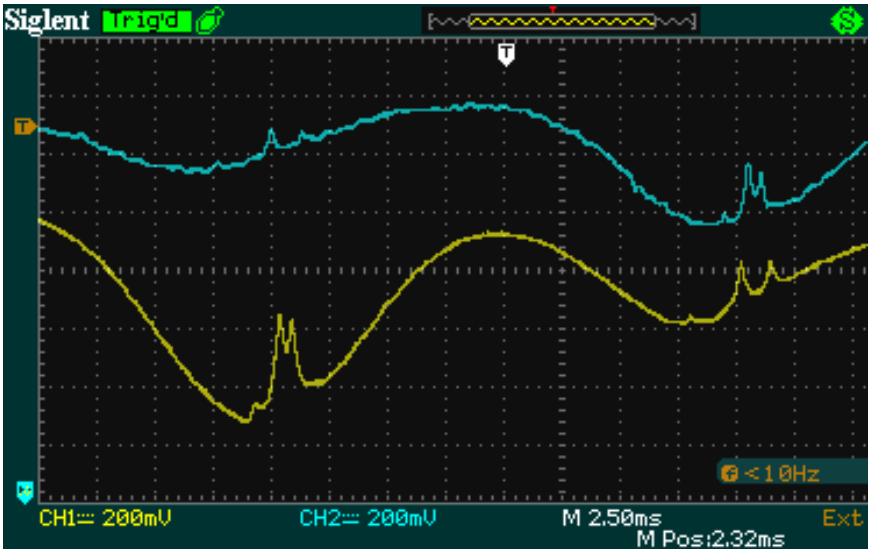

Figure 7.4: Satspec with applied modulation 1.22 GHz. (Yellow) Reference satspec setup. (Blue) Post EOM setspec setup.

To characterize the sideband and carrier power ratio, A Fabry–Pérot cavity Figure 3.9 is used. By measuring the resonance peak height on the oscilloscope, the relative power is measured as a function of import modulating power.

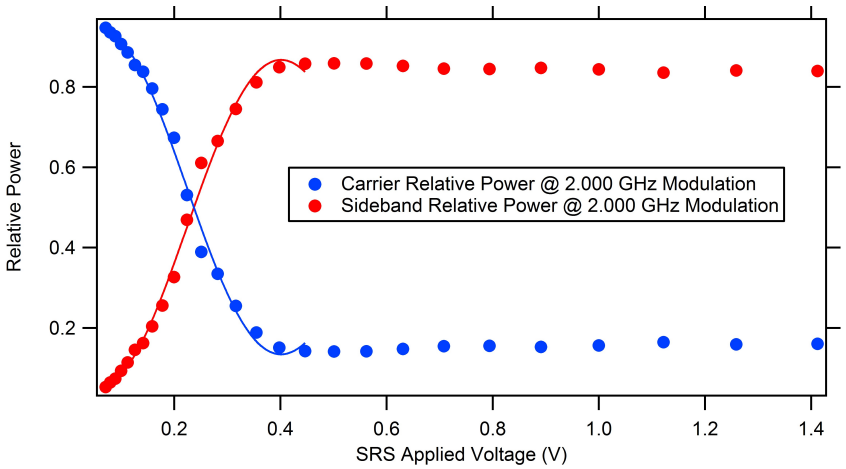

Figure 7.5: The relative power of the sideband and the carrier frequency at 2 GHz modulation frequency

7.3 Double MOT

This is a project done by collaborating with Maryrose Barrios. The purpose of this project is to use the 2D MOT as a cold atom source instead of a dispenser. This will enable a higher vacuum and thus a longer lifetime for the condensate. The 3D MOT chamber is a glass cell, as a result, the MOT coil doesn't need to be water-cooled due to the close spacing between the MOT coils. Furthermore, the all-glass cell lead to small scattering from the imaging beams.

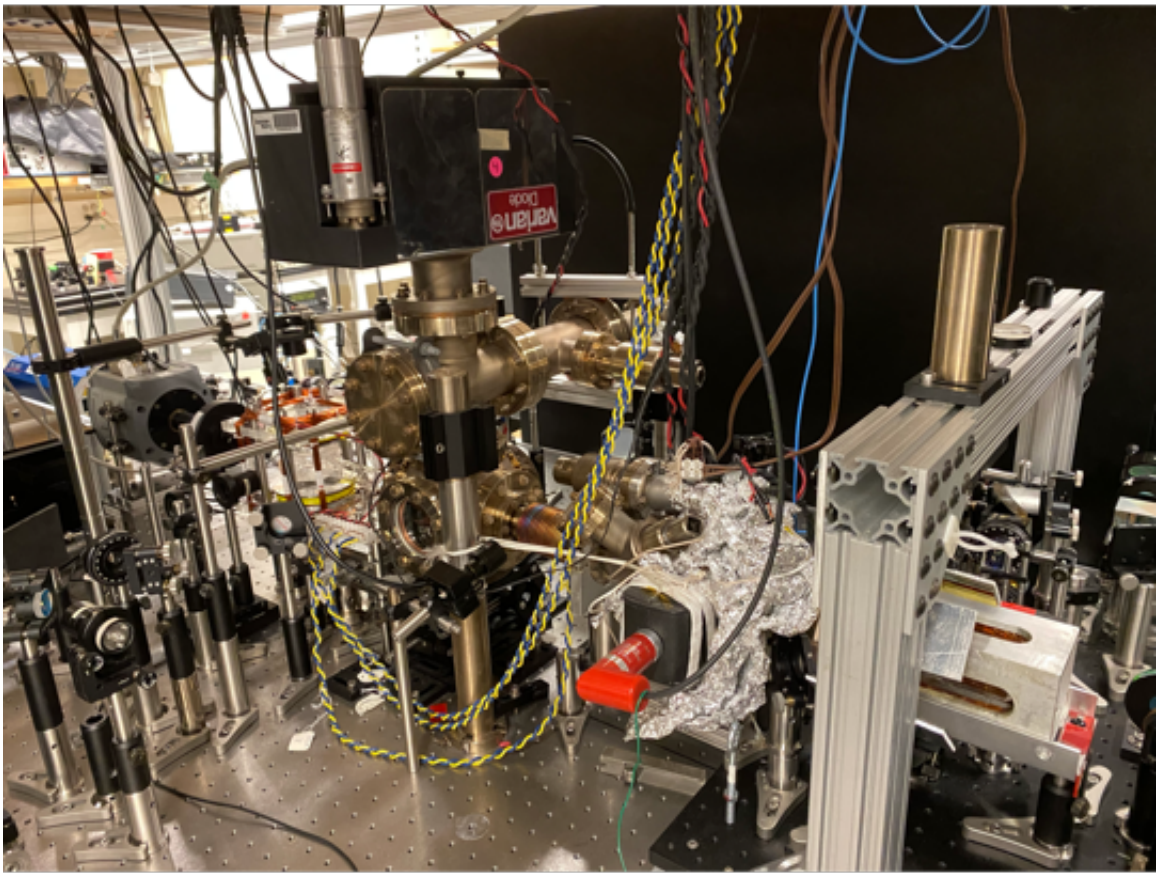

Figure 7.6: Double MOT vacuum chamber setup.

The 2D MOT takes the most laser power due to the expanded cigar beam shape. A push beam sends atoms through a small hole to the 3D side, where the slow atom source is recaptured by the MOT beams. An atom number of 6×10^9 can be loaded within 10.5 s

and the lifetime of MOT is about 20 s.

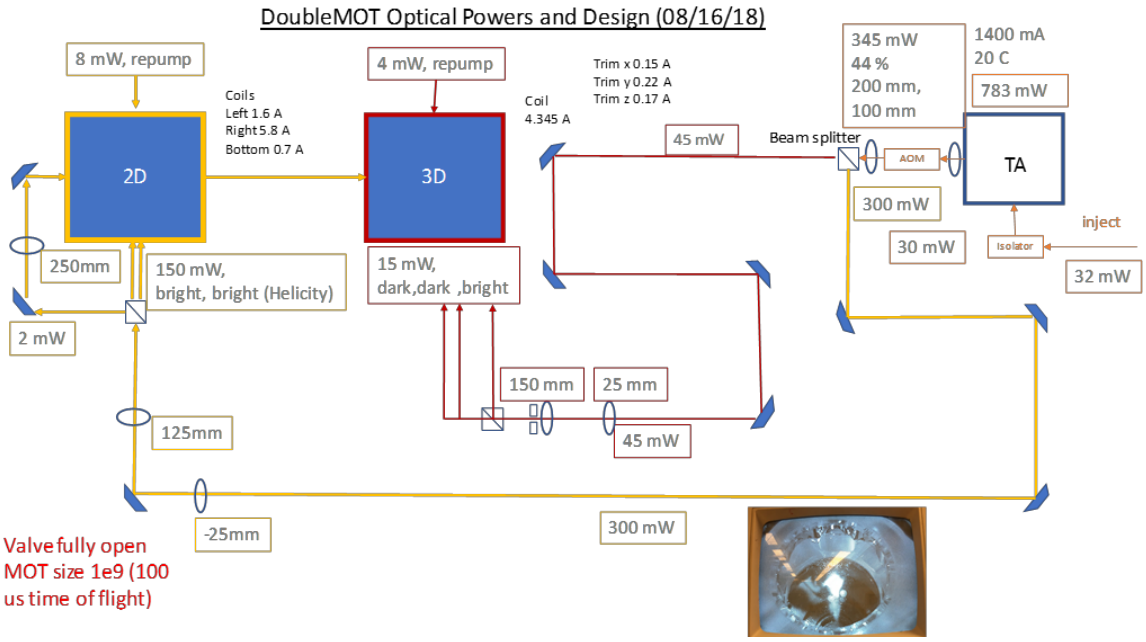

Figure 7.7: Double MOT laser setup.

Another advantage of using the all-glass cell is that the dipole traps optics are placed outside the chamber. A YAG fiber laser with $\lambda = 1064$ nm (seed laser YLD-0.01-1064-LP-SF + amplifier YAR-20k-1064-LP-SF) is used to load the atom from the Dark MOT stage. An 8.5 W (15 W out of fiber) of $\lambda = 1064$ nm is focused by a 100 mm lens into the chamber. About 5×10^5 atoms are trapped inside the dipole trap. The alignment is helped by using a cycling beam to blow atom away in the dark MOT center and then overlap the $\lambda = 1064$ nm with the cycling beam.

To sum up, this project is a successful trial for going to more complicated setup with further improvement. The problem still needs to be conquered is the instability of the 3D MOT, which comes from the long trajectory under gravity between the 2D MOT to 3D MOT. A shorter distance will help. Also, the TA will be better used by having its free space coupled by the slave laser instead of after the fiber coupling.

7.4 Antenna with circularly-polarized microwaves

This is a project done by collaborating with Matthew Boguslawski. This project aims to use the circularly polarized microwave to apply a gate that does not care about the frequency degeneracy of $\pm\Delta$ transition. In the actual experiment, the antenna used is a spiral antenna due to its simplicity. Here another antenna with better circular polarization is demonstrated.

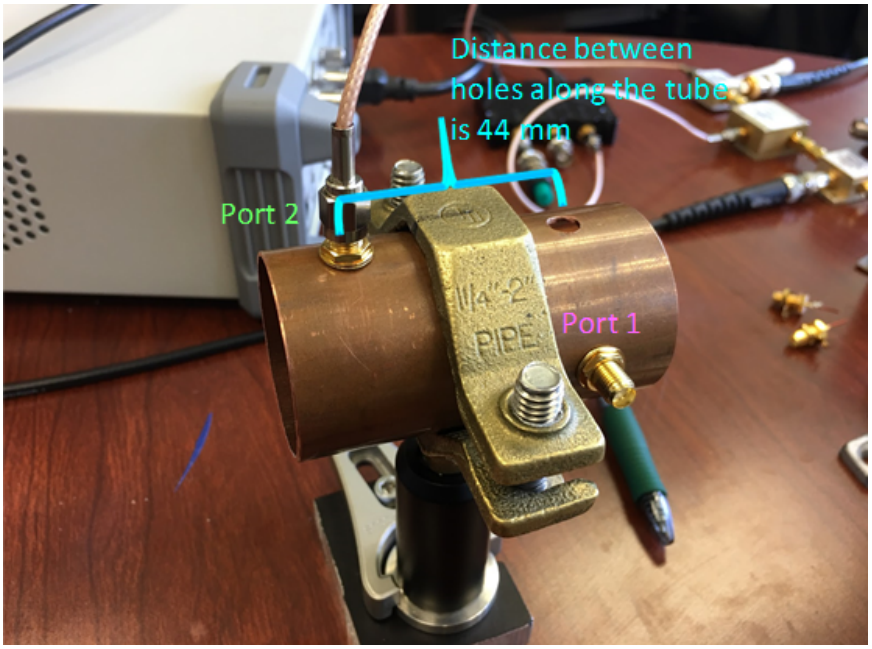

Figure 7.8: Two dipole antennas are constructed to be orthogonal to each other. Two antennas are displaced along the axis direction so that there is no interference. The phase of microwaves entering each antenna is modulated by using a mixer.

The quality of linearly and circularly polarized microwaves is examined using a receiving linear polarized antenna and measuring the receiving power against the rotation angle. The measurement of Malus's law indicates good linear polarization (25 dB contrast) of each antenna while showing the 90° difference between antennas.

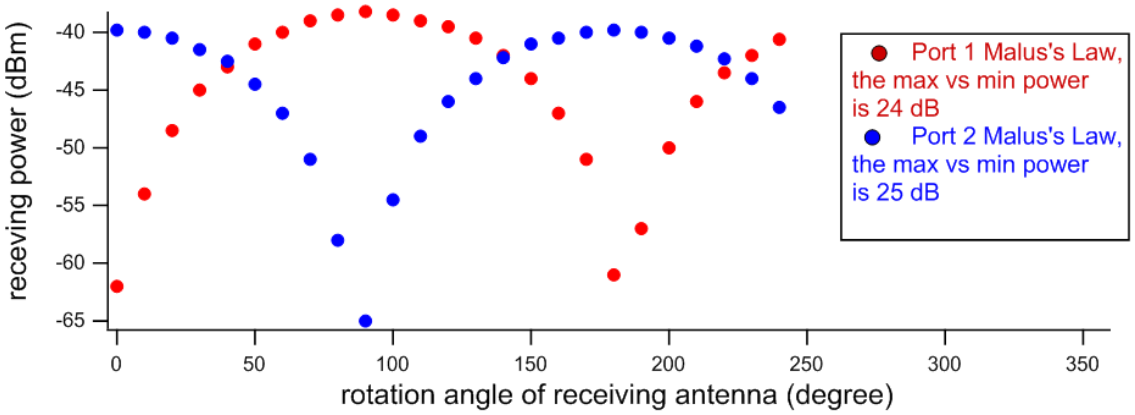

Figure 7.9: Individual antenna measurement shows Malus's law.

By changing the relative phase difference between the microwaves that input into the antenna, the maximum and minimum power received is balanced. The difference between the two power indicates how good is the circular polarization.

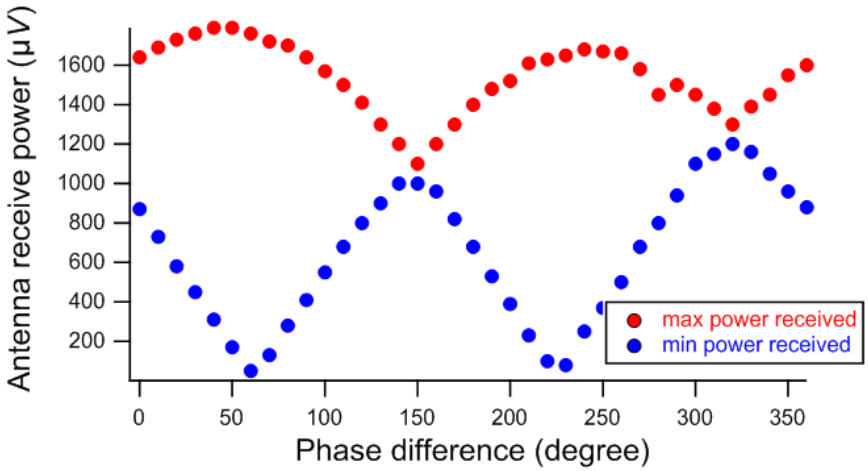

Figure 7.10: The minimum axial ratio between the max and min power is 0.4 dB which is better than the commercial linear-to-circular polarizer. The opposite handedness of circular polarization can be generated by shifting the phase of $180°$.

7.5 DBR laser

This is a project done by collaborating with Julia Cohen and Tetsuro Ishida. This project aims to replace the ECDL laser with the distributed Bragg reflector (DBR) laser to achieve better thermal stability, a larger free spectrum range, and a simpler laser locking method

with a large tunable range. The DBR laser (Photodigm ph780DBR Mercury package) has a passive grating controlled by the current and the temperature. The current and the temperature controller are from Vescent (D2-105). The temperature can be thus stabilized to ± 25 μK at the 1 s scale.

Table 7.1: A beam waist measurement of the DBR laser. The astigmatism is fixed by the cylindrical telescope. The aspherical collimation is optimized by adjusting the Y waist close to the near-distance result. The cylindrical telescope is adjusted to have the smallest X waist.

	X waist (μm)	Y waist (μm)
Near distance (after isolator)	401.46	1485.4
Far distance 1m for below measurement		
Aspherical collimation	1098.4	1150
1:1 50mm cylindrical telescope	615.28	1230
After anamorphic prism	594.41	598.3

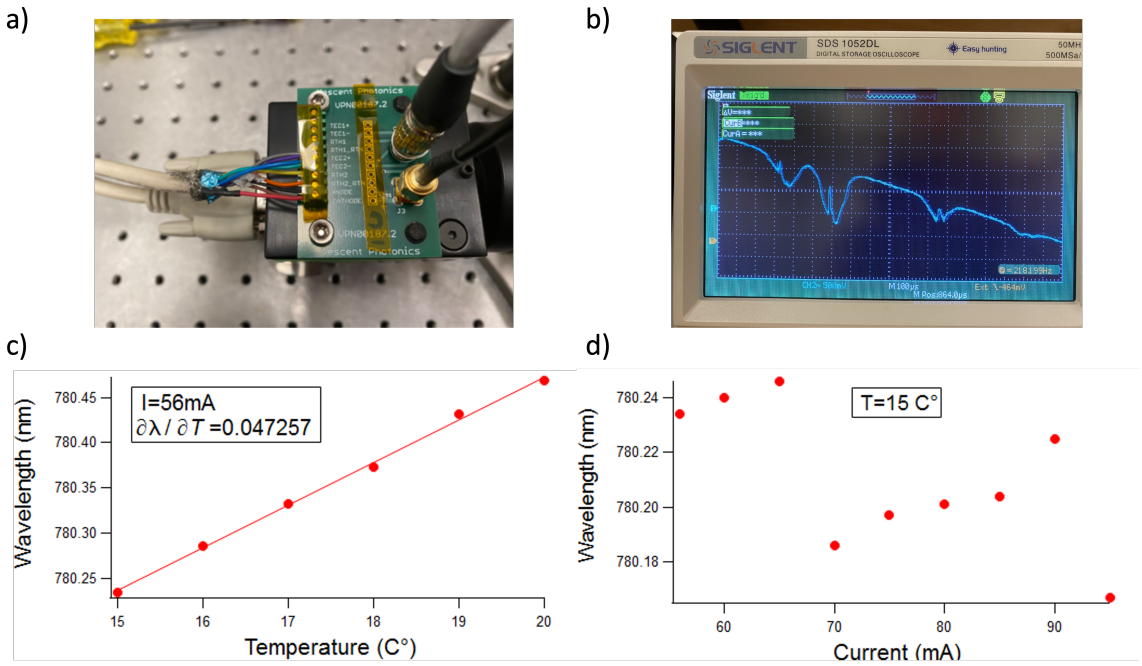

Figure 7.11: (a) The case of the current controller needs to be connected to the ground of the laser to avoid the ground loop. (b) The DBR laser has a free spectrum range of 20 GHz without the mode hop. All ^{87}Rb and ^{85}Rb features can be shown at the same time. (c) Wavelength as a function of temperature. (d) Wavelength as a function of current.

7.5.1 sub-Doppler DAVLL

To further improve the simplicity of the error signal generation, we switch from the FM method to the dichroic atomic vapor laser lock (DAVLL) method. A sub-Doppler DAVLL [105, 106] is applied to generate the error signal at a Doppler-free satspec. This method requires about 10 G along the Rb cell direction which is generated by a solenoid. The magnetic field shifts the resonance of $\sigma_{\pm}$ transition by $2\mu_B g_F B_z/h$ and the subtraction between the $\sigma_{\pm}$ signal gives the effective first-order derivatives.

The lock quality is estimated from the noise on the error signal. Two DBR lasers are locked to 3,1 crossover and 3,2 crossover accordingly, the bandwidth of DBR1=1.5 MHz and DBR2= 1.5 MHz. As a result, the bandwidth of the heterodyne signal has FWHM=$\sqrt{1.5^2 \cdot 2} = 2.1$ MHz agrees with the 2 MHz measured data.

7.5.2 DAVLL: Permanent magnet

To generate an error signal with a large tunable range (1 GHz), a DAVLL locking method is needed. This method does not require Doppler-free satspec and requires a magnetic field of about 100 G. A solenoid is not a great tool to generate such a strong field due to the fact of too many windings and the heat generated affecting the Rb cell temperature. To solve this problem, permanent magnets replacement is applied. Here are some permanent magnet configurations that are used.

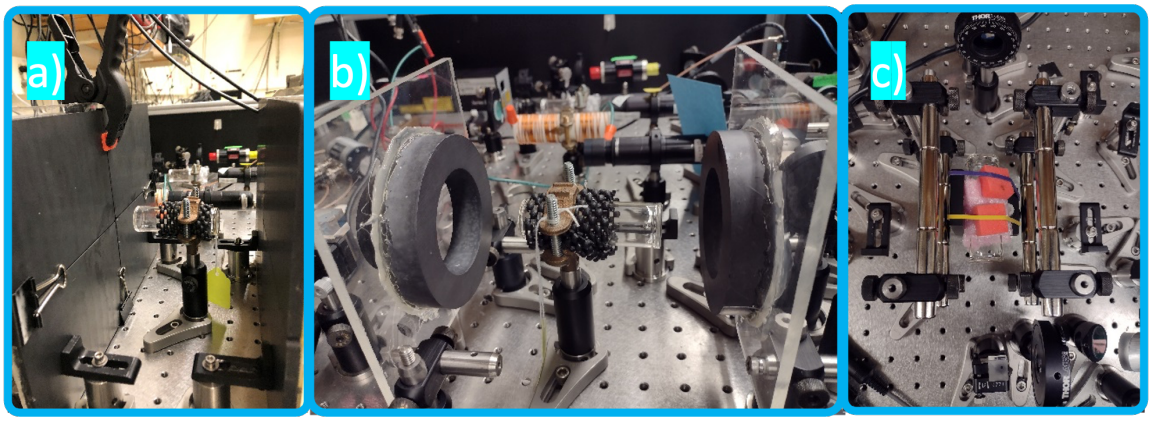

Figure 7.12: (a) A pair of ceramic plate magnets with a small hole in the center. Each plate is an attachment of 4 smaller plates (4×6") (b) A pair of ceramic ring magnets (100 mm outer diameter, 60 mm inner diameter, 20 mm thickness). (c) Four NdFeB magnets rod ($1/2$" diameter, 6" length). Each rod is an attachment of three cylinder magnets (2" length). From the center axis to the center of the rod is 2.088".

That configuration is found by performing the analytic calculations and numerical simulations. The cylindrical magnets along the center of the axial z direction have a field:

$$B_z = \frac{B_r}{2}\left(\frac{L+Z}{\sqrt{R^2+(L+Z)^2}} - \frac{Z}{\sqrt{R^2+Z^2}}\right),$$

where B_r is the flux density (Ceramic 5 = 3950 and NdFeB 35 = 12300), L is the thickness, R is the radius, and Z is the distance from the surface. It is very similar to a pair of Helmholtz coils where $\partial B_z/\partial z = 0$ happens at $R = D$, where D is the distance between the magnets. As a result, the plate magnets are chosen to be $8 \times 12 \times 1/4$" with $D = 5.7$".

The ring magnets can be calculated with the equation

$$B(z) = \frac{Br}{2}\left[\left(\frac{Z+L}{\sqrt{(Z+L)^2+R_1^2}} - \frac{Z}{\sqrt{Z^2+R_1^2}}\right) - \left(\frac{Z+L}{\sqrt{(Z+L)^2+R_2^2}} - \frac{Z}{\sqrt{Z^2+R_2^2}}\right)\right],$$

where R_1 is the outer radius and R_2 is the inner radius. There are not a lot of commercial options for ring magnets with a large radius, so we use the available options and optimized the distance ($D = 2.825$") to minimize the gradient.

The four-rod configuration is directly simulated using the method in [107]. This configuration turns out to be most compact and easy to be mounted with optics mounting hardware. The measurement of all three configurations shows great agreement with the theoretical curves.

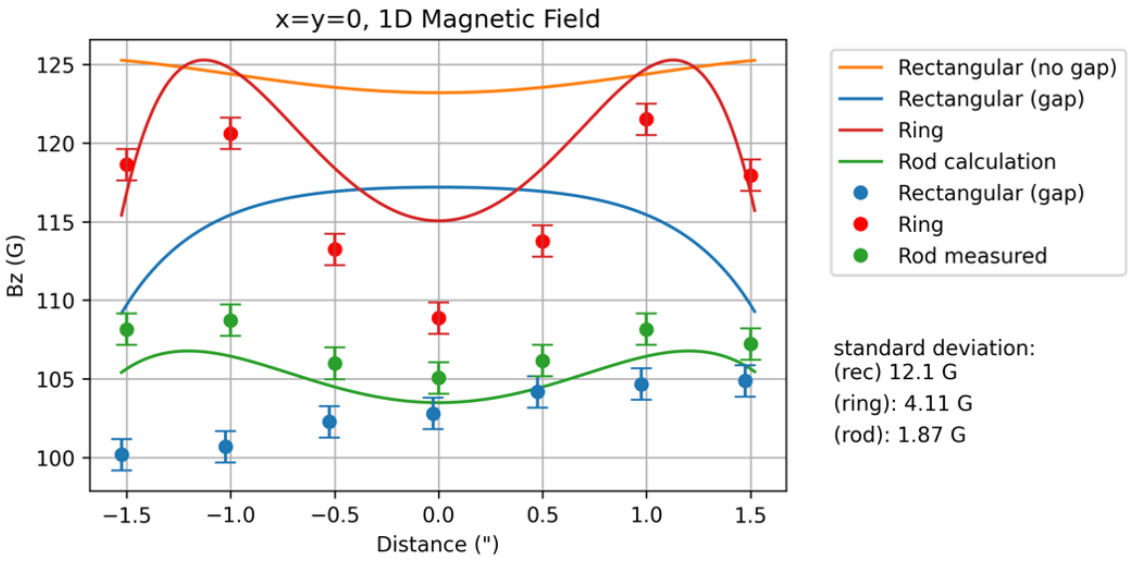

Figure 7.13: Magnetic field measurement along the center axis of different configurations. The solid curves are from the theory while the circles are measured with the Hall effect sensor.

Using the above configurations, the DVALL method generates a stable error signal that can be used to lock a laser with a large tunable range.

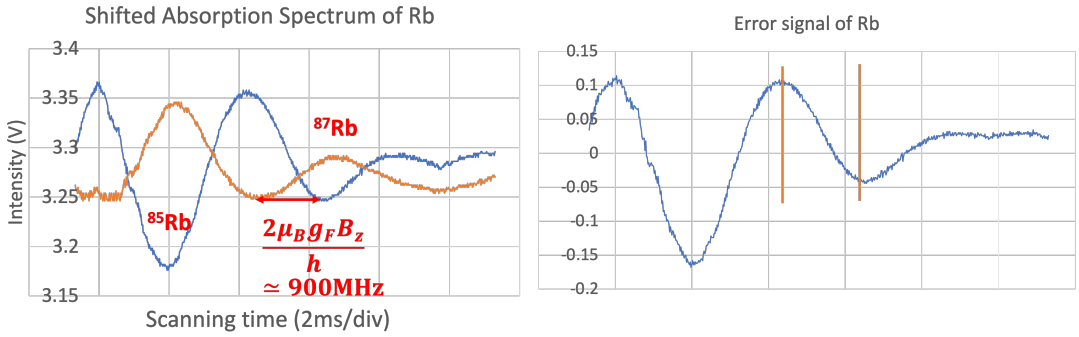

Figure 7.14: The DVALL method generates a splitting of $\sigma_{\pm}$ signal by 900 MHz. The change of the locking voltage to the error signal can now span the range of GHz.

7.6 New chamber

This project aims to improve the current vacuum setup to achieve a longer lifetime of BECs and a simultaneous imaging system with lower background noise. The setup is designed to have a minimum change to the current system.

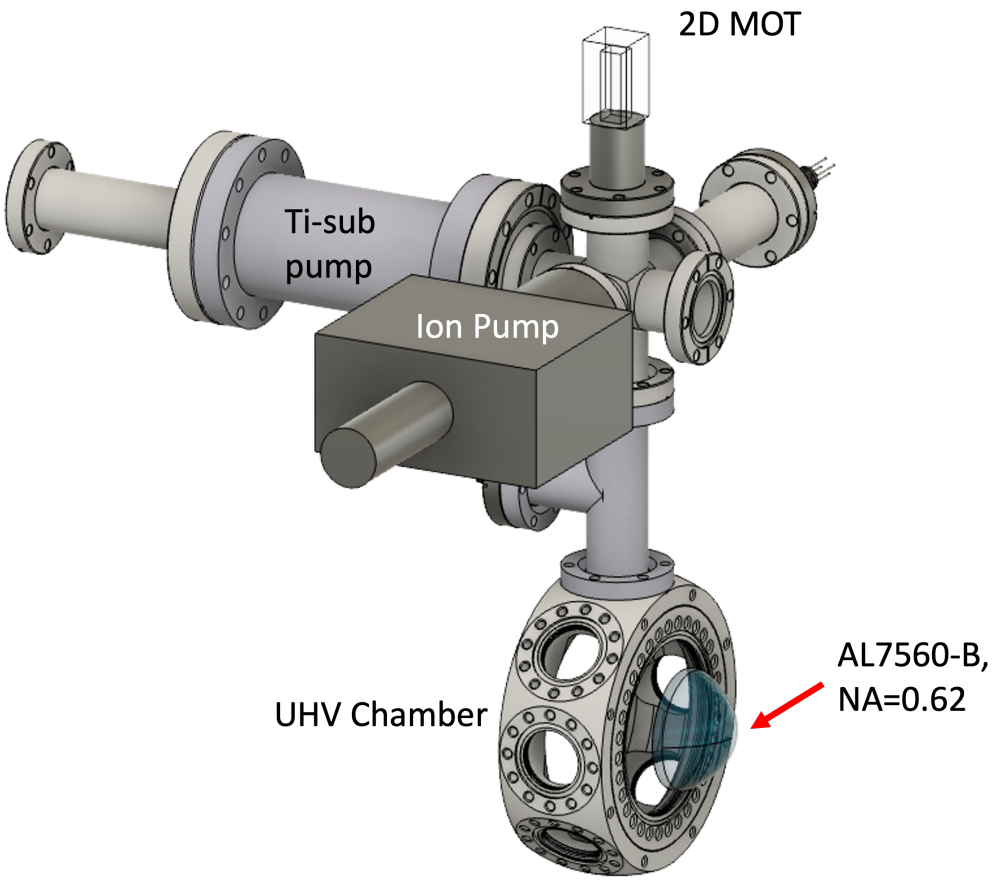

Figure 7.15: A 2D MOT setup is added as the slow atom source. This will improve the vacuum in the 3D MOT chamber. The 2D MOT is installed in the vertical direction to avoid the gravity curved trajectory of the atomic beam. The imaging lens inside the chamber can work with its full NA due to the cloud falling along the imaging axis. An extra high NA lens is installed to utilize the 6" window. Due to the 75 mm diameter of the aspherical lens, the TOF will not lead the cloud far from the imaging axis thus leading to less imaging distortion.

CHAPTER 8

OUTLOOK

In this thesis, we have been focused very deep into a spinor Bose-Einstein condensate within $m = 0$ subspace and investigated squeezed ground states. This is started with a question about how we manipulate the quantum system and achieve the target state, Hamiltonian, etc. to realize purposes such as metrology, simulation, and computation. There are limited options of interactions that nature provides us with. However, humans are not only trying to study nature but also using the knowledge we learned to further construct possible systems. In this chapter, we will look at the possible future direction from a broader perspective.

8.1 Experimental techniques

In this thesis, we are using the existing tools to make the experiment work. Nevertheless, there are plenty of places that can be further improved. The $\lambda = 850$ nm laser that is used for the cross trap configuration can be replaced with a further detuned wavelength (for instance, $\lambda = 1064$ nm) to achieve a lower photon scattering rate and a stabler trap alignment. The vacuum quality and the loading time can be further improved with a 2D MOT slow atom source. The number of lasers can be further reduced with DBR lasers. The laser power can be actively feedback and stabilized. The trim coils can be designed to satisfy the Helmholtz conditions to minimize the possible gradient. The IGBT can be replaced with metal–oxide–semiconductor field-effect transistor (MOSFET) to avoid the large induction induced current while the SG and MOT coils can be powered with the same power supply. The imaging method can be further improved by introducing the third aperture to apply the three-beam imaging method [47]. The fast laser on/off switching can be done with a better method (such as motorized laser power attenuators) without losing

a fair amount of power through AOMs. The control sequence can be optimized with non-even sampling rates.

8.2 Research directions

The reason that we limit our study within the $m = 0$ subspace is that the initial state $|0, N, 0\rangle$ can be generated robustly by the purification process. To further explore interesting physics outside this subspace, a robust protocol to prepare a different initial state that is accurate up to the quantum noise level needs to be designed. The experiments related to the $m \neq 0$ subspace are spin-1 state noise tomography and gap opening due to the non-zero magnetization.

Another direction that can be studied is to flip the sign of the interactions in the spinor condensate. q can be flipped with a microwave dressing. c can be flipped by transferring atoms into $F = 2$ level because it is anti-ferromagnetic. At the same time, $F = 2$ level is more accurately described by the spin-2 dynamics. Theories and experiments are less studied which leaves a lot of open questions: What is the commutation relationship of the 25 operators space? What will be qualitatively different between the spin-1 and spin-2 spin-mixing dynamics? Can the control of q and c together engineer Hamiltonian to create time-reversal dynamics or two-axis squeezing?

Last but not least, there are still some hard problems to be tackled even within the $m = 0$ subspace. The Dicke state is still a state hard to be generated due to the phase transitions. The potential solution is to find a shortcut for generating such states such as non-adiabatic evolution or deterministic excitation to a highly excited state at the polar phase. In an ideal world, we should be able to generate any eigenstate of the many-body Hamiltonian but the truth is we are still far away from this goal. This means a lot of further studies can be conducted in the future.

REFERENCES

[1] A. Einstein, *Quantentheorie des einatomigen idealen Gases*, ser. Sitzungsberichte der Preussischen Akademie der Wissenschaften. Physikalisch-mathematische Klasse bk. 2. Verlag d. Akad. d. Wiss., 1925.

[2] Bose, "Plancks gesetz und lichtquantenhypothese," *Zeitschrift für Physik*, vol. 26, pp. 178–181, 1 1924.

[3] W. D. Phillips, "Nobel lecture: Laser cooling and trapping of neutral atoms," *Rev. Mod. Phys.*, vol. 70, pp. 721–741, 3 Jul. 1998.

[4] M. H. Anderson, J. R. Ensher, M. R. Matthews, C. E. Wieman, and E. A. Cornell, "Observation of bose-einstein condensation in a dilute atomic vapor," *Science*, vol. 269, no. 5221, pp. 198–201, 1995.

[5] K. B. Davis, M. O. Mewes, M. R. Andrews, N. J. van Druten, D. S. Durfee, D. M. Kurn, and W. Ketterle, "Bose-einstein condensation in a gas of sodium atoms," *Phys. Rev. Lett.*, vol. 75, pp. 3969–3973, 22 Nov. 1995.

[6] D. M. Stamper-Kurn, M. R. Andrews, A. P. Chikkatur, S. Inouye, H.-J. Miesner, J. Stenger, and W. Ketterle, "Optical confinement of a bose-einstein condensate," *Phys. Rev. Lett.*, vol. 80, pp. 2027–2030, 10 Mar. 1998.

[7] M. D. Barrett, J. A. Sauer, and M. S. Chapman, "All-optical formation of an atomic bose-einstein condensate," *Phys. Rev. Lett.*, vol. 87, p. 010 404, 1 Jun. 2001.

[8] M.-S. Chang, C. D. Hamley, M. D. Barrett, J. A. Sauer, K. M. Fortier, W. Zhang, L. You, and M. S. Chapman, "Observation of spinor dynamics in optically trapped 87rb bose-einstein condensates," *Phys. Rev. Lett.*, vol. 92, p. 140 403, 14 Apr. 2004.

[9] M.-S. Chang, Q. Qin, W. Zhang, L. You, and M. S. Chapman, "Coherent spinor dynamics in a spin-1 bose condensate," *Nature Physics*, vol. 1, pp. 111–116, 2 2005.

[10] E. M. Bookjans, C. D. Hamley, and M. S. Chapman, "Strong quantum spin correlations observed in atomic spin mixing," *Phys. Rev. Lett.*, vol. 107, p. 210 406, 21 Nov. 2011.

[11] C. D. Hamley, C. S. Gerving, T. M. Hoang, E. M. Bookjans, and M. S. Chapman, "Spin-nematic squeezed vacuum in a quantum gas," *Nature Physics*, vol. 8, no. 4, pp. 305–308, 2012.

[12] T. M. Hoang, M. Anquez, B. A. Robbins, X. Y. Yang, B. J. Land, C. D. Hamley, and M. S. Chapman, "Parametric excitation and squeezing in a many-body spinor condensate," *Nature Communications*, vol. 7, no. 1, p. 11 233, 2016.

[13] T. M. Hoang, H. M. Bharath, M. J. Boguslawski, M. Anquez, B. A. Robbins, and M. S. Chapman, "Adiabatic quenches and characterization of amplitude excitations in a continuous quantum phase transition," *Proceedings of the National Academy of Sciences*, vol. 113, no. 34, pp. 9475–9479, 2016.

[14] M. Anquez, B. A. Robbins, H. M. Bharath, M. Boguslawski, T. M. Hoang, and M. S. Chapman, "Quantum kibble-zurek mechanism in a spin-1 bose-einstein condensate," *Phys. Rev. Lett.*, vol. 116, p. 155 301, 15 Apr. 2016.

[15] T. M. Hoang, C. S. Gerving, B. J. Land, M. Anquez, C. D. Hamley, and M. S. Chapman, "Dynamic stabilization of a quantum many-body spin system," *Phys. Rev. Lett.*, vol. 111, p. 090 403, 9 Aug. 2013.

[16] H. M. Bharath, M. Boguslawski, M. Barrios, L. Xin, and M. S. Chapman, "Exploring non-abelian geometric phases in spin-1 ultracold atoms," *Phys. Rev. Lett.*, vol. 123, p. 173 202, 17 Oct. 2019.

[17] L. Xin, M. S. Chapman, and T. A. B. Kennedy, "Fast generation of time-stationary spin-1 squeezed states by nonadiabatic control," *PRX Quantum*, vol. 3, p. 010 328, 1 Feb. 2022.

[18] L. Xin, M. Barrios, J. T. Cohen, and M. S. Chapman, "Squeezed ground states in a spin-1 bose-einstein condensate," *arXiv.2202.12338*, 2022.

[19] E. P. Gross, "Structure of a quantized vortex in boson systems," *Nuovo Cimento*, vol. 20, pp. 454–477, Oct. 1960.

[20] L. P. PITAEVSKII, "Vortex lines in an imperfect bose gas," *Sov. Phys.-JETP*, vol. 13, no. 2, p. 451, 1961.

[21] Y. Kawaguchi and M. Ueda, "Spinor Bose-Einstein condensates," *Physics Reports*, vol. 520, pp. 253–381, 2012.

[22] D. A. Steck, *Rubidium 87 d line data*, 2001.

[23] W. Zhang, D. L. Zhou, M.-S. Chang, M. S. Chapman, and L. You, "Coherent spin mixing dynamics in a spin-1 atomic condensate," *Phys. Rev. A*, vol. 72, p. 013 602, 1 Jul. 2005.

[24] C. D. Hamley, "Spin-nematic squeezing in a spin-1 bose-einstein condensate," Ph.D. dissertation, 2012.

[25] W. Zurek, "Cosmological experiments in condensed matter systems," *Physics Reports*, vol. 276, no. 4, pp. 177–221, 1996.

[26] C. K. Law, H. Pu, and N. P. Bigelow, "Quantum spins mixing in spinor bose-einstein condensates," *Phys. Rev. Lett.*, vol. 81, pp. 5257–5261, 24 Dec. 1998.

[27] L.-N. Wu and L. You, "Using the ground state of an antiferromagnetic spin-1 atomic condensate for heisenberg-limited metrology," *Phys. Rev. A*, vol. 93, p. 033 608, 3 Mar. 2016.

[28] H. Strobel, W. Muessel, D. Linnemann, T. Zibold, D. B. Hume, L. Pezzè, A. Smerzi, and M. K. Oberthaler, "Fisher information and entanglement of non-gaussian spin states," *Science*, vol. 345, no. 6195, pp. 424–427, 2014.

[29] B. Lücke, J. Peise, G. Vitagliano, J. Arlt, L. Santos, G. Tóth, and C. Klempt, "Detecting multiparticle entanglement of dicke states," *Phys. Rev. Lett.*, vol. 112, p. 155 304, 15 Apr. 2014.

[30] Y.-Q. Zou, L.-N. Wu, Q. Liu, X.-Y. Luo, S.-F. Guo, J.-H. Cao, M. K. Tey, and L. You, "Beating the classical precision limit with spin-1 dicke states of more than 10,000 atoms," *Proceedings of the National Academy of Sciences*, vol. 115, no. 25, pp. 6381–6385, 2018.

[31] E. L. Raab, M. Prentiss, A. Cable, S. Chu, and D. E. Pritchard, "Trapping of neutral sodium atoms with radiation pressure," *Phys. Rev. Lett.*, vol. 59, pp. 2631–2634, 23 Dec. 1987.

[32] C. Monroe, W. Swann, H. Robinson, and C. Wieman, "Very cold trapped atoms in a vapor cell," *Phys. Rev. Lett.*, vol. 65, pp. 1571–1574, 13 Sep. 1990.

[33] S. D. Saliba, M. Junker, L. D. Turner, and R. E. Scholten, "Mode stability of external cavity diode lasers," *Appl. Opt.*, vol. 48, no. 35, pp. 6692–6700, Dec. 2009.

[34] T. M. Hoang, "Quantum control of a many-body system in a spin-1 bose-einstein condensate," Ph.D. dissertation, 2013.

[35] E. A. Donley, T. P. Heavner, F. Levi, M. O. Tataw, and S. R. Jefferts, "Double-pass acousto-optic modulator system," *Review of Scientific Instruments*, vol. 76, no. 6, p. 063 112, 2005.

[36] A. Perot and C. Fabry, "On the Application of Interference Phenomena to the Solution of Various Problems of Spectroscopy and Metrology," *apj*, vol. 9, p. 87, Feb. 1899.

[37] M. S. Chapman, *Optics lab manual*.

[38] A. A. Michelson and E. W. Morley, "On the relative motion of the earth and the luminiferous ether," *American Journal of Science*, vol. s3-34, no. 203, pp. 333–345, 1887.

[39] Z. Hu, "Quantum optics with cold atoms–nonlinear spectroscopy and road toward single-atom trap," Ph.D. dissertation, 1995.

[40] M.-S. Chang, "Coherent spin dynamics of a spin-1 bose-einstein condensate," Ph.D. dissertation, 2006.

[41] E. Bookjans, "Relative number squeezing in a spin-1 bose-einstein condensate," Ph.D. dissertation, 2010.

[42] L. Pezzè, A. Smerzi, M. K. Oberthaler, R. Schmied, and P. Treutlein, "Quantum metrology with nonclassical states of atomic ensembles," *Rev. Mod. Phys.*, vol. 90, p. 035 005, 3 Sep. 2018.

[43] J. Ma, X. Wang, C. Sun, and F. Nori, "Quantum spin squeezing," *Physics Reports*, vol. 509, no. 2, pp. 89 –165, 2011.

[44] M. Kitagawa and M. Ueda, "Squeezed spin states," *Phys. Rev. A*, vol. 47, pp. 5138–5143, 6 Jun. 1993.

[45] C. Gross, T. Zibold, E. Nicklas, J. Estève, and M. K. Oberthaler, "Nonlinear atom interferometer surpasses classical precision limit," *Nature*, vol. 464, no. 7292, pp. 1165–1169, 2010.

[46] W. Muessel, H. Strobel, D. Linnemann, T. Zibold, B. Juliá-Díaz, and M. K. Oberthaler, "Twist-and-turn spin squeezing in bose-einstein condensates," *Phys. Rev. A*, vol. 92, p. 023 603, 2 Aug. 2015.

[47] A. Qu, B. Evrard, J. Dalibard, and F. Gerbier, "Probing spin correlations in a bose-einstein condensate near the single-atom level," *Phys. Rev. Lett.*, vol. 125, p. 033 401, 3 Jul. 2020.

[48] Z. Zhang and L.-M. Duan, "Generation of massive entanglement through an adiabatic quantum phase transition in a spinor condensate," *Phys. Rev. Lett.*, vol. 111, p. 180 401, 18 Oct. 2013.

[49] X.-Y. Luo, Y.-Q. Zou, L.-N. Wu, Q. Liu, M.-F. Han, M. K. Tey, and L. You, "Deterministic entanglement generation from driving through quantum phase transitions," *Science*, vol. 355, no. 6325, pp. 620–623, 2017.

[50] H. Lee, P. Kok, and J. P. Dowling, "A quantum rosetta stone for interferometry," *Journal of Modern Optics*, vol. 49, no. 14-15, pp. 2325–2338, 2002.

[51] J. Javanainen and M. Y. Ivanov, "Splitting a trap containing a bose-einstein condensate: Atom number fluctuations," *Phys. Rev. A*, vol. 60, pp. 2351–2359, 3 Sep. 1999.

[52] B. Juliá-Díaz, T. Zibold, M. K. Oberthaler, M. Melé-Messeguer, J. Martorell, and A. Polls, "Dynamic generation of spin-squeezed states in bosonic josephson junctions," *Phys. Rev. A*, vol. 86, p. 023 615, 2 Aug. 2012.

[53] M. J. Steel and M. J. Collett, "Quantum state of two trapped bose-einstein condensates with a josephson coupling," *Phys. Rev. A*, vol. 57, pp. 2920–2930, 4 Apr. 1998.

[54] J. Ma and X. Wang, "Fisher information and spin squeezing in the lipkin-meshkov-glick model," *Phys. Rev. A*, vol. 80, p. 012 318, 1 Jul. 2009.

[55] E. Torrontegui, S. Ibáñez, S. Martínez-Garaot, M. Modugno, A. del Campo, D. Guéry-Odelin, A. Ruschhaupt, X. Chen, and J. G. Muga, "Chapter 2 - shortcuts to adiabaticity," in *Advances in Atomic, Molecular, and Optical Physics*, ser. Advances In Atomic, Molecular, and Optical Physics, E. Arimondo, P. R. Berman, and C. C. Lin, Eds., vol. 62, Academic Press, 2013, pp. 117–169.

[56] M. F. Riedel, P. Böhi, Y. Li, T. W. Hänsch, A. Sinatra, and P. Treutlein, "Atom-chip-based generation of entanglement for quantum metrology," *Nature*, vol. 464, no. 7292, pp. 1170–1173, 2010.

[57] R. E. Slusher, L. W. Hollberg, B. Yurke, J. C. Mertz, and J. F. Valley, "Observation of squeezed states generated by four-wave mixing in an optical cavity," *Phys. Rev. Lett.*, vol. 55, pp. 2409–2412, 22 Nov. 1985.

[58] D. M. Meekhof, C. Monroe, B. E. King, W. M. Itano, and D. J. Wineland, "Generation of nonclassical motional states of a trapped atom," *Phys. Rev. Lett.*, vol. 76, pp. 1796–1799, 11 Mar. 1996.

[59] P. Salamon, K. H. Hoffmann, Y. Rezek, and R. Kosloff, "Maximum work in minimum time from a conservative quantum system," *Phys. Chem. Chem. Phys.*, vol. 11, pp. 1027–1032, 7 2009.

[60] B Andresen, K. H. Hoffmann, J Nulton, A Tsirlin, and P Salamon, "Optimal control of the parametric oscillator," *European Journal of Physics*, vol. 32, no. 3, pp. 827–843, Apr. 2011.

[61] K. H. Hoffmann, B. Andresen, and P. Salamon, "Optimal control of a collection of parametric oscillators," *Phys. Rev. E*, vol. 87, p. 062 106, 6 Jun. 2013.

[62] J. Janszky and P. Adam, "Strong squeezing by repeated frequency jumps," *Phys. Rev. A*, vol. 46, pp. 6091–6092, 9 Nov. 1992.

[63] G. S. Agarwal and S. A. Kumar, "Exact quantum-statistical dynamics of an oscillator with time-dependent frequency and generation of nonclassical states," *Phys. Rev. Lett.*, vol. 67, pp. 3665–3668, 26 Dec. 1991.

[64] F. Galve and E. Lutz, "Nonequilibrium thermodynamic analysis of squeezing," *Phys. Rev. A*, vol. 79, p. 055 804, 5 May 2009.

[65] V. V. Dodonov and V. I. Man'ko, "Coherent states and the resonance of a quantum damped oscillator," *Phys. Rev. A*, vol. 20, pp. 550–560, 2 Aug. 1979.

[66] T. Kiss, J. Janszky, and P. Adam, "Time evolution of harmonic oscillators with time-dependent parameters: A step-function approximation," *Phys. Rev. A*, vol. 49, pp. 4935–4942, 6 Jun. 1994.

[67] R. Graham, "Squeezing and frequency changes in harmonic oscillations," *Journal of Modern Optics*, vol. 34, no. 6-7, pp. 873–879, 1987.

[68] H. P. Yuen, "Two-photon coherent states of the radiation field," *Phys. Rev. A*, vol. 13, pp. 2226–2243, 6 Jun. 1976.

[69] G. S. Agarwal, *Quantum Optics*. Cambridge University Press, 2012.

[70] C. Zener, "Non-adiabatic crossing of energy levels," *Proc. Roy. Soc. A*, vol. 33, no. 1929, pp. 696–702, 1932.

[71] W. H. Zurek, U. Dorner, and P. Zoller, "Dynamics of a quantum phase transition," *Phys. Rev. Lett.*, vol. 95, p. 105 701, 10 Sep. 2005.

[72] B. Damski and W. H. Zurek, "How to fix a broken symmetry: Quantum dynamics of symmetry restoration in a ferromagnetic bose–einstein condensate," *New Journal of Physics*, vol. 10, no. 4, p. 045 023, Apr. 2008.

[73] A. Altland, V. Gurarie, T. Kriecherbauer, and A. Polkovnikov, "Nonadiabaticity and large fluctuations in a many-particle landau-zener problem," *Phys. Rev. A*, vol. 79, p. 042 703, 4 Apr. 2009.

[74] A. Sala, D. L. Núñez, J. Martorell, L. De Sarlo, T. Zibold, F. Gerbier, A. Polls, and B. Juliá-Díaz, "Shortcut to adiabaticity in spinor condensates," *Phys. Rev. A*, vol. 94, p. 043 623, 4 Oct. 2016.

[75] W. H. Zurek, "Cosmological experiments in superfluid helium?" *Nature*, vol. 317, no. 6037, pp. 505–508, 1985.

[76] T. W. B. Kibble, "Some implications of a cosmological phase transition," *Physics Reports*, vol. 67, no. 1, pp. 183–199, 1980.

[77] L.-Y. Qiu, H.-Y. Liang, Y.-B. Yang, H.-X. Yang, T. Tian, Y. Xu, and L.-M. Duan, "Observation of generalized kibble-zurek mechanism across a first-order quantum phase transition in a spinor condensate," *Science Advances*, vol. 6, no. 21, 2020.

[78] L. Zhao, J. Jiang, T. Tang, M. Webb, and Y. Liu, "Dynamics in spinor condensates tuned by a microwave dressing field," *Phys. Rev. A*, vol. 89, p. 023 608, 2 Feb. 2014.

[79] T. Laudat, V. Dugrain, T. Mazzoni, M.-Z. Huang, C. L. G. Alzar, A. Sinatra, P. Rosenbusch, and J. Reichel, "Spontaneous spin squeezing in a rubidium BEC," *New Journal of Physics*, vol. 20, no. 7, p. 073 018, Jul. 2018.

[80] P. Solinas, P. Ribeiro, and R. Mosseri, "Dynamical properties across a quantum phase transition in the lipkin-meshkov-glick model," *Phys. Rev. A*, vol. 78, p. 052 329, 5 Nov. 2008.

[81] M. Xue, S. Yin, and L. You, "Universal driven critical dynamics across a quantum phase transition in ferromagnetic spinor atomic bose-einstein condensates," *Phys. Rev. A*, vol. 98, p. 013 619, 1 Jul. 2018.

[82] J. Estève, C. Gross, A. Weller, S. Giovanazzi, and M. K. Oberthaler, "Squeezing and entanglement in a bose–einstein condensate," *Nature*, vol. 455, no. 7217, pp. 1216–1219, 2008.

[83] T. Berrada, S. van Frank, R. Bücker, T. Schumm, J. F. Schaff, and J. Schmiedmayer, "Integrated mach–zehnder interferometer for bose–einstein condensates," *Nature Communications*, vol. 4, no. 1, p. 2077, 2013.

[84] E. Pedrozo-Peñafiel, S. Colombo, C. Shu, A. F. Adiyatullin, Z. Li, E. Mendez, B. Braverman, A. Kawasaki, D. Akamatsu, Y. Xiao, and V. Vuletić, "Entanglement on an optical atomic-clock transition," *Nature*, vol. 588, no. 7838, pp. 414–418, 2020.

[85] S. S. Szigeti, S. P. Nolan, J. D. Close, and S. A. Haine, "High-Precision Quantum-Enhanced Gravimetry with a Bose-Einstein Condensate," *Phys. Rev. Lett.*, vol. 125, no. 10, p. 100 402, Sep. 2020.

[86] J Aasi and et al., "Enhanced sensitivity of the LIGO gravitational wave detector by using squeezed states of light," *Nature Photonics*, vol. 7, no. 8, pp. 613–619, 2013.

[87] D. M. Stamper-Kurn and M. Ueda, "Spinor bose gases: Symmetries, magnetism, and quantum dynamics," *Rev. Mod. Phys.*, vol. 85, pp. 1191–1244, 3 Jul. 2013.

[88] E. M. Bookjans, A. Vinit, and C. Raman, "Quantum phase transition in an antiferromagnetic spinor bose-einstein condensate," *Phys. Rev. Lett.*, vol. 107, p. 195 306, 19 Nov. 2011.

[89] T.-L. Ho and S. K. Yip, "Fragmented and single condensate ground states of spin-1 bose gas," *Phys. Rev. Lett.*, vol. 84, pp. 4031–4034, 18 May 2000.

[90] M. Vengalattore, S. R. Leslie, J. Guzman, and D. M. Stamper-Kurn, "Spontaneously modulated spin textures in a dipolar spinor bose-einstein condensate," *Phys. Rev. Lett.*, vol. 100, p. 170 403, 17 May 2008.

[91] A. S. Sørensen and K. Mølmer, "Entanglement and extreme spin squeezing," *Phys. Rev. Lett.*, vol. 86, pp. 4431–4434, 20 May 2001.

[92] C. S. Gerving, T. M. Hoang, B. J. Land, M Anquez, C. D. Hamley, and M. S. Chapman, "Non-equilibrium dynamics of an unstable quantum pendulum explored in a spin-1 Bose-Einstein condensate," *Nature Communications*, vol. 3, p. 1169, Nov. 2012.

[93] E. J. Mueller, T.-L. Ho, M. Ueda, and G. Baym, "Fragmentation of bose-einstein condensates," *Phys. Rev. A*, vol. 74, p. 033 612, 3 Sep. 2006.

[94] B. Evrard, A. Qu, J. Dalibard, and F. Gerbier, "Observation of fragmentation of a spinor bose-einstein condensate," *Science*, vol. 373, no. 6561, pp. 1340–1343, 2021.

[95] C. A. R. Sá de Melo, "Squeezed boson states in condensed matter," *Phys. Rev. B*, vol. 44, pp. 11 911–11 917, 21 Dec. 1991.

[96] D. M. Broun, "What lies beneath the dome?" *Nature Physics*, vol. 4, pp. 170–172, 3 2008.

[97] P. Gegenwart, Q. Si, and F. Steglich, "Quantum criticality in heavy-fermion metals," *Nature Physics*, vol. 4, pp. 186–197, 3 2008.

[98] S. Sachdev, "Quantum magnetism and criticality," *Nature Physics*, vol. 4, pp. 173–185, 3 2008.

[99] M. Kitagawa and M. Ueda, "Squeezed spin states," *Phys. Rev. A*, vol. 47, pp. 5138–5143, 6 Jun. 1993.

[100] Y. C. Liu, Z. F. Xu, G. R. Jin, and L. You, "Spin squeezing: Transforming one-axis twisting into two-axis twisting," *Physical Review Letters*, vol. 107, no. 1, 2011.

[101] L.-N. Wu, M. K. Tey, and L. You, "Persistent atomic spin squeezing at the heisenberg limit," *Phys. Rev. A*, vol. 92, p. 063 610, 6 Dec. 2015.

[102] J. Hu, W. Chen, Z. Vendeiro, A. Urvoy, B. Braverman, and V. Vuletić, "Vacuum spin squeezing," *Phys. Rev. A*, vol. 96, p. 050 301, 5 Nov. 2017.

[103] G. Floquet, "Sur les équations différentielles linéaires à coefficients périodiques," *Annales scientifiques de l'École Normale Supérieure*, vol. 12, pp. 47–88, 1883.

[104] W. H. Zurek, U. Dorner, and P. Zoller, "Dynamics of a quantum phase transition," *Phys. Rev. Lett.*, vol. 95, p. 105 701, 10 Sep. 2005.

[105] R. Giannini, E. Breschi, C. Affolderbach, G. Bison, G. Mileti, H. P. Herzig, and A. Weis, "Sub-Doppler diode laser frequency stabilization with the DAVLL scheme on the D1 line of a 87Rb vapor-cell," in *14th International School on Quantum Electronics: Laser Physics and Applications*, P. A. Atanasov, T. N. Dreischuh, S. V. Gateva, and L. M. Kovachev, Eds., International Society for Optics and Photonics, vol. 6604, SPIE, 2007, pp. 156 –160.

[106] T Petelski, M Fattori, G Lamporesi, J Stuhler, and G. M. Tino, "Doppler-free spectroscopy using magnetically induced dichroism of atomic vapor: A new scheme for laser frequency locking," *The European Physical Journal D - Atomic, Molecular, Optical and Plasma Physics*, vol. 22, pp. 279–283, 2 2003.

[107] N. Derby and S. Olbert, "Cylindrical magnets and ideal solenoids," *American Journal of Physics*, vol. 78, no. 3, pp. 229–235, 2010.